

Application of low-pressure reverse osmosis in a two-stage biogas production: optimization of VFA concentration and biofouling monitoring

Zur Erlangung des akademischen Grades eines
DOKTORS DER INGENIEURWISSENSCHAFTEN (Dr.-Ing.)

von der KIT-Fakultät für Chemieingenieurwesen und Verfahrenstechnik des
Karlsruher Instituts für Technologie (KIT)

genehmigte
DISSERTATION

von

M.Sc. Giorgio Pratofiorito
aus Genua

Tag der mündlichen Prüfung: 22.06.2023

Erstgutachter: Prof. Dr. Harald Horn

Zweitgutachter: Prof. Dr. Ing. Mathias Ernst

Acknowledgement

The last three years have been a milestone for my personal and professional development. This growth would have not been possible without the people who supported me over the PhD.

First of all, I want to thank Prof. Harald Horn, who gave me the opportunity to work at his chair, hiring me for the position as doctoral student. His guidance was of great inspiration for me. It is easier to face difficulties when somebody stands behind you, especially when you know that this person believes in you. The motivation I received from him was accompanied by a sense of responsibility that I had to carry throughout the course of my work.

A special thank goes to Florencia Saravia, who was always there when I needed her the most. The discussions with her made me see problems from another perspective and helped me to find my way. Every talk we had was a chance for me to understand more about myself and to see things more clearly about my work. She gave me the courage to deal with mistakes head-on and transmitted me her passion for research.

Words can barely describe the value that people like Alfred, Axel, Dennis, Erwin and Joachim had for my daily work. It would have not been possible for me to produce any significant result without their technical support. All the same, I acknowledge the contribution of Matthias, Reinhard and Uli for the analytics behind the work. The concentrations found in this dissertation are the result of an analytical effort that must not be underestimated.

I am grateful to Annika Bauer, Max Hackbarth and Michael Wagner, who introduced me to OCT and image processing.

The friendly working atmosphere at the institute made it much easier to stand up in the morning. My fellow PhD students contributed enormously to this atmosphere. Therefore, thank you Amélie, Ali, Alondra, Andreas, Florian, Hessam, Jonas, Luisa, Max Miehle, Michael Sturm, Nikhil, Prantik, Rowayda, Stephan, Vasco and Yair. Of course, thank you Birgit Gordalla, Ewa Borowska, Gudrun Abbt-Braun, Norbert Andree, Rafael Peschke, Stephanie West, Sylvia Heck, Ulrike Scherer and Ursula Schäfer for the nice talks and exchanges.

If it were not for Andrea, I would have probably not even started the PhD. I cherish a fond memory of her supervision during my post graduate thesis. I like to consider her as the bridge between my master and my doctorate.

I hope I could at least partially return Andrea's supervision by carrying the responsibility for four other students. Thank you, Malek, Susan, David and Lars. Having the opportunity and the pleasure to work with you made me grow a lot. Hopefully, we both learned from each other.

Last but not least I am thankful to my parents, Cesarina and Gian Paolo, who supported me throughout my PhD.

Abstract

The two-stage fermentation of biomass to produce biomethane has gained attention in recent years. The key aspect of this process, that differentiates it from the conventional anaerobic digestion, is the spatial separation of the biological degradation steps of biomass. In a continuously stirred tank reactor (CSTR), complex macromolecules are converted in volatile fatty acids (VFA). The product of the CSTR is called hydrolysate and is be treated with microfiltration (MF) to avoid the clogging of a fixed bed reactor (FBR), where the hydrolysate is converted in biogas, and to increase the methane production rate. To decrease the volume flowrate of hydrolysate and increase the organic loading rate (OLR) to the FBR, reverse osmosis (RO) has been considered to concentrate VFA after the MF step.

A major research question in this work is how biofouling impacts the long-term operability of the RO unit and how it can be monitored to promptly react in case of membrane performance decline. The already high concentration of easily degradable carbon source in the hydrolysate implies a serious biofouling potential, that must be taken into consideration. The biofilm growing inside the feed channel of the spiral wound modules can heavily impair permeability and is therefore a challenge for the performance stability of the membrane. Monitoring tools for biofouling early-warning would help to control the process.

There are several imaging methods for biofilm monitoring and quantification. Among them, optical coherence tomography (OCT) distinguish itself for the combination of multiple features. These are: a fairly high resolution (down to 3 μm); a relatively easy to handle measuring apparatus; and the non-invasive nature of the measuring principle. OCT is therefore a useful tool for the study of biofouling in spacer-filled channels.

In the present dissertation, three main tasks are addressed: (I) the enhancement of the VFA reclamation by tuning the recovery of the membrane system; (II) the development of a method for biofilm monitoring in the feed channel of a flat sheet membrane module via OCT; and (III) the investigation of biofilm sensors as early-warning systems for permeability decline in RO-applications.

A lab-scale RO system with an internal recirculation was operated with several recoveries. Samples from the feed, the concentrate and the permeate were analyzed with respect to their dissolved organic carbon (DOC, representative of the VFA concentration) and to their ion concentrations. The impact of the recovery on the ratio between VFA concentration in the concentrate and in the permeate (R_c) was examined by means of mass balances under two operating pressures. The findings were supported by the calculation of the osmotic pressure of the solution in the feed channel. The results showed that the operating pressure influences the optimal recovery by changing the retention of the membrane. As the osmotic pressure increases in the feed channel, less VFA are retained and their reclamation worsens. This means that the recovery must not overcome a certain value, after which the concentration in the feed channel negatively affects the retention.

After having optimized the separation efficiency of the RO unit, the focus was shifted on the long-term operability of the system, particularly on biofouling issues. Flat-sheet membrane modules (FMM) were equipped with optical windows that allowed for the *in-situ* observation of the feed side of the membrane via OCT imaging. Pressure drop along the modules and permeability were constantly monitored. A macro for the differentiation of fouling on the membrane and on the spacer was written. Two parameters quantifying these two types of fouling were defined (*ME* for the membrane fouling and *SP* for the spacer fouling). Results shows that *SP* started increasing from the very beginning of the experiment and stabilized just when *ME* began to grow. This suggests that there is a preferential fouling of the spacer and that significant membrane fouling occurs only once the spacer is saturated with biofilm. Pressure drop was controlled by fouling on the spacer during the first stage of the experiment, while membrane fouling played a role only in the second half. Permeability decline correlated only with membrane fouling. However, surface coverage did not correlate with permeability decline, indicating that the biofilm first spread horizontally and then built up vertically, before a critical value of *ME* was reached. Only as the critical value was reached, the hydraulic resistance was high enough to strongly impact permeability.

Overall, OCT could help deepening the understanding of biofouling behavior in spiral wound modules and the developed parameters could successfully describe the phenomenon. However, OCT is difficult to apply in real scale plants due to the complexity of the measurement and the cost of the needed equipment. Therefore, the use of biofilm sensors in RO systems to predict membrane performance decline was explored as an alternative. A commercially available thermal based biofilm sensor was embedded in a flow cell, which was set parallel to two FMM. Both the flow cell and the FMM were equipped with optical windows, allowing for OCT imaging of the flow channels. The sensor signal correlated with the permeability decline and with the biofilm thickness on the sensor surface. Membrane and sensor cleaning was carried out and the sensor response was assessed. The sensor reacted to cleaning with a decrease of the signal, which was proportional to the amount of biofilm removed from the measuring surface and to the restoration of permeability.

Overall, the main challenges of the application of RO in the two-stage production of biogas were thoroughly addressed. The VFA yield was optimized by setting the right filtration recovery. The development of *ME* and *SP* parameters extended the current knowledge about biofilm formation in spiral wound modules. Moreover, a modified biofilm sensor showed promising results for the prediction of permeability decline. The tested sensor represents an interesting approach for biofilm monitoring in RO systems.

Zusammenfassung

Das Interesse an der zweistufigen Fermentation von Biomasse hat in den letzten Jahren kontinuierlich zugenommen. Schwerpunkt dieses Prozesses ist die räumliche Trennung der anaeroben Abbauschritte der Biomasse. In einem Rührkesselreaktor werden komplexe organische Makromoleküle zunächst hydrolysiert und in kurzkettige Fettsäuren (VFA) umgewandelt. Das hier gewonnene Hydrolysat wird mit Mikrofiltration (MF) behandelt, um eine Verstopfung des nachfolgenden Hochdruckfestbettreaktors zu vermeiden, in welchem die mikrobielle Umwandlung des Hydrolysats in Methan erfolgt. Als weiterer Vorbereitungsschritt kann eine Behandlung des Hydrolysats mit Umkehrosmose (reverse osmosis, RO) vorteilhaft sein. So können die im Rührkesselreaktor entstehenden VFA aufkonzentriert werden. Dabei sinkt die Verweilzeit im kostenintensiven Festbettreaktor und das benötigte Reaktorvolumen kann entsprechend kleiner gewählt werden.

Ein wichtiger Punkt für den Langzeitbetrieb von RO ist die Auswirkung von Biofouling auf die Permeabilität der Membran und die Frage, wie man mit möglichen Reinigungsschritten rechtzeitig auf Biofouling reagieren kann. Eine hohe Konzentration von VFA im Hydrolysat stellt dabei ein konkretes Biofoulingpotential dar. Der in der Folge im Feedkanal wachsende Biofilm kann die Membranpermeabilität und damit die Membranleistung stark herabsetzen. Überwachungssysteme zur Kontrolle von Biofouling könnten helfen, diesen Leistungsabfall durch eine gezielte Steuerung von Reinigungszyklen der Membranen zu minimieren.

Es gibt inzwischen diverse bildgebende Verfahren für die Quantifizierung von Biofilmen. Dabei bietet die optische Kohärenztomografie (OCT) für die Untersuchung von Biofouling in RO-Feedkanälen gegenüber anderen Methoden einige grundlegende Vorteile: eine relativ hohe Auflösung (bis zu 3 μm), eine leichte Handhabung und ein nicht invasives Messprinzip.

Die vorliegende Arbeit befasst sich mit (I) der Verbesserung der VFA Rückgewinnung durch die Einstellung der Ausbeute der Membrananlage; (II) der Entwicklung einer Methode zur Biofilmüberwachung im Feedkanal eines RO-Moduls mithilfe der OCT; und (III) der Anwendung von Biofilmsensoren als Frühwarnsystem für die Abnahme der Permeabilität in RO-Membranen.

Eine RO-Laboranlage mit einem internen Rezirkulationssystem wurde bei verschiedenen Ausbeuten betrieben. Proben aus dem Feed, dem Konzentrat und dem Permeat wurden in Hinblick auf ihren gelösten organischen Kohlenstoff (DOC) und ihre Konzentration an anorganischen Ionen analysiert. Der Einfluss der Ausbeute auf das Verhältnis zwischen der Konzentration von VFA im Konzentrat und der Konzentration im Permeat (R_c) wurde mittels Massebilanzierung untersucht. Eine Berechnung des osmotischen Drucks im Feedkanal konnte die Ergebnisse untermauern. Es wurde festgestellt, dass sich der beaufschlagte Druck durch die Änderung des Rückhalts der Membran auf die optimale Ausbeute auswirkt. Wenn der osmotische Druck im Feedkanal steigt, werden weniger VFA zurückgehalten. Das heißt,

dass für die Ausbeute ein Schwellenwert existiert, oberhalb dessen die Konzentration im Feedkanal einen negativen Einfluss auf den Rückhalt der Membran hat.

Nach der Optimierung der Trennungseffizienz wurde das Biofouling untersucht, welches als die größte Herausforderung des Langzeitbetriebs gilt. Flachmembranmodule (FMM) wurden mit optischen Fenstern ausgestattet, die die Bildgebung der Feedseite der Membran ermöglichten. Die Anlage wurde für 26 Tage betrieben und dabei täglich OCT Bilder aufgenommen. Der Druckabfall entlang des Moduls und die Permeabilität wurden dabei kontinuierlich erfasst. Die OCT Bilder wurden mit einem Makro ausgewertet, das die separate Quantifizierung von Biofouling auf dem Spacer und auf der Membran ermöglichte. Zwei Parameter wurden definiert, um diese zwei Arten von Fouling voneinander zu unterscheiden, ME für die Membran und SP für den Spacer. SP nahm zu, sobald das Experiment gestartet wurde, und erreichte ein Plateau, als ME anfang zu steigen. Das lässt rückschließen, dass die zwei Arten von Fouling nacheinander auftreten, und dass Biofilm erst auf der Membran anfängt zu wachsen, wenn der Spacer schon bedeckt ist. Der Druckabfall während der ersten Phase des Experiments konnte demnach auf den Einfluss des Foulings auf dem Spacer (SP) zurückgeführt werden, während das Fouling auf der Membran ME erst in der zweiten Phase dazu beitrug. Die Abnahme der Permeabilität korrelierte dabei nur mit der Dicke der Foulingschicht auf der Membran und nicht mit dem Bedeckungsgrad. Dies weist darauf hin, dass der Biofilm sich zuerst auf der Membranfläche ausbreitet und seine Dicke erst danach steigt. Sobald ein kritischer Wert von ME erreicht wurde, war der hydraulische Widerstand groß genug, um die Permeabilität zu beeinträchtigen.

Insgesamt ermöglichte die Anwendung von OCT die Vertiefung der Kenntnisse über Biofouling in Wickelmodulen und die entwickelten Parameter konnten das Phänomen erfolgreich beschreiben. Allerdings kann das OCT Messverfahren aufgrund der Notwendigkeit des optischen Zugriffs nicht direkt in industriellen Wickelmodulen angewendet werden. Aus diesem Grund wurde die Anwendung von Biofilmsensoren für die Vorhersage der Membranleistung in RO-Anlagen untersucht. Ein kommerziell verfügbarer thermischer Sensor wurde in eine Fließzelle integriert, die in eine RO-Anlage parallel zu zwei FMM eingebaut wurde. Sowohl die Fließzelle als auch die FMM wurden mit optischen Fenstern ausgestattet, die die Bildgebung der Fließkanäle mittels OCT ermöglichten. Daraufhin konnte das Sensorsignal mit der Permeabilitätsabnahme und mit der Biofilmdicke auf der Sensoroberfläche korreliert werden. Um den Einfluss der Reinigungszyklen auf diese Korrelation zu überprüfen, wurde eine Membran- und Sensorspülung durchgeführt. Hier konnte eine Abnahme des Sensorsignals während der Reinigung nachgewiesen werden. Die Verringerung der Biofilmdicke auf dem Sensor und die Wiederherstellung der Membranpermeabilität verhielten sich dabei proportional zu der Abnahme des Sensorsignals.

Die Hauptherausforderungen der Applikation von RO in der zweistufigen Druckfermentation von Biomasse wurden in dieser Dissertation ausführlich thematisiert. Die VFA-Rückgewinnung wurde optimiert. Mittels OCT wurde das Verständnis der Biofilmbildung in Wickelmodulen vertieft. Die Weiterentwicklung eines Biofilmsensors zeigte vielversprechende Ergebnisse für

die Vorhersage der Permeabilitätsabnahme der Membran. Damit stellt der Sensor einen interessanten Ansatz für die Biofilmüberwachung in RO-Anlagen dar.

Publications

The chapters 3 and 4 of this dissertation have been published in the first and second of the following peer-reviewed articles.

Giorgio Pratofiorito, Harald Horn, Florencia Saravia. Differentiating fouling on the membrane and on the spacer in low-pressure reverse-osmosis under high organic load using optical coherence tomography, *Separation Purification Technology* 291 (2022) 120885, <https://doi.org/10.1016/j.seppur.2022.120885>

Giorgio Pratofiorito, Harald Horn, Florencia Saravia. Impact of the recovery on concentrating acetic acid with low-pressure reverse-osmosis membranes, *Membranes* 11 (10) (2021) 742, <https://doi.org/10.3390/membranes11100742>

Giorgio Pratofiorito, Max Hackbarth, Carmen Mandel, Siyavuya Madlanga, Stephanie West, Harald Horn, Andrea Hille-Reichel. A membrane biofilm reactor for hydrogenotrophic methanation, *Bioresource Technology* 321 (2021) 124444, <https://doi.org/10.1016/j.biortech.2020.124444>

The following manuscript has been submitted to a peer-reviewed journal and is further listed in chapter 5 of this dissertation:

Giorgio Pratofiorito, Harald Horn, Florencia Saravia. Application of online biofilm sensors for the prediction of membrane performance in a reverse osmosis with high organic load feed streams. Submitted

Contents

| | |
|---|----|
| 1 Introduction | 1 |
| 1.1 Biomass to VFA | 1 |
| 1.2 High-pressure fermentation | 2 |
| 1.3 Application of reverse osmosis in the two-stage biogas production | 3 |
| 1.4 Reverse osmosis | 5 |
| 1.5 Types of fouling and ways to mitigate it | 11 |
| 1.6 Biofilm sensors | 14 |
| 1.7 Imaging techniques for the visualization of biofouling on membranes | 16 |
| 1.8 Outline of the work | 23 |
| 2 Preliminary work | 25 |
| 2.1 Choice of the membrane | 25 |
| 2.2 Formulation of a model solution and choice of the operating pressure | 30 |
| 3 Impact of the recovery on concentrating acetic acid with low-pressure reverse-osmosis membranes | 33 |
| 3.1 Introduction | 33 |
| 3.2 Materials and methods | 37 |
| 3.2.1 Experimental setup | 37 |
| 3.2.2 Feed solution | 38 |
| 3.2.3 Sampling and analytics | 38 |
| 3.2.4 Development of parameters | 39 |
| 3.3 Results and discussion | 40 |
| 3.3.1 Experiment at 22 bar | 40 |
| 3.3.2 Experiment at 25 bar | 43 |
| 3.3.3 Economic considerations | 45 |
| 3.4 Conclusions | 45 |
| 4 Differentiating fouling on the membrane and on the spacer in low-pressure reverse-osmosis under high organic load using optical coherence tomography | 47 |
| 4.1 Introduction | 47 |
| 4.2 Materials and methods | 50 |
| 4.2.1 Feed solution | 50 |
| 4.2.2 Lab-scale LPRO setup | 50 |
| 4.2.3 Operational conditions | 51 |
| 4.2.4 OCT and image processing | 51 |
| 4.2.4.1 Image analysis of the membrane | 52 |
| 4.2.4.2 Image analysis of the spacer region | 53 |
| 4.3.1 Biofilm development | 54 |

| | |
|---|-----------|
| 4.3.2 Flux decline and feed channel pressure drop increase | 57 |
| 4.3.3 Surface coverage distribution | 58 |
| 4.4 Conclusions | 59 |
| 5 Application of online biofilm sensors for the prediction of membrane performance in a reverse osmosis with high organic load feed streams..... | 60 |
| 5.1 Introduction | 60 |
| 5.2 Materials and methods | 62 |
| 5.2.1 Flat sheet membrane modules | 62 |
| 5.2.2 Biofilm sensor | 62 |
| 5.2.3 Experimental procedure..... | 63 |
| 5.2.4 OCT imaging | 65 |
| 5.3 Results and discussion | 65 |
| 5.3.1 Biofilm detection with the unmodified flow cell surface..... | 65 |
| 5.3.2 Biofilm detection with a sandblasted flow cell surface | 67 |
| 5.3.3 Cleaning of the membrane and the sensor | 72 |
| 5.4 Conclusions | 74 |
| 6 Summary | 75 |
| 7 Appendix | 77 |
| 8 Reference | 85 |

List of figures

| | |
|---|----------------|
| Fig. 1-1: Flow diagram of the two-stage fermentation process developed in the ProBioLNG project. The hydrolysate coming from the HR is treated with MF and RO before it is fed to the MR | Page 4 |
| Fig. 1-2 Representation of the osmotic pressure. Water flows from the diluted solution to the concentrated solution. | Page 5 |
| Fig. 1-3 Schematic of the transition between pressure retarded osmosis and reverse osmosis. π is the osmotic pressure of the feed solution..... | Page 6 |
| Fig. 1-4 Rendering of an unwrapped spiral wound module. The feed enters the module from one side while the permeate and the concentrate leave it at the opposite end. The feed spacer separates the membrane sheets from one another and the permeate spacer conveys the permeate towards the central perforated pipe. | Page 9 |
| Fig. 1-5 Schematic of the solution-diffusion model (adapted from Melin and Rautenbach 2003)..... | Page 10 |
| Fig. 1-6 Occurrence of biofouling in a crossflow membrane module. The biofilm represents a hindrance for water flux through the membrane..... | Page 13 |
| Fig. 1-7: Working principle of the DEPOSENS biofilm sensor. The sensor detects changes in the heat transmission and generates a signal, which is proportional to the thickness of the biofilm (taken from Netsch et al. 2021)..... | Page 16 |
| Fig. 1-8: Working principle of OCT. Interferences are generated as the reference beam and the sample beam are recombined..... | Page 19 |
| Fig. 1-9: The Fast Fourier Transform (FFT) converts the signal from the time domain to the frequency domain. The information extracted from this spectrum is then used to calculate the depth profile (A-scan). | Page 20 |
| Fig. 1-10: Combining several A-scans together yields a B-scan and stacking more B-scans yields a C-scan (adapted from Min et al. 2013)..... | Page 21 |
| Fig. 2-1 Permeability of different membranes at 25 °C and 12 bar (measured with demineralized water)..... | Page 26 |
| Fig. 2-2 Retention of the six membranes for compounds of different molecular weight | Page 27 |
| Fig. 2-3 DOC and TN retention of the three selected membranes, pH 5.0 and 8, 12 and 16 bar. | Page 29 |
| Fig. 2-4 DOC and TN retention of the three selected membranes, pH 6.0 and 8, 12 and 16 bar. | Page 29 |
| Fig. 2-5 Retention values of the XLE membrane for DOC, TN and the main VFA in the hydrolysate at 12 bar and 37 °C..... | Page 31 |
| Fig. 3-1: Schematic representation of the system. FP: Feed pump; CP: concentrate pump; RT: recirculation tank; P: pressure; T: temperature; F: flow; and L: level. | Page 38 |
| Fig. 3-2: Osmotic pressure and acetate concentrations in the concentrate and in the permeate at different concentration factors CF (22 bar). | Page 41 |
| Fig. 3-3: Concentration ratio (R_c) and mass ratio (R_w) at different concentration factors CF (22 bar)..... | Page 41 |
| Fig. 3-4: Retention of acetic acid and ammonium (measured as TN) at different CF (22 bar).... | Page 42 |
| Fig. 3-5: Retention of acetic acid and ammonium (measured as TN) at different concentration factors CF (25 bar). | Page 44 |
| Fig. 3-6: Osmotic pressure and acetate concentrations in the concentrate and in the permeate at different concentration factors CF (25 bar). | Page 44 |
| Fig. 3-7: Concentration ratio (R_c) and mass ratio (R_w) at different concentration factors CF (25 bar). | Page 45 |

| | |
|--|----------------|
| Fig. 4-1: Photograph of an FMM with optical windows (a) and schematic representation of the lab-scale LPRO setup (b). FT: feed tank; TI: temperature sensor; PI: pressure sensor; FI: flowmeter..... | Page 51 |
| Fig. 4-2: Image processing steps for the membrane. Top view of a spacer rhombus (a) lateral view of the fouling layer on the membrane (b). | Page 52 |
| Fig. 4-3: Processing steps of a B-scan. The raw image dataset (a) is first filtered and the contrast is enhanced (b) and then the dataset is binarized (c). | Page 53 |
| Fig. 4-4: Development of relative pressure drop together with spacer fouling (SP) (a), membrane fouling (ME) (b), and flux (c). The arrows show the phases in which pressure drop is governed by fouling on the spacer (I) and on the membrane (II). | Page 55 |
| Fig. 5-1 Sketch and dimensions of the flow cell in which the biofilm sensor was embedded, the optical windows for OCT measurement are located at 140 mm and 210 mm from the inlet above the biofilm sensor..... | Page 63 |
| Fig. 5-2 Experimental setup. PI: pressure indicator; TI: temperature indicator; FI: flow indicator. The flow cell with the biofilm sensor was set parallel to the membrane modules..... | Page 64 |
| Fig. 5-3 a) Permeability and biofilm sensor signal; b) biofilm thickness on the membrane and on the sensor for the experiment with the unmodified flow cell measured with OCT. The error bars represent the deviation between the average values of the two FMM..... | Page 67 |
| Fig. 5-4 a) Permeability and biofilm sensor signal; b) biofilm thickness on the membrane and on the sensor for the experiment with the sandblasted flow cell measured with OCT. Exp. 2a (left) and Exp. 2b (right)..... | Page 69 |
| Fig. 5-5 Estimated substrate concentration profiles near the membrane surface C_m (a) and near the sensor surface $\sim C_f$ (b). Due to the very thin biofilm thickness and the low amount of biomass the consumption is nearly neglectable..... | Page 71 |
| Fig. 5-6 a) Permeability and biofilm sensor signal; b) biofilm thickness on the membrane and on the sensor before and after cleaning measured by OCT (Exp. 3). Time span of cleaning: h 24 to h 30..... | Page 73 |

List of tables

| | |
|---|----------------|
| Tab. 1-1 Typical VFA produced. Adapted from Alvarado Munguía 2022..... | Page 2 |
| Tab. 2-1: Composition of the solution used to determine the MWCO of the six membranes.... | Page 27 |
| Tab. 2-2: MWCO of the six membranes..... | Page 28 |
| Tab. 2-3 Composition of the model solution used in the present work. Acetic acid and calcium acetate were used to reach the equivalent DOC value of the other main VFA..... | Page 32 |
| Tab. 3-1 Membranes used for VFA recovery..... | Page 35 |
| Tab. 6-1 Feed composition..... | Page 63 |

Nomenclature

Abbreviations

| Abbreviation | Meaning |
|--------------|------------------------------------|
| AFM | Atomic force microscope |
| CLSM | Confocal laser scanning microscopy |
| CSTR | Continuously stirred tank reactor |
| DOM | Dissolved organic matter |
| EPS | Extracellular polymeric substances |
| FBR | Fixed bed reactor |
| FFT | Fast Fourier transformed |
| FMM | Flat membrane module |
| HR | Hydrolysis reactor |
| LM | Light microscopy |
| LPRO | Low-pressure reverse-osmosis |
| MF | Microfiltration |
| MR | Methane reactor |
| MRI | Magnetic resonance imaging |
| NF | Nanofiltration |
| NMR | Nuclear magnetic resonance |
| NOM | Natural organic matter |
| OCT | Optical coherence tomography |
| OPO | Oxygen planar optode |
| PSA | Pressure swing adsorption |
| RO | Reverse osmosis |
| SEM | Scanning electron microscopy |
| SMP | Soluble microbial products |
| SOC | Synthetic organic compounds |

| | |
|-------|---|
| UF | Ultrafiltration |
| UV | Ultraviolet |
| VFA | Volatile fatty acids |
| μ | Chemical potential [J mol ⁻¹] |

Parameters

| Symbol | Meaning | Units |
|--------|--------------------------|------------------------|
| C | Concentration | [mol L ⁻¹] |
| CF | Concentration factor | [-] |
| COD | Chemical oxygen demand | [mg L ⁻¹] |
| DOC | Dissolved organic carbon | [mg L ⁻¹] |
| MWCO | Molecular weight cut-off | [g mol ⁻¹] |
| T | Temperature | [K] |
| TMP | Transmembrane pressure | [bar] |
| TN | Total nitrogen | [mg L ⁻¹] |
| μ | Chemical potential | [J mol ⁻¹] |

1 Introduction

1.1 Biomass to VFA

Climate change is deteriorating the environment quality and represents a key aspect of the policy choices of many countries in Europe. To decrease our dependency from fossil fuels, several options have been considered and are under investigation. One of them is the exploitation of biomass as a source of energy on one hand and of platform chemicals on the other hand. The chemical energy stored in the organic bonds of biomass can be converted to other forms of energy (i.e. heat or electricity) without releasing fossil CO₂ in the atmosphere. However, the organic compounds, of which biomass is constituted, can be also used to provide carbon neutral alternatives in the market of chemical intermediates. To accomplish these two tasks, the concept of biorefinery has gained importance. A biorefinery converts biomass into either biofuels or valuable products that are later used as building blocks for several processes (e.g. in the chemical, pharmaceutical, textile, cosmetic and food industries). In 2012 the German Government has published a *“Roadmap for biorefineries”* (Roadmap Bioraffinerien 2012) to provide practical suggestions on how to develop biorefineries. In current years, much effort is being dedicated to the development of the suitable technologies that will allow to shift the market of platform chemicals into a more sustainable one in the near future. Some of the most relevant biologically derived platform chemicals are: sugars, alcohols, carboxylic acids, phenols, aldehydes and molasse (Fang et al. 2017). Among them, volatile fatty acids (VFA) can be produced by microbial fermentation and represent interesting intermediates for the production of valuable chemicals. However, given the limited amount of available biomass, there is a competition between biofuels and biologically based platform chemicals. For instance, in both pathways the production of VFA via anaerobic digestion is of great importance. In fact, VFA can both represent valuable intermediates in the chemical production chain and at the same time they can be directly used as substrate for biogas production.

VFA are produced as intermediates during the anaerobic digestion of biomass. Firstly, complex organic molecules (long chain hydrocarbons, proteins, nucleic acids and triglycerides) are degraded into shorter compounds (sugars, aminoacids, nucleotides and carboxylic acids). This process is called hydrolysis and is performed by microbial enzymes under anaerobic conditions. The lighter compounds subsequently undergo a further degradation into VFA via acidification. The main VFA produced during acidification are listed in Tab. 1-1. The optimal pH for hydrolysis and acidification is reported to be between 5.0 and 6.5 (Alvarado Munguía 2022).

Tab. 1-1: Typical VFA produced. Adapted from Alvarado Munguía 2022.

| VFA | Chemical formula |
|-----------------|--|
| Formic acid | HCOOH |
| Acetic acid | CH ₃ COOH |
| Propionic acid | CH ₃ CH ₂ COOH |
| Butyric acid | CH ₃ (CH ₂) ₂ COOH |
| Valeric acid | CH ₃ (CH ₂) ₃ COOH |
| Isovaleric acid | (CH ₃) ₂ CHCH ₂ COOH |
| Caproic acid | CH ₃ (CH ₂) ₄ COOH |

The production of VFA is highly dependent on the operating conditions (pH, temperature, retention time, mixed microbial culture and substrate). A pH lower than 6.0 or higher than 8.0 can inhibit the growth of VFA consuming microorganisms, resulting in a higher production of VFA (Atasoy et al. 2018). Zhao et al. (2018) found that a stepwise increase of the pH from 9.0 to 11.0 enhances the activity of VFA producing bacteria. Temperature is another important factor playing a role in the regulation of VFA production. Under thermophilic conditions (55 °C) the hydrolysis rate increased compared to mesophilic conditions (35 °C), leading to a 10 times higher production of VFA (Hao and Wang 2015; Zhang et al. 2009). Retention time does not only influence the overall VFA production, but also their composition, due to changes in the microbial community. In general, the higher the retention time, the higher the VFA production (Bolaji and Dionisi 2017). However, the optimal retention time strongly depends on the substrate used (Atasoy et al. 2018). The use of different feedstocks results in different degrees of acidification, defined as the ratio between the COD converted in carboxylic acid over the initial COD. The amount of readily fermentable organic matter has a direct impact on the degree of acidification. Lignocellulosic substrates, soapy slurry and landfill leachates have the lowest acidogenic potential with a degree of acidification below 10%. This is due to the high percentage slowly degradable organic matter in the feed. In contrast, the degree of acidification of chees whey, molasses and the organic fraction of municipal solid waste reaches 40% (Atasoy et al. 2018). Primary sludge is also rich in fast degradable organic matter and is therefore a good substrate for VFA production (Ucisik and Henze 2008).

1.2 High-pressure fermentation

During the two further stages of anaerobic digestion – acetogenesis and methanogenesis – VFA are first degraded into acetic acid and hydrogen and then into biogas, mainly composed by methane and carbon dioxide (Fig. 1-1). The microorganisms responsible for these transformations have different optimal growth conditions (temperature and pH) than the bacteria involved in hydrolysis and acidification. The optimum pH for methanogenesis is reported to be near 7.0 (Alvarado Munguía 2022). Two-stages anaerobic digestion processes

have been developed, to displace the degradation steps of hydrolysis/acidification and acetogenesis/methanogenesis in two reactors (Muha et al. 2013; Lindner et al. 2015). The spatial separation of the degradation steps ensures the optimal environmental conditions for both groups of microorganisms. More recently, high-pressure fermentation of VFA has been proposed (Merkle et al. 2017a, 2017b; Lemmer et al. 2015; Bär et al. 2018). The overpressure in the methane reactor (MR) is autogeneratively provided by microorganisms their selves. In this way, the costs for the pressure boosting before the injection in the grid can be reduced by 45-60% (Bär et al. 2018). It has been proved, that the methanogenic activity is not inhibited by high pressures (up to 100 bar) (Merkle et al. 2017b).

A conventionally produced biogas is made up of approximately 60% methane and 40% carbon dioxide. Posttreatments are often applied to remove impurities (H_2O , H_2S , etc.) and to increase the percentage of methane, thereby enhancing the calorific value of the biogas. Pressure swing adsorption (PSA) is commonly used to remove CO_2 from the produced biogas. In PSA the gas flows through a porous material (zeolite or activated carbon) that selectively adsorbs CO_2 . Separation is performed based on molecular size exclusion (Niesner et al. 2013). Posttreatments for biogas purification imply additional costs and their need might be reduced by a higher methane content in the produced gas. The higher solubility of CO_2 in water compared to the one of CH_4 presents a further benefit of high-pressure fermentation. At higher pressures more CO_2 dissolves in the liquid phase than CH_4 . Increasing the operating pressure to 90 bar shifts the gas-liquid equilibrium to a point where the methane content in the gas phase reaches 90% (Lindeboom et al. 2011). The discharge of CO_2 with the liquid stream circumvents the need for PSA or at least reduces the cost for the posttreatment equipment. However, biogas upgrading can still be performed, converting the remaining CO_2 by hydrogenotrophic methanation. That is, hydrogen from renewable sources can be used as electron donor to reduce CO_2 to CH_4 (Pratofiorito et al. 2020).

Microfiltration (MF) was used to treat the effluent of the hydrolysis reactor (HR) (Bär et al. 2018). The aim was to remove the suspended solids contained in the hydrolysate, thereby avoiding the clogging of the MR, which was a fixed bed reactor (FBR). Another important role of MF in the process was to set a barrier, dividing the microbial communities of the two reactors, so that their operating conditions (pH, temperature and hydraulic retention time) can be optimized separately (Tuczinsky 2018). MF showed a reduction of the chemical oxygen demand (COD) of 50%, meaning that only half of the COD was composed of dissolved organic matter. The elimination of the inert organic matter allowed for the reduction of the hydraulic residence time from 4 days to 1.5 days. It follows that the application of MF in the high-pressure fermentation process can reduce the volume of the MR, which is the greatest cost driving apparatus of the process chain (Bär et al. 2018).

1.3 Application of reverse osmosis in the two-stage biogas production

A possible way to further decrease the MR volume is the enrichment of VFA in the hydrolysate after it has been treated with MF. Under the same organic loading rate of the MR, an increase

of the VFA concentration implies a reduction of the volumetric flowrate. At a given hydraulic retention time, this turns into a smaller MR volume. The reduction of the volumetric flowrate fed to the pressurized reactor also limits the energetic efforts related to pumping. Several technologies can be applied to concentrate these low molecular weight organic compounds, ranging from gas stripping, to solvent extraction, to the use of membranes (Atasoy et al. 2018). Reverse osmosis (RO) belongs to the latter option, shows good results in terms of retention and can separate VFA from sugars (Zhou et al. 2013a, 2013b), which are often present in fermentation broths as unreacted substrates.

The ProBioLNG project (founded by the German federal ministry of education and research, BMBF) involves partners from the industry as well as from the academia and aims to develop a sustainable and efficient process chain for the production and distribution of liquefied biomethane (BioLNG). The two-stage biogas production is at the heart of the process, involving two separate bioreactors (Fig. 1-1). The substrate, consisting of a mixture of pig manure and sugar beet juice, is fed after a pretreatment to the HR, where hydrolysis and acidogenesis take place. The HR is operated at a pH between 5.0 and 6.0. During this first stage of biomass degradation, complex organic compounds are converted to simple sugars, alcohols and VFA. The product of the HR is referred to as “hydrolysate” and is fed to the MR. In the MR, acetogenesis and methanogenesis convert the VFA into methane, which is later purified, liquefied and distributed. A MF (0.2 μm pore size) step separates the suspended solids from the hydrolysate and recirculates them to the HR, to increase their residence time in the reactor, thereby enhancing their degradation. An external circulation pump provides for homogeneous distribution of VFA concentration and for uniform temperature in the FBR.

To maximize the concentration of VFA that are fed to the MR, the use of RO after the MF step has been investigated (dashed line in Fig. 1-1). The idea is to feed the concentrate of the RO unit to the MR and dispose the permeate. A recirculation of the permeate to the HR would be counterproductive, since it would increase the inlet volumetric flowrate, thereby reducing the hydraulic retention time. Therefore, the RO separation efficiency must be as high as possible, in order to minimize the loss of VFA in the permeate.

The characterization of the hydrolysate is presented in the appendix 1-1. The concentration of VFA is already high, reaching up to 10 g L⁻¹ of dissolved organic carbon (DOC). This high concentration of easily degradable organic compounds implies a severe biofouling potential. Biofouling consists in the formation of a biofilm inside the membrane module that induces membrane performance decline. The threaten of biofouling is even more concrete, when the concentration of easily degradable organic compounds in the feed is considerably high. For this reason, it is crucial to mitigate biofouling and to control it in order to prolong the membrane lifetime and limit the downtimes needed for cleaning. The main challenge is to understand what mechanisms affect biofouling under these conditions and to find a way to reliably control fouling. Much effort has been additionally invested to develop online monitoring tools for biofouling quantification.

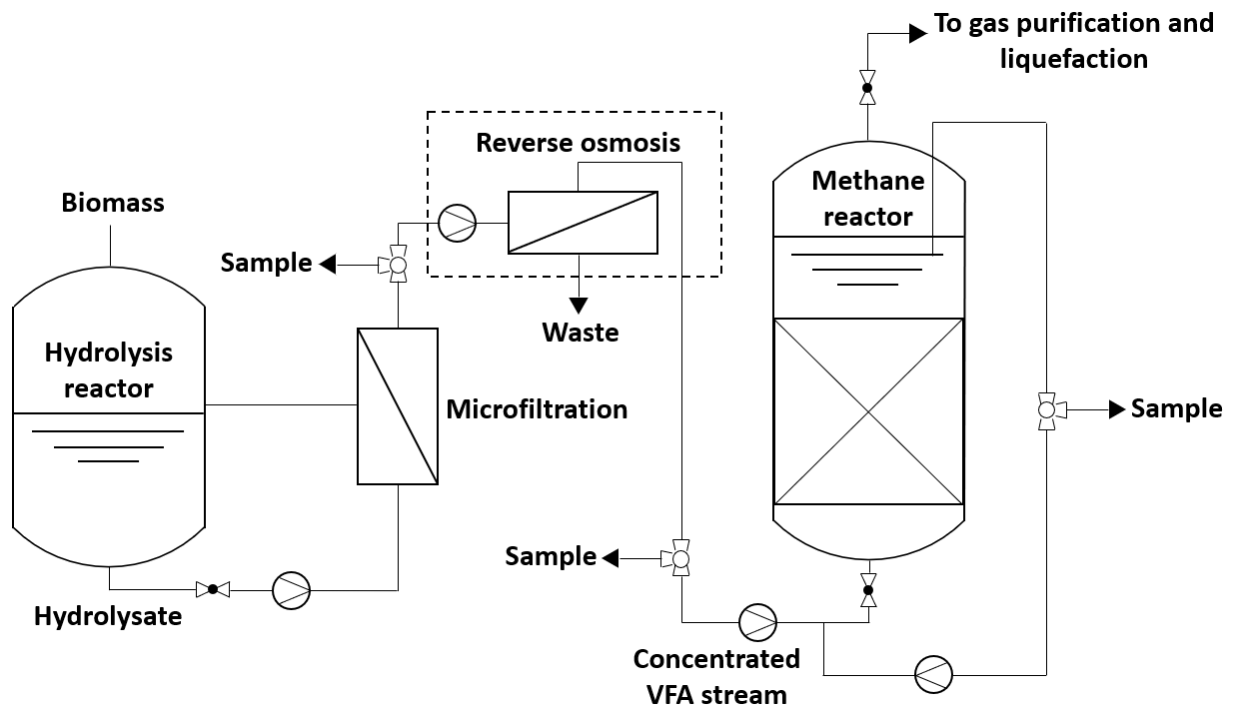


Fig. 1-1: Flow diagram of the two-stage fermentation process developed in the ProBioLNG project. The hydrolysate coming from the HR is treated with MF and RO before it is fed to the MR.

1.4 Reverse osmosis

RO has been applied for 50 years for sea water and brackish water desalination to supply arid and semiarid regions with fresh water. Currently, RO is the most used technology for water desalination with a share of 70% of the world total installed capacity, with the other technologies being mostly thermally driven (Curto et al. 2021). In 2015 desalination plants were 18,000 worldwide and this number is expected to double by 2030, together with the related energy demand (Voutchkov 2016). This stresses the need for ever more efficient RO systems to minimize energy consumption. This necessity is highlighted by another big issue related to climate change threatening global social stability: water scarcity. World population growth, economical development and changes in the styles of consumption are leading to an increase of fresh water usage. Globally, food production contributes to 69% of the fresh water consumption. This share comprehends farming, livestock breeding and aquaculture (United Nations 2022). According to the United Nations (UN) reports on water scarcity, in 2019 more than 700 million people were living in regions under high or critical water stress (United Nations 2015). This number is expected to raise up to 1.8 million by 2025. To tackle this and other related problems, the UN dedicated the sixth goal of *The 2030 agenda for sustainable development* to “Clean water and sanitation”. The target 6.4 requires an increase in the water use efficiency across all sectors and a substantial reduction of the number of people suffering

from water scarcity. As indicator for the achievement of this target, the UN promote the sustainable freshwater withdrawal. That means: the withdrawal of freshwater must be proportional to the renewable resources. In this context, water desalination (also via RO), appears to be an effective tool to handle the problem of freshwater scarcity on the planet, relieving groundwater and surface water reservoirs from an ever-increasing demand.

Osmosis is a natural phenomenon occurring in living beings. It consists in the passage of water through a semipermeable membrane from a diluted solution to a more concentrated solution. Water keeps flowing until an equilibrium across the two sides of the membrane is reached. Considering two compartments – one containing a concentrated solution and one containing pure water – separated by a membrane permeable to water, the pressure difference between the two compartments reached at the equilibrium is referred to as “osmotic pressure” of the concentrated solution (Fig. 1-2).

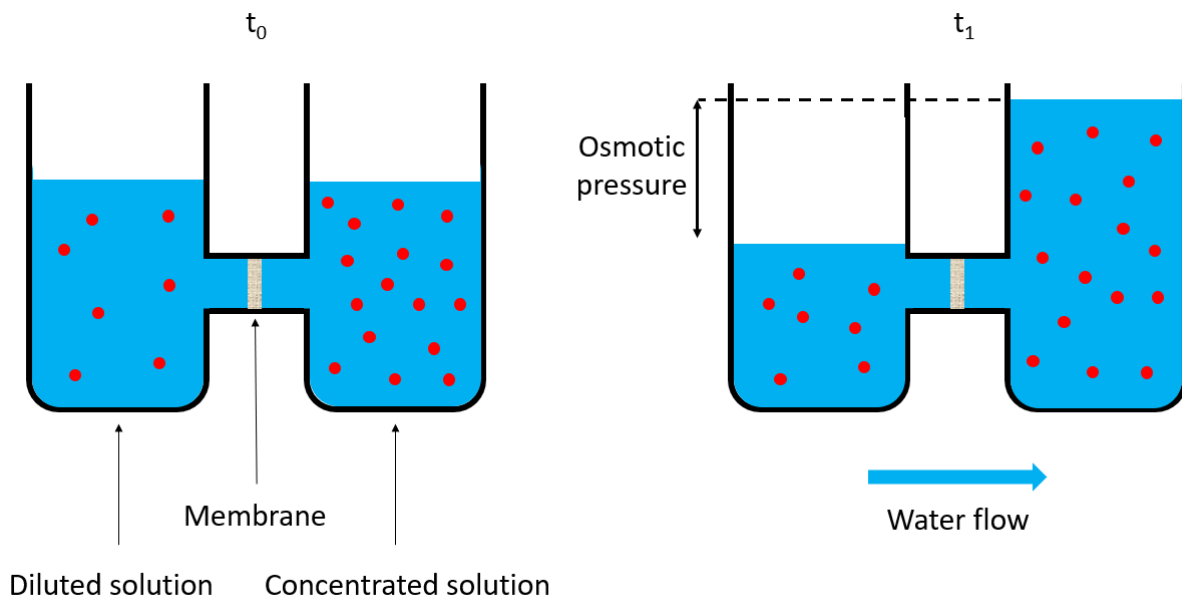


Fig. 1-2 Representation of the osmotic pressure. Water flows from the diluted solution to the concentrated solution.

RO is the process in which a suitable membrane is put in contact with a solution and a pressure higher than the osmotic pressure of the solution is applied, letting the water flow from the high concentrated solution to the low concentrated solution. The membranes used for RO are “composite membranes”, consisting of a supporting porous layer (often polyethersulfone) and a thin (thickness of few hundreds of nanometers) active layer. The supporting layer is very permeable and confers to the membrane its mechanical properties. The active layer is responsible for the retention properties of the membrane and is usually constituted by polyamides. Mass transport across the dense active layer occurs mainly via diffusion (Mulder 2003).

The better retention performances of tighter membranes come with the disadvantage of fluxes that are generally lower. On the other hand, looser membranes are able to allow for more water to pass per unit time and surface area, but they show poorer retention. Whatever passes the membrane goes under the name of “permeate”; whatever gets retained is called “concentrate” or “retentate”.

When it comes to water treatment, the product of the filtration is the permeate. As for sea water desalination, the concentrated solution (brine) is directly discharged into the sea. However, when RO is applied to solutions containing desirable compounds, the concentrate is the product. Ideally, only water passes through the membrane and all dissolved components are retained.

The osmotic pressure of the feed solution is an important factor for the planning of RO systems. If the applied pressure is smaller than the osmotic pressure, water will flow from the diluted side to the concentrated side, producing a pressure gradient. One can in this way obtain energy from the system. This mode of operation is called “pressure retarded osmosis” and is used to obtain energy from the mixing solutions with different salinities at the estuaries of rivers (Mulder 2003). Fig. 1-3 depicts the transition between pressure retarded osmosis and reverse osmosis.

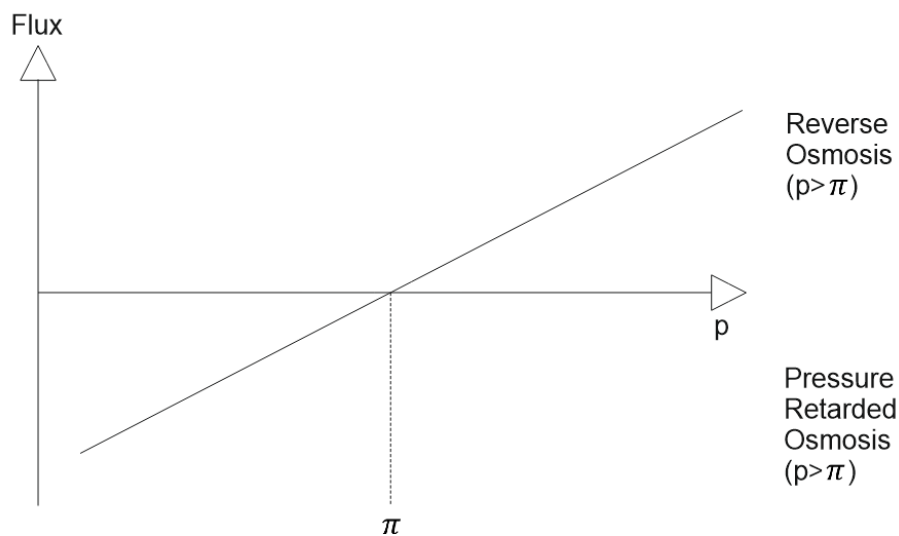


Fig. 1-3 Schematic of the transition between pressure retarded osmosis and reverse osmosis. π is the osmotic pressure of the feed solution.

The osmotic pressure can be calculated with the Van't Hoff's equation once the composition of the solution is known (Eq. 1-1).

$$\pi = RT \sum_{k=1}^n i_k C_k \quad \text{Eq. 1-1}$$

Where π is the osmotic pressure [bar], C_k is the concentration of the k^{th} component [mol L^{-1}], i_k is the Van't Hoff coefficient of the k^{th} component [-], R is the universal gas constant [$\text{L bar mol}^{-1} \text{K}^{-1}$] and T is the absolute temperature of the system [K]. The higher the osmotic pressure, the more energy will be needed to obtain a reasonable flux of permeate, making the operation of the system more expensive. Eq. 1-1 allows for the calculation of the minimum theoretical operating pressure that has to be applied, in order to allow for water permeation.

The smallest unit in which a membrane is packed is called “module”. Modules are designed in a way that minimizes the volume required to produce a certain amount of permeate flux. The goal is to have the highest active membrane surface per unit volume. The standard choice for the modules used for RO is the spiral-wound module, but hollow fiber modules have also been used (Baker 2004). They are assembled by laying the feed spacer (a grid usually made of a plastic material) between two flat sheet membranes in a sandwich-like fashion. On the outer sides of the sandwich two permeate spacers are placed. Then the envelope is wrapped around a perforated pipe to form a spiral. The spiral is enveloped in a housing. The feed enters the housing from one end and leaves it from the other end as concentrate. The permeate is collected by the permeate spacer, conveyed to the central tube and leaves the module at the distal end. This configuration offers high surface to volume ratios ($300 - 1,000 \text{ m}^2 \text{ m}^{-3}$). A rendering of unwrapped spiral wound can be seen in Fig. 1-4. To minimize the pressure drop encountered by the permeate flowing toward the central perforated tube, multi-envelope modules have been designed. In these modules several envelopes are wrapped together. For the same membrane area, the dimension of each envelope decreases. In this way the path taken by the permeate becomes shorter and the pressure drop is minimized (Baker 2004). The role of the feed spacer is to separate one sheet of membrane from the other, but also to promote mass transfer for a better mixing of the feed solution. Depending on the viscosity of the feed, the spacer can vary in thickness.

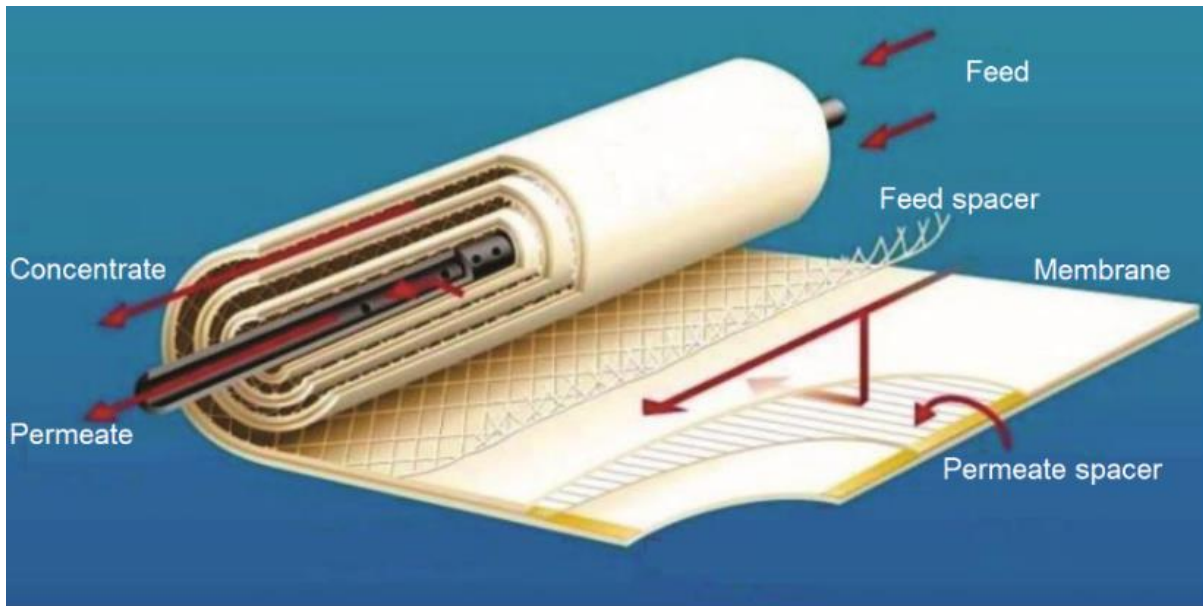


Fig. 1-4 Rendering of an unwrapped spiral wound module (adapted from Kim et al. 2013).

If the feed is particularly clean, hollow fiber modules can be used for RO and nanofiltration (NF) too. Hollow fiber modules offer the highest packing density, up to $30,000 \text{ m}^2 \text{ m}^{-3}$ (Mulder 2003). They are conceptually similar to capillary modules, with the main difference being the diameters of the membranes, that for hollow fibers is below 0.5 mm. The modules can be operated outside-in (the solution flows from the shell of the module to the lumens of the hollow fibers) or inside-out (the solution flows from the lumens of the hollow fibers to the shell of the module). One drawback of the outside-in configuration is channeling, i.e. the preferential flow of the feed in some specific regions of the module that prevents the efficient use of all membrane surface. On the other hand, for the inside-out configuration the pressure drop inside the hollow fibers can be quite high. In general, hollow fiber modules need clean feedwater, since they are particularly sensitive to fouling.

In general, there is a certain degree of freedom in the choice of how much water enters the permeate and how much is retained in the concentrate. The proportion between the permeate flowrate and the feed flowrate expressed in percentage is called “recovery”. As the recovery increases, the solution on the feed side of the membrane gets more concentrated and its osmotic pressure increases, causing the energy demand to increase in turn. It is therefore necessary to find a tradeoff for which the recovery is not too low (sufficient quantity of permeate) and not too high (contained expenses). Typical values for water desalination range between 35% and 50% (Curto et al. 2021). More detailed considerations about the impact of the recovery on the separation efficiency will be object of chapter 3. An equivalent way to express the recovery of an RO system is the concentration factor (CF), defined as the ratio between the volume fed to the system (Q_f) and the volume of produced concentrate (Q_c) per unit time (Eq. 1-2). The relation between the recovery and the CF is described by Eq.

1-3. The choice of considering the CF instead of the recovery is due to practical reasons. For instance, in the cases in which the concentrate is the product, it is more convenient to consider the CF. This provides a more immediate awareness of the amount of feed needed to produce a certain volume of concentrate. For this reason, the study described in chapter 3 considers the CF instead of the recovery, thereby presenting the results in an intuitive way.

$$CF = \frac{Q_f}{Q_c} \quad \text{Eq. 1-2}$$

$$\text{Recovery (\%)} = \left(1 - \frac{1}{CF}\right) \cdot 100 \quad \text{Eq. 1-3}$$

There are two models describing permeation in RO processes: the solution-diffusion model and the pore-flow model. Currently, the solution-diffusion model (Fig. 1-5) is generally accepted as the most suitable approach to rationalize reverse osmosis (Wijmans and Baker 1995). Based on this model, mass transport of water across the membrane is described as follows (Eq. 1-4) (Mulder 2003).

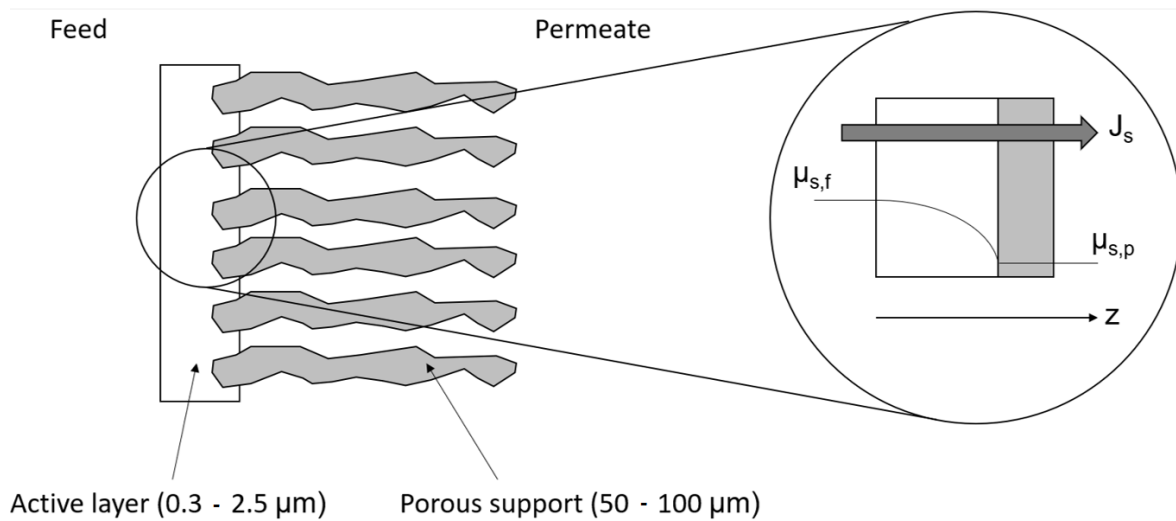


Fig. 1-5 Schematic of the solution-diffusion model (adapted from Melin and Rautenbach 2003).

$$J_w = A \left(\frac{\partial p}{\partial z} - \sigma \frac{\partial \pi}{\partial z} \right) \quad \text{Eq. 1-4}$$

Where J_w is the water flux [$\text{kg m}^{-2}\text{h}^{-1}$], A is the water permeability coefficient [$\text{kg m}^{-1}\text{h}^{-1}\text{bar}^{-1}$], $\frac{\partial p}{\partial z}$ is the pressure gradient across the membrane [bar m^{-1}], $\frac{\partial \pi}{\partial z}$ is the osmotic pressure gradient

across the membrane [bar m^{-1}] and σ is the reflection coefficient. σ is a correcting factor taking into account the permeation of small solutes, that reduces the osmotic pressure difference across the membrane.

In contrast, mass transport of the solute depends on its concentration on the feed side of the membrane (Eq. 1-5) (Mulder 2003).

$$J_s = -C_s \cdot m_s \cdot \frac{\partial \mu_s}{\partial z} \quad \text{Eq. 1-5}$$

Where J_s is the solute flux [$\text{kg m}^{-2} \text{s}^{-1}$], C_s is the solute concentration [kg m^{-3}], m_s is the mobility of the solute in the polymer phase [$\text{mol m}^2 \text{J}^{-1} \text{s}^{-1}$] and $\frac{\partial \mu_s}{\partial z}$ is the chemical potential gradient within the polymer phase [$\text{J mol}^{-1} \text{m}^{-1}$], the driving force for the mass transport across the membrane. In this context, the chemical potential represents the dependency of the energy of the system from the variation of the solute concentration. The higher the chemical potential, the stronger will be this dependency, and the energy of the system will vary faster by adding a given amount of solute to the system. The mobility of the solute can be related with the diffusion coefficient D_s [$\text{m}^2 \text{s}^{-1}$] by the Nerst- Einstein equation (Eq. 1-6).

$$D_s = R \cdot T \cdot m_s \quad \text{Eq. 1-6}$$

Combining Eq. 1-5 e Eq. 1-6 yields Eq. 1-7:

$$J_s = -C_s \cdot \frac{D_s}{RT} \cdot \frac{\partial \mu_s}{\partial z} \quad \text{Eq. 1-7}$$

According to Eq. 1-7, the bigger the chemical potential difference of a component across the membrane, the higher the driving force for its transport through the polymer phase. In contrast, Eq. 1-4 shows that water flux is proportional to the pressure difference across the membrane. If the solute concentration in the feed increases, more solute permeates through the membrane and the separation performance worsens. To mitigate this effect, it is recommendable to increase the operating pressure, thereby favoring the water transport across the membrane, as indicated by Eq. 1-4. High recoveries generally imply high solute concentration on the feed side of the membrane and are generally associated with high operating pressures.

1.5 Types of fouling and ways to mitigate it

A big concern regarding the operability of membrane systems is fouling, which consists in the deposition, adsorption or the adhesion to the membrane of (rejected) feed components. The occurrence of fouling reduces membrane permeability, resulting in either an increase of the transmembrane pressure (TMP) under constant flux operation, or to a flux decrease under

constant inlet pressure operation. Fouling causes therefore a deterioration of membrane performance, by increasing the energy required for the process.

There are four types of fouling, depending on the complex interaction between the membrane and the rejected components: particle fouling, scaling, organic fouling and biofouling.

Particle fouling is the deposition of solids on the membrane and involves two mechanisms: pore blocking (for porous membranes) and cake formation. In literature several classifications of particulate matter according to their size can be found. In general, there is good agreement about the following classification: settleable solids ($> 100 \mu\text{m}$), supra-colloidal solids ($1 \mu\text{m}$ to $100 \mu\text{m}$), colloidal solids (1 nm to $1 \mu\text{m}$) and dissolved solids ($< 1 \text{ nm}$) (Yiantsios et al. 2005). Particles can be either of organic or inorganic origin. The presence of aluminum silicate clays in the feed can lead to inorganic particulate fouling. These are particles that can be found in natural waters, especially sea water. On the other hand, organic colloids are often constituted by proteins, lipids, oil and grease (Yiantsios et al. 2005).

When the ionic product of a salt contained in the feed solution exceeds the solubility product, the solution becomes supersaturated and precipitation of salts might occur on the membrane surface. This phenomenon takes the name of scaling and involves three stages: supersaturation, nucleation and crystal growth. Commonly, high concentrations of calcium carbonate, calcium sulphate, strontium sulphate, barium sulphate, calcium phosphate and silicon dioxide in the feed water imply a high scaling potential.

Dissolved organic matter (DOM) is ubiquitous in natural waters and its definition comprises a broad variety of organic compounds, which can be both hydrophobic or hydrophilic (Abbt-Braun et al. 2003). DOM is classified according to its origin: natural organic matter (NOM) is present in surface water (rivers, lakes and reservoirs); synthetic organic compounds (SOC) derive from the introduction of anthropogenic substances such as detergents and surfactants; soluble microbial products (SMP) generate during biological purification steps and are present in water treatment plants effluents (Guo et al. 2012). The organic matter fraction with molecular size smaller than the membrane pores can adsorb and restrict the pore lumen, whereas larger fractions clog the pore at the entrance or deposit on the membrane surface, forming a gel layer (Fane 2016). Another factor playing a role is the hydrophobic/hydrophilic character of the DOM. It was reported that chemical affinity between the membrane and the DOM present in the feed tends to provoke severe fouling (Fane 2016).

Biofouling takes place when microorganisms proliferate on the membrane surface, feeding on the nutrients supplied with the feed water (Fig. 1-6). To facilitate their own attachment and ensure themselves a favorable environment for growth, microorganism produce a matrix of extracellular polymeric substances (EPS), which, together with the cells forms a "biofilm" (Desmond et al. 2022). Biofouling has been described as a biotic form of organic fouling (Flemming et al. 2002). In fact, these two fouling phenomena are difficult to differentiate and are often synergistic, with the deposit of organic macromolecules forming a conditioning film

facilitating biofouling initiation. Depending on the feed water quality, the combined effect of organic fouling and biofouling can contribute to the membrane performance deterioration. Biofilms can be very persistent and are often difficult to remove from surfaces. Their removal must tackle two aspects: the dissolution of the EPS matrix on one side and disinfection on the other side to retard regrowth right after cleaning. As for the dissolution of EPS, caustic agents showed to be more effective than acids (Jiang et al. 2017). A common solution is to combine NaOH (from 0.1% to 2% w/v) with NaClO (from 50 ppm to 200 ppm) (Saha et al. 2009).

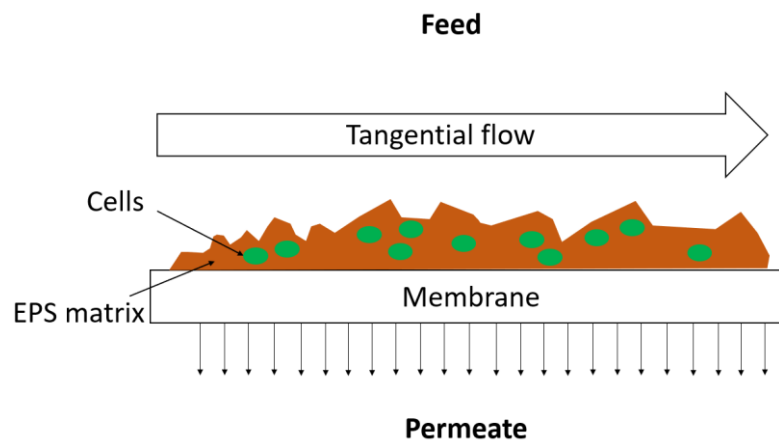


Fig. 1-6: Occurrence of biofouling in a crossflow membrane module. The biofilm represents a hindrance for water flux through the membrane.

To mitigate fouling in RO, several pretreatments are commonly used. To mitigate particle fouling, sedimentation, air floatation and granular media filtration (with or without coagulation/flocculation) are commonly used as pretreatment before the membrane unit (Abushaban et al. 2021). Alternatively, MF and UF are used to remove suspended solids from the feed. While MF and UF are gaining attention in recent years for RO pretreatment, coagulation/flocculation combined with a solid-liquid separation step is a well-established water treatment step to remove suspended colloids from a solution (Jiang et al. 2017). Scaling is usually mitigated with antiscalants (Matin et al. 2019). Antiscalants are complexing agents that retard the bulk crystallization of the salts (Benecke et al. 2018). Another option is to pretreat the solution with ion exchange resins, that act as water softeners, capturing divalent ions and releasing monovalent ions, which have higher solubility products. Biofouling needs to be tackled by disinfection, in order to minimize the microbial charge. Free chlorine, chloramines, chlorine dioxide, ozone and ultraviolet (UV) irradiation are often used as disinfecting agents. Free chlorine disinfection is very effective, since the reaction of chlorine with water produces hypochlorous acid, a strong oxidizing agent able to inactivate most pathogens (Al-Juboori and Yusaf 2012). Traces of chlorine must be accurately removed before the RO step, since the membrane material can be heavily damaged by this chemical. Sodium bisulfite is commonly used to quench residual chlorine (Bucs et al. 2018). An alternative to chlorination is ozonation. Ozone decomposes rapidly and spontaneously and forms hydroxyl

free radicals, which are strong oxidants able to degrade the phospholipidic membrane of microbial cells. Unlike chlorine, chlorine dioxide and chloramines, ozone cannot be stored and must be produced onsite. UV treatment has been used for disinfection since the late 1990s (Al-Juboori and Yusaf 2012). Besides denaturing the cell membrane, UV light can also attack DNA, resulting in an additional mechanism for pathogens deactivation. However, even if most of the cells are removed from the feed and almost no organic compounds are fed to the RO unit, biofouling will still occur, although it will be retarded. The few residual microorganisms escaping the disinfection treatment will receive over time a large amount of nutrients on which they can feed (Maddah and Chogle 2017). Therefore, sooner or later the problem of biofouling must be tackled.

Among all types of fouling, biofouling is the most likely to occur in RO modules used to treat the hydrolysate coming the HR. Cleaning cycles targeting biofouling have to be conceived to restore the membrane performance. Given the structure of the polymeric composite membranes used for RO, no physical cleaning can be performed other than increasing the cross-flow velocity inside the feed channel. Therefore, chemical cleaning remains the only effective option for biofouling removal. Chemical cleaning requires the flushing of cleaning agents inside the membrane module. The substances used are bases, acids, enzymes, chelating agents or biocides, depending on the kind of fouling that needs to be treated. An example of cleaning agent used to remediate biofouling is sodium dodecyl sulphate (SDS), which is an anionic surfactant able to bind to the lipophilic fraction of the EPS matrix and dissolve it for a better removal (Creber et al. 2010). Biocides can be either dosed into the system or used for periodic shock disinfection (Baker 2004). Some examples are formaldehyde, hydrogen peroxide or peracetic acid. Monochloramine 2,2-dibromo-3-nitrilopropionamide (DBNPA) could successfully inactivate cells on a fouled membrane, but did not restore flux. Therefore, it is recommendable to continuously dose it in the feed, rather than use it for fouling remediation (Siddiqui et al. 2017). One major drawback of chemical cleaning is the reduction of the membrane lifetime and the production of a waste, that must be treated before discharge (neutralization, inactivation of the enzymes, etc.).

The strategies applied to mitigate and control fouling are mainly pretreatment, the optimization of the operating condition with a view to limiting biological growth (pH, temperature, flux, spacer configuration) and the development of effective cleaning cycles. Besides, membrane coating and the optimization of feed spacer design are also possible ways to address the problem.

1.6 Biofilm sensors

Biofilms are object of interest in different technical applications. They do not only represent a threaten to membrane performance in pressure driven systems. Productive biofilms can be used to sustainably produce biopolymers or platform chemicals (Hackbarth et al. 2020). In waste water treatment, biofilms can contribute to purification by consuming nutrients (Wu et

al. 2021). The reactor designs for the exploitation of biofilm metabolism range from membrane bioreactors (MBR) to moving bed biofilm reactors (MBBR) to bioelectrochemical systems (Herrling et al. 2017; Fortunato et al. 2020; Hackbarth et al. 2020). The relevance of biofilms in such systems underlines the need for a reliable biofilm quantification. So far, several imaging techniques have been used to investigate biofilm development. However, most of them are limited to laboratory applications, given their complexity and the impossibility to integrate them in industrial plants. The need for more versatile solutions to gauge bioaccumulation inside a system has encouraged the production of biofilm sensors. Biofilm sensors are useful tools that can be easily integrated in a process line, giving a first rough estimation of the amount of biofilm growing on a surface.

Several biofilm sensors are already available on the market. They are based on different measuring principles. This gives the chance to select the sensor that better fits the desired application. ALVIM Srl (Genova, Italy) produces biofilm monitoring systems that measure the current density on a metallic surface generated by the metabolism of a biofilm. This sensor was applied for biofilm monitoring inside a RO desalination plant and used as a chlorination triggering device (Pavanello et al. 2011). After chlorination, the sensor signal dropped, indicating that the cleaning was efficient and that the sensor can be used to estimate in real time the amount of biofilm in the pipes of the desalination plant. However, a minimum concentration of dissolved oxygen is a prerequisite for the functioning of the sensor. In anoxic process lines, like that of anaerobic digestion, this requirement cannot be fulfilled.

Another working principle is that of optical sensors (Mittenzwey et al. 2006). Usually, these sensors are provided with a pulsing light source. A light detector is placed in front of the source and measures the transmittance of the medium in between. The attenuation of light due to the presence of biofilm is then quantified and used to gauge biomass accumulation. The main drawback of such a measuring principle is that light can also be absorbed by compounds present in the feed, leading to attenuation of the transmitted beam and thereby an overestimation of biofilm.

Thermal sensors can measure the deposition of biofilm on a surface without the need for dissolved oxygen in the solution and are not susceptible to turbidity. The biofilm growing on a surface reduces the global heat transfer coefficient. To quantify this impact on heat transfer either a sinusoidal heat power signal or a continuous heat power is applied to the surface (Reyes-Romero et al. 2014; Netsch et al. 2022). In the first case, the temperature oscillations of the medium are sampled by a probe and undergo a numerical dynamic analysis, that returns the amplitude and phase shift of the signal. This shift contains information about the biofilm thickness and composition.

Lagotec GmbH (Magdeburg, Germany) proposes a solution based on the second approach, where the power supply is continuous. In this case, a probe measures the temperature of the fluid and another probe measures the temperature of the surface where biofilm is expected to grow. A heater provides thermal energy to the surface. The amount of biofilm is estimated

according to the heat power (\dot{P}) needed to maintain a preset temperature difference (ΔT) between the surface and the fluid (Fig. 1-7). The sensors provided by Lagotec GmbH represent a robust option for the estimation of biofilm thickness. These sensors were applied to monitor biofilm formation in drip irrigation systems (Wagner and Horn 2017). The irrigation drippers were fed with pretreated wastewater. The aim of the study was to characterize the drippers, to relate their structure with the irrigation performance and to investigate cleaning strategies. Thanks to this study, the DEPOSENS[®] biofilm sensors were established as online sensor for biofouling monitoring. Based on the collected data, operational guidelines for the utilization of the sensors were developed. Specifically, a signal between 40 and 47 a.u. (auxiliary unit) was defined as a “warning sign”, that justified the cleaning of the drippers (for instance with NaOCl). Thereby, a knowledge-based procedure for biofouling control was adopted. A similar concept could be applied to RO systems. The sensor might be integrated in a RO plant and its signal might be used to infer the amount of biofilm on the membrane. Visual information about the biofilm growing on the sensor and on the membrane would help interpreting the sensor signal. A concise review of the imaging techniques for biofouling visualization is presented in the next section.

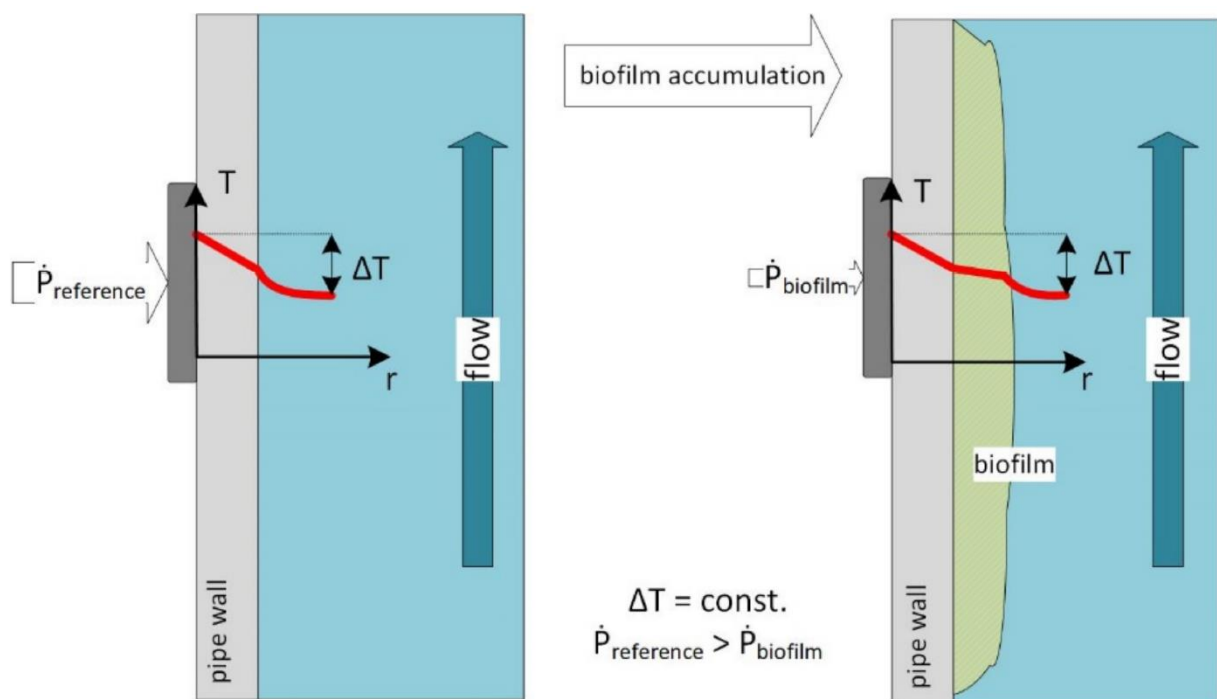


Fig. 1-7: Working principle of the DEPOSENS biofilm sensor. The sensor detects changes in the heat transmission and generates a signal, which is proportional to the thickness of the biofilm (taken from Netsch et al. 2021).

1.7 Imaging techniques for the visualization of biofouling on membranes

The observation of biofilm growth can help to develop strategies to minimized biofouling. Knowing under what conditions biofilms grow faster or acquire specific properties which are

detrimental for membrane filtration (for instance compactness), can help finding the most convenient way to operate RO delaying fouling formation. Another option is “biofilm engineering”, which consists in the condition of biofilm in a way that leads it to possess qualities that are advantageous for the specific scope (Desmond et al. 2022). Biofilm – and more in general fouling – imaging has been applied in research to gather information about the structure of the deposit on the membrane. The most popular techniques are: light microscopy (LM), confocal laser scanning microscopy (CLSM), atomic force microscopy (AFM), scanning electron microscopy (SEM), oxygen planar optode (OPO), magnetic resonance imaging (MRI) and optical coherence tomography (OCT) (Vallarades Linares et al. 2016). Probably the cheapest and easiest technique to perform fouling imaging is LM. The main limitation of LM is the low magnification and only allows for the characterization of the macroscopic structure of the fouling layer (Bulut et al. 2014). All other techniques have higher magnification and resolution, allowing for a better description of the fouling layer morphology. Benecke used LM to image the surface of a fouled membrane (Benecke 2018). The fouling layer was mostly constituted by NOM and gypsum. The microscopic analysis combined with a chemical characterization of the fouling layer permitted to conclude that the adsorption of NOM onto the gypsum subcritical nuclei retarded crystal growth, thereby extending the observed induction time. As already mentioned, there are numerous options for the choice of the suitable imaging technique for fouling description. However, CLSM, MRI and OCT are three of the most applied biofouling imaging techniques for engineering purposes.

CLSM is a fairly recent imaging technique. The first studies applying CLSM to investigate microbial communities date back to the 1990s. Over the years, CLSM gained importance as new stains became available on the market and new ways to interpret the acquired data were developed (Neu and Lawrence 2014). In CLSM a light source illuminates the sample, which reflects light at different optical planes along the depth. All beams being reflected outside the focal plane are excluded by a pinhole (confocal aperture). In this way, only the light coming from a thin region of the sample reaches the detector, resulting in a crisp image. CLSM is mostly used to image biological samples. It is often used to acquire stacks of optical sections at different depths that are later plied up together to obtain pseudo-tridimensional pictures. With multichannel devices, it is possible to use several fluorochromes simultaneously (Neu and Lawrence 2014), allowing for the detection of several compounds at ones. CLSM is a powerful tool when it comes to analyze the biofilm composition. Additionally, it can also be used to characterize the biofilm structure at the microscale (Wagner et al. 2010). Image analysis software for the calculation of surface coverage of the target compounds at different planes along the sample depth are commercially available. CLSM has been applied to investigate the distribution of EPS-glycoconjugate and nucleic acids inside a biofilm growing on a NF membrane used for swimming pool water treatment (Peng 2016). If the biofilm is composed by a pure culture, it is also possible to stain it in a way that allows to quantify death cells and live cells (Suwarno et al. 2014). This is particularly useful when the effect of biocides

needs to be assessed. The main limitation of CLSM is the impossibility to use it as online tool for biofilm monitoring. In fact, the sample must be removed from the environment for staining. Moreover, the need for staining makes CLSM an invasive technique. Therefore, in some cases it is preferable to use methods with lower resolution, but that allow for *in situ* visualization of biofilm, such as MRI and OCT.

MRI is based on nuclear magnetic resonance (NMR). NMR devices generate a magnetic field affecting only isotopes with an intrinsic magnetic moment (Ranzinger 2022). The isotopes population redistribute itself among the available energy states, by changing their spins. The distribution is described by the Boltzmann equation. The direction of the external magnetic field is preferred. Hence the majority of the isotope aligns its spin to it, generating a magnetization vector along the direction of the external magnetic field. Then, a coil produces a pulsing electric field at a specific frequency, that excites the isotopes. The pulsing electric field alters the direction of the magnetization vector. Starting from the excitation, the magnetic field is turned off. At this point relaxation starts. The time required for the relaxation is specific for each substance. The signal of the relaxation is received by a coil, that detects the magnetic field gradient. This gives the possibility to resolve the image according to the composition of the sample. MRI was applied to study the biofilm development in a spiral wound RO membrane module (Fridjonsson et al. 2015). The module was placed in the bore of the NMR device and the pressure drop along the module was measured during a fouling experiment. The NMR signal increased before the pressure drop, proving to be an effective method for the detection of biofilm formation at an early stage. Moreover, the spatial resolution of the acquired images allowed for the localization of fouling and a detailed description of its development. MRI was also used to characterize filtration and analyze flow profiles in a multichannel hollow fiber UF membrane (Schuhmann et al. 2019). Sodium alginate was used as model substance to mimic the EPS. Experiments were performed with and without CaCl_2 in the feed. The presence of Ca^{2+} ions impacted the fouling mechanism leading to a more compact and uniform layer along the length of the module. This was explained by the strong interaction of alginate with divalent ions, leading to the formation of a gel. In contrast, when no Ca^{2+} were present in the feed, the fouling layer was thicker at the end of the module and MRI could detect a steeper radial concentration profile, resulting from concentration polarization. Penetration depth is a limiting factor in most imaging methods. MRI is virtually not limited from this perspective and the sample can be completely penetrated. Thanks to this key-feature, it was possible to image entire membrane modules that are usually installed in full scale plants (Creber et al. 2010; Fridjonsson et al. 2015; Schuhmann et al. 2019). This confers MRI an enormous advantage over other techniques. Using a cylindrical coordinates system, it is possible to render the entire module and not only quantify fouling at each spot inside the feed channel, but also describe the flow field and concentration profiles of the solution components.

MRI has a great potential for studying biofilms, but it is rather complex and its administrative and instrumental demand are high. The apparatus is of considerable size too (Wagner et al.

2010). A good alternative to MRI is OCT. In some way, OCT represents a good compromise between CLSM and MRI. It is a nondestructive and online method. Both are advantageous features over CLSM. At the same time, the used instrumentation is rather compact, meaning that no particular requirements are needed for the preparation of the laboratory where the OCT device is placed and a less complex apparatus is needed in comparison with MRI. This makes OCT a rather flexible method. Furthermore, OCT exhibits a higher resolution than MRI and can image comparable sample volumes (Wagner et al. 2010).

Background:

The working principle of OCT is that of an interferometer. A short temporal coherent light source is produced and directed toward a beam splitter (Fig. 1-8). A fraction of the beam is sent to the sample (sample arm), while the other fraction reaches a moving reference mirror (reference arm). The light scattered back by the sample recombines with the light from the reference arm and is sent to a photodetector. The time delay between the two arms generates interference fringes, containing information about the sample structure. The signal is then amplified, filtered with a bandpass filter, demodulated and converted into a digital signal (Schmitt 1999).

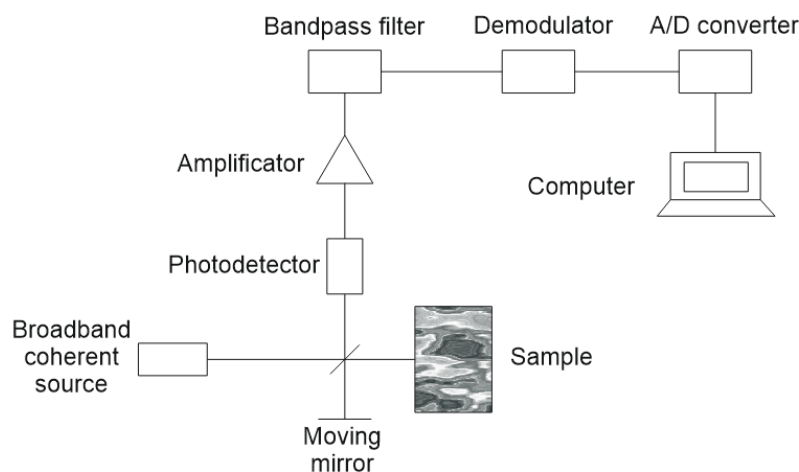


Fig. 1-8: Working principle of OCT. Interferences are generated as the reference beam and the sample beam are recombined.

The light intensity captured by the photodetector is the sum of the mean intensity of the reference arm, the mean intensity of the sample arm and the amplitude of the interference fringes. Basically, OCT imaging systems respond to changes in the refractive index along the depth of the specimen caused by inhomogeneities in its structure. At each transition of the refractive index, light is scattered at a different angle and this is what characterizes the interference fringes.

The mathematical description of the interference phenomenon is given by Eq. 1-8 (Schmitt 1999).

$$I_d = 0.5(I_r + I_s) + Re[\int_{t_1}^{t_2} E_r^*(t + \tau)E_s(t)dt] \quad \text{Eq. 1-8}$$

Where I_d is the intensity at the detector, I_r is the mean intensity of the reference arm, I_s is the mean intensity of the sample arm, E_r^* is the complex conjugated of the reference arm electric field, E_s is the electric field of the sample arm, t_1 and t_2 are the initial and final sampling time and τ is the time delay between the two electric fields. The last term of the equation represents the real part of the cross-correlation product of the sample electric field and the reference electric field. To extract the information from the interference fringes, the Fast Fourier Transform (FFT) is applied to the signal intensity in the time domain. The FFT is a powerful mathematical tool that boils down the problem into a simpler one in the domain of the frequency (Fig. 1-9). In this way, it is possible to extract information about the structure of the sample along its depth (Schmitt 1999). When the coherent light source is pointed at a fixed position, the result is a 1D depth profile, referred to as A-scan. To generate 3D images, the sample is scanned. In this way, several A-scans are collected to produce a B-scan: a 2D image made of the 1D depth profiles joined together. The scanning is repeated many times at different positions, keeping the step between one B-scan and the next one constant (Fig. 1-10). Then, the B-scans are stacked to generate a C-scan: a 3D image of the sample (Wagner et al. 2010).

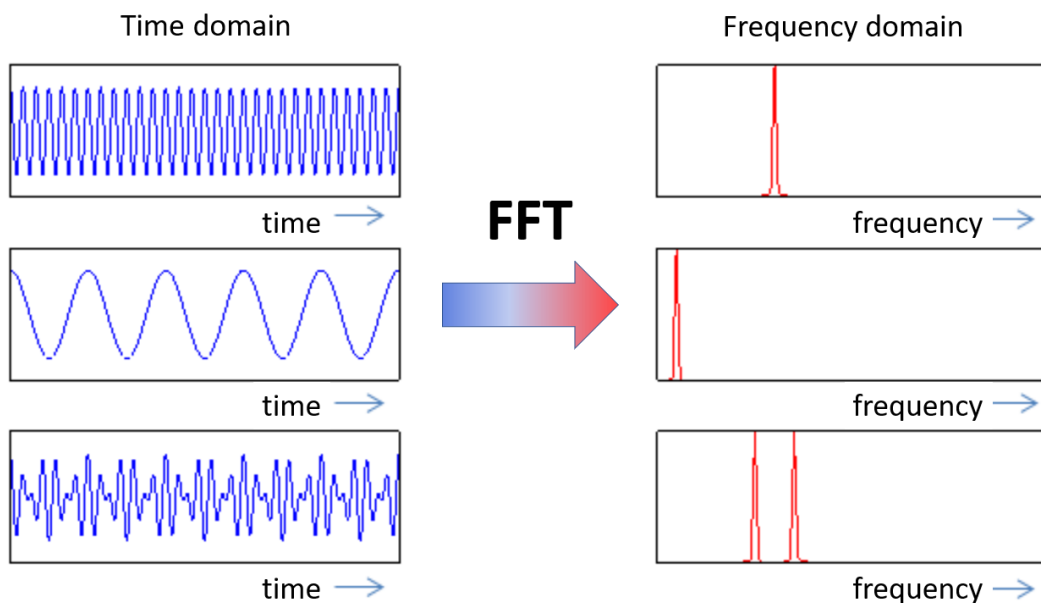


Fig. 1-9: The Fast Fourier Transform (FFT) converts the signal from the time domain to the frequency domain. The information extracted from this spectrum is then used to calculate the depth profile (A-scan).

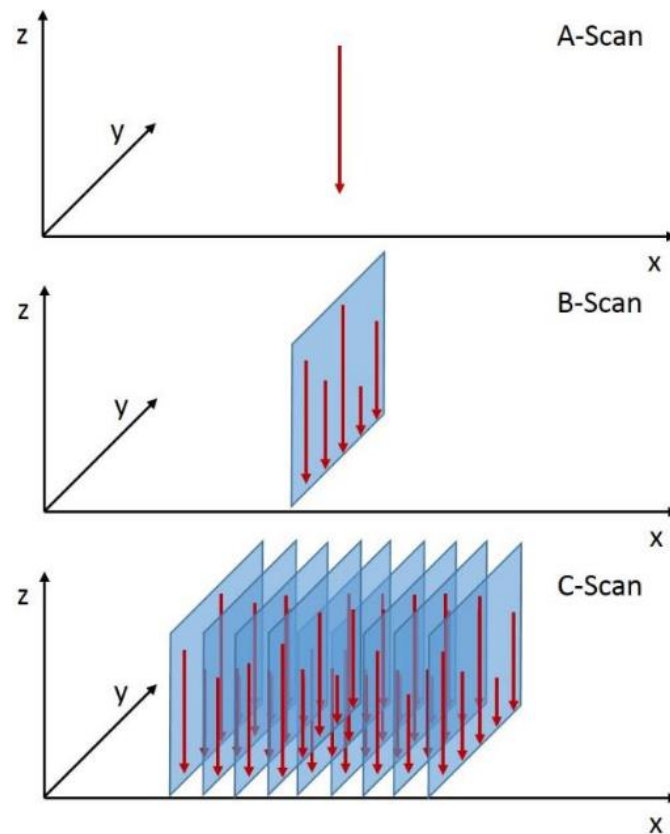


Fig. 1-10: Combining several A-scans together yields a B-scan and stacking more B-scans yields a C-scan (adapted from Min et al. 2013).

Application:

OCT has been used for the study of environmental biofilm and of biofilm-based technical applications, ranging from membrane systems, to biological methanation (West et al. 2016, Pratofiorito et al. 2020, Fortunato et al. 2020).

OCT imaging was performed to quantify biofilm growth in a membrane biofilm reactor used for Hydrogenotrophic biomethanation of carbon dioxide (Pratofiorito et al. 2020). The biofilm grew on the external walls of tubular polypropylene membranes, that were submerged in a liquid medium providing trace elements, inorganic nutrients and vitamins. The biofilm was co-diffusional, meaning that both the electron donor (H_2) and the electron acceptor (CO_2) were delivered from the same side, namely from the lumens of the membranes. A gradient of biofilm growth along the membranes was observed. As the gaseous substrates were fed in excess, biofilm coverage expanded to those membrane regions that remained uncovered up to this point. The authors motivate this fact, with an initial gradient of partial pressure of H_2 and CO_2 along the lumens, caused by the consumption of the substrates. This gradient limited biological growth at the distal end of the membrane. But as soon as the gas supply increased,

biological growth at the distal end was supported. OCT is therefore a useful tool to deepen the understanding of processes where biofilm is involved.

West et al. applied OCT to detect biofilm formation in the feed channel of a membrane module (West et al. 2016). Simultaneously, the feed channel pressure drop was measured. Two different feed spacers were tested. The authors concluded that the amount of biofilm present in the feed channel correlates with the pressure drop and that small-meshed spacers promote a faster biofilm growth. For small-meshed spacers the number of filament junctions per unit membrane surface is higher, which results in a higher protected area for biofilm to start to grow.

OCT was also used to evaluate different physical cleaning strategies in a gravity-driven membrane bioreactor (GD-MBR) (Fortunato et al. 2020). Membrane relaxation cycles were carried out at different frequencies; intermittent air scouring was then performed; finally, relaxation and air scouring were combined. OCT imaging together with pressure drop and flux measurements led to the estimation of biomass hydraulic resistance during the different phases of cleaning. Interestingly, when relaxation was carried out at higher frequency, biofilm thickness increased. However, the specific biomass resistance decreased, so that the overall biomass resistance remained constant. Air scouring decreased biomass resistance, by thinning the deposit layer on the membrane. The combination of air scouring and relaxation, increased biomass roughness and decreased the specific hydraulic resistance. The beneficial impact of biomass roughness on permeation was already reported in another study involving OCT and two-dimensional mass transfer modelling (Li et al. 2016).

Scaling can be also characterized by means of OCT. OCT enabled the in-situ visualization and quantification of scaling in a membrane distillation (MD) setup (Bauer et al. 2019). The share of covered membrane area correlated with flux decline. This proved that the observation of the membrane surface via OCT can actually assess the state of fouling and thereby predict membrane performance decline. Another finding of the work was that the feed spacer does not necessarily induce scaling. In a follow-up study, the same authors investigated the effect of the operating conditions of an MD unit on the scale formation (Bauer et al. 2021). The change from the direct contact (DC) to the air gap (AG) configuration did not imply any significant influence on scaling. In contrast, the increase of temperature speeded up nucleation, leading to the formation of bigger crystals.

1.8 Outline of the work

The present dissertation deals with the optimization of a RO unit for the concentration of VFA in a two-stage production of biogas. For all experiments presented hereby, the same model solution was used as feed. The composition of the solution was formulated to mimic the one of the hydrolysate produced in the HR. Since acetic acid was the VFA with the highest concentration in the hydrolysate acetate/acetic acid was the only organic carbon source in the model solution. Additionally, acetic acid is the smallest VFA and thus an appropriate target compound to evaluate rejection. To allow the cross comparison of the different experiments, the operating conditions were kept the same throughout the work.

The membrane used for the experiments was the XLE membrane (FilmTec Dupont, Wilmington, DE, USA). It is a low energy reverse osmosis membrane, commonly used in water treatment systems and food processing. It was selected, based on its retention properties with respect to VFA and on the relatively high water permeability. Tighter membranes showed better VFA retention values, but had lower values of permeability and could retain better ammonium and other inorganic ions. They were therefore discarded, since a high salinity of the concentrate could inhibit biological growth in the MR. The XLE membrane sheets were laid inside two parallel flat sheet membrane modules (FMM), that reproduced the typical flow conditions inside spiral-wound modules. Moreover, the FMM used in this work allowed for the visualization of the membrane feed side through optical windows.

There are two main aspects that are covered by this work: the optimization of the recovery of VFA via mass balances and the study of biofouling. The recovery must be calibrated based on the need of the specific process. The concentration of VFA in the concentrate must be maximized and at the same time the permeation of VFA through the membrane must be minimized. The recovery of the system plays a role in both these aspects. The issue addressed in chapter 3 is the application of mass balances to answer the question: “How much can one push the recovery to increase the concentration of VFA in the product stream, without undermining the VFA yield?”. The first goal of this dissertation was to test the RO unit performance under different recoveries. Simultaneously, the impact of the osmotic pressure inside the feed channels of the FMM on the separation efficiency was examined.

The second issue addressed by this work is the interplay between spacer fouling, membrane fouling pressure drop along the module and permeability. In chapter 4, the application of OCT to quantify and differentiate the two types of fouling is presented. The feed channels of the FMM were imaged with OCT. Simultaneously, permeability and pressure drop were recorded. A method for image analysis was developed and implemented with a macro. The definition and calculation of two fouling parameters (*ME* for the membrane and *SP* for the spacer) allowed for the differentiation of fouling. A correlation between *ME*, *SP* and the operating parameters was found. The findings can be used to develop fouling control strategies. They are part of a bigger picture, that aims to deepen the understanding of biofouling. In this sense,

chapter 4 deals with fundamental research. The goal was to broaden the base knowledge about fouling in pressure driven membrane processes.

In the last part of the work (chapter 5), a biofilm sensor was applied for the prediction of membrane performance decline. Conventionally, membranes are cleaned as soon as the permeability drops by about 10-15% of the initial value, to avoid severe fouling. However, to support the decision about the right time for cleaning and the total cleaning procedure, an estimation of the amount of biofilm on the membrane can be useful. The use of biofilm sensors in RO systems is a fairly novel approach to optimized membrane operability and might open the way to new control strategies. The biofilm sensor was embedded in a flow cell, which was then integrated in the RO system, in parallel to the two FMM. The conditions (flow, temperature and composition of the solution) inside the sensor flow cell were kept as close as possible to the conditions in the FMM. Several trials were performed, where the membrane permeability and the biofilm sensor signal were constantly recorded. The hypothesis was that biofilm could develop on the sensor surface and inside the FMM simultaneously, making the sensor signal rise as permeability declined (or even anticipating the permeability drop). To corroborate the conclusions drawn from the experiments, biofilm growth on the sensor surface and on the membrane was quantified via OCT. The presented results are critically discussed to provide insights in the application of biofilm sensors for the prediction of permeability decline in RO systems.

2 Preliminary work

To set the boundary conditions for the present study, a preliminary work was performed. Three main aspects had to be addressed before proceeding with the optimization of the recovery and the study of biofouling: the choice of the most suitable membrane for the process, the formulation of a model solution reproducing the real hydrolysate and the definition of a minimum operating pressure. Once these conditions are set, it is possible to perform further experiments. In this way, the comparability of the different results was guaranteed. To cover all three aspects, the first step was a detailed chemical analysis of the hydrolysate. The analysis included the determination of the DOC and of the total nitrogen (TN) (TOC-L CPH, Shimadzu Corporation, Kyōto, Japan), the quantification of the VFA and the inorganic ions with ion chromatography (Metrohm, 790 Personal IC, Herisau, Switzerland) and the quantification of the metals (ICP-OES, Agilent, Model 5110, Santa Clara, CA, USA). The results of the characterization of the hydrolysate are presented in the appendix 1-1. The experimental setup used for the preliminary work is described in detail in chapter 3.

2.1 Choice of the membrane

After a literature review, six membranes were selected and their clean water flux was tested: NF-245, NF-90, XLE, LE, BW30LE, BW30HR (FilmTec Dupont, Wilmington, DE, USA). The measurements were performed in duplicates with demineralized water under 25 °C and 12 bar in crossflow modus. The crossflow velocity was 0.2 m s⁻¹. Fig. 2-1 shows the comparison between the permeability values of the six membranes. The membranes with the highest permeability are the two nanofiltration membranes, NF-245 with 8.9 L m⁻² h⁻¹ bar⁻¹ and NF-90 with 8.7 L m⁻² h⁻¹ bar⁻¹, respectively. The BW30HR showed the lowest permeability to clean water (3.2 L m⁻² h⁻¹ bar⁻¹).

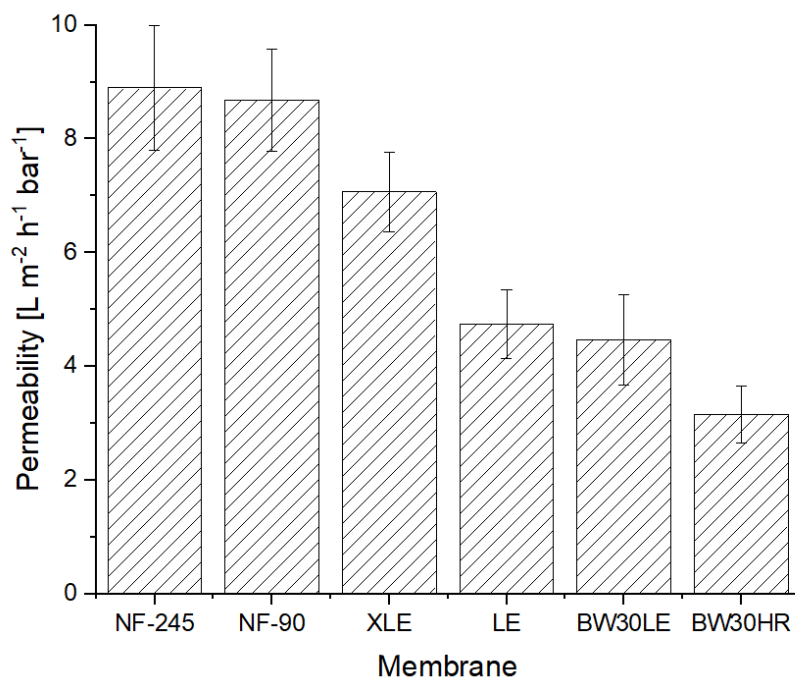


Fig. 2-1: Permeability of different membranes at 25 °C and 12 bar (measured with demineralized water).

To further characterize the six membranes, their molecular weight cut-off (MWCO) was determined using a solution of ethylene glycol, glycerin, glucose, maltose, raffinose and polyethylene glycol (PEG, molecular weight 1000 g mol⁻¹). Tab. 2-1 displays the composition of the solution that was prepared to determine all MWCO. Filtration was performed at 25 °C, 8 bar and 0.2 m s⁻¹ in crossflow modus. The samples from the feed and the permeates were analyzed with size exclusion chromatography with online detection of dissolved organic carbon (SEC-OCD). The separation was performed with a Toyopearl column (HW-50S, 30 μm, 250 x 20 mm, Dr. Maisch GmbH, Germany). The SEC-OCD flow scheme and the method used for the measurements are described by Alvarado Munguía, 2022. The concentration of each component in the feed and in the permeate was obtained integrating the curves in the chromatograms. The retentions were calculated with Eq. 2-1:

$$R (\%) = \frac{C_f - C_p}{C_f} \quad \text{Eq. 2-1}$$

Where C_f is the concentration of the component in the feed and C_p the concentration in the permeate. Fig. 2-2 depicts the retention of the six membranes for all compounds expressed as a function of their molecular weight. PEG 1000 is retained less than raffinose (molecular weight 594 g mol⁻¹) by all membranes except the BW30HR. This might be explained by the linear structure of PEG. Although its molecular weight is higher than the one of raffinose, the

elongated shape of PEG allows for higher permeation in comparison to raffinose. Tab. 2-2 shows the MWCO of the membranes. The indicated values correspond to a retention of 90% obtained after interpolation of the data. Most of the MWCO are higher than 88 g mol^{-1} , which is the molecular weight of butyric acid. Acetic acid and propionic acid have even smaller molecular weights: 60 g mol^{-1} and 74 g mol^{-1} . However, size exclusion is not the only mechanism by which VFA are retained by NF and RO membranes. Electrostatic repulsion also plays a role in the retention of these compounds. It follows that VFA can still be well retained by a membrane with a MWCO higher than their molecular weight. All molecules used in this work for the determination of the MWCO are neutral in a broad range of pH. That means, the MWCO showed hereunder do not consider electrostatic repulsion effect.

Tab. 2-1: Composition of the solution used to determine the MWCO of the six membranes.

| Component | Molecular weight [g mol^{-1}] | Concentration [mg L^{-1}] |
|-----------------------------|--|--------------------------------------|
| Ethylene glycol | 62 | 37 ± 5 |
| Glycerine | 92 | 32 ± 1 |
| Glucose | 180 | 39 ± 6 |
| Maltose | 342 | 40 ± 8 |
| Raffinose·5H ₂ O | 594 | 26 ± 4 |
| PEG 1000 | 950 – 1050 | 24 ± 5 |

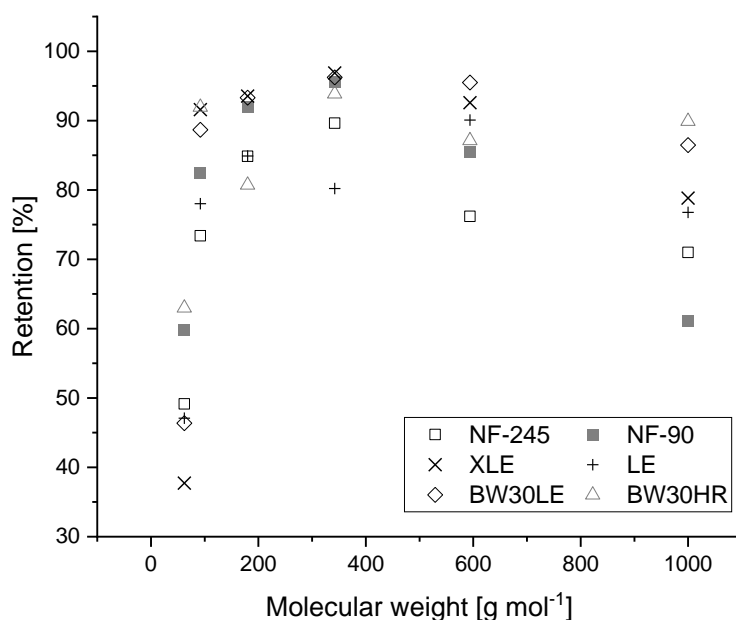


Fig. 2-2: Retention of the six membranes for compounds of different molecular weight.

Tab. 2-2: MWCO of the six membranes.

| Membrane | MWCO [g mol ⁻¹] |
|----------|-----------------------------|
| NF-245 | 340 |
| NF-90 | 180 |
| XLE | 90 |
| LE | 80 |
| BW30LE | 140 |
| BW30HR | 90 |

On the base of the clean water flux results, three membranes were further selected, each from a different range of permeability: NF-245, XLE and BW30HR. NF-245 is a nanofiltration membrane used for dewatering and concentrating liquid foods; XLE is a low energy reverse osmosis membrane, commonly used in water treatment systems and food processing; BW30HR is a reverse osmosis membrane used for brackish water desalination. The idea was to pick one membrane from each range of permeability: above $8 \text{ L m}^{-2} \text{ h}^{-1} \text{ bar}^{-1}$, between 4 and $8 \text{ L m}^{-2} \text{ h}^{-1} \text{ bar}^{-1}$ and below $4 \text{ L m}^{-2} \text{ h}^{-1} \text{ bar}^{-1}$. The membranes were tested in terms of their separation performance. The solution used to evaluate the rejection of the different membranes was made of NH_4Cl (600 mg L^{-1}) and acetate/acetic acid as only organic carbon source (3 g L^{-1}). Acetic acid was the VFA with the highest concentration in the hydrolysate. Experiments were performed in duplicates at pH 5.0 and pH 6.0 and at 8, 12 and 16 bar. The two values of pH were chosen to test the membranes performance at the operating limits of the HR. The pH was adjusted by dosing NaOH into the solution. The temperature was set to $25 \text{ }^\circ\text{C}$. The rejection of acetic acid and ammonium (measured as TN) was quantified analyzing the feed and the permeate using a carbon analyzer (TOC-L CPH, Shimadzu Corporation, Kyōto, Japan). The rejection was calculated according to Eq. 2-1.

Fig. 2-3 and Fig. 2-4 depict the retention of the membranes with respect to acetic acid and ammonium at pH 5.0 and pH 6.0, respectively. In general, the retentions of all membranes with respect to DOC is higher at pH 6.0. This is due to a higher dissociation degree of acetic acid with respect to pH 5.0. The dissociation degree can be calculated with the Henderson–Hasselbalch equation, knowing that the acidic dissociation constant of acetic acid is $\text{pK}_a = 4.76$. At pH 5.0 63.4% of the acetic acid is present in the form of acetate, which is negatively charged and is repulsed by the electrostatic force exerted by the membrane. This percentage increases to 94.6 % at pH 6.0. This effect is more pronounced for the NF-245, which is in accordance with Li et al. (2008), who stated that NF membranes performances are more affected by changes of the pH than RO membranes. At pH 5.0 the BW30HR showed the best retention values with respect to DOC and TN. At higher pH the separation performance of the XLE significantly improved and became competitive with the BW30HR performance.

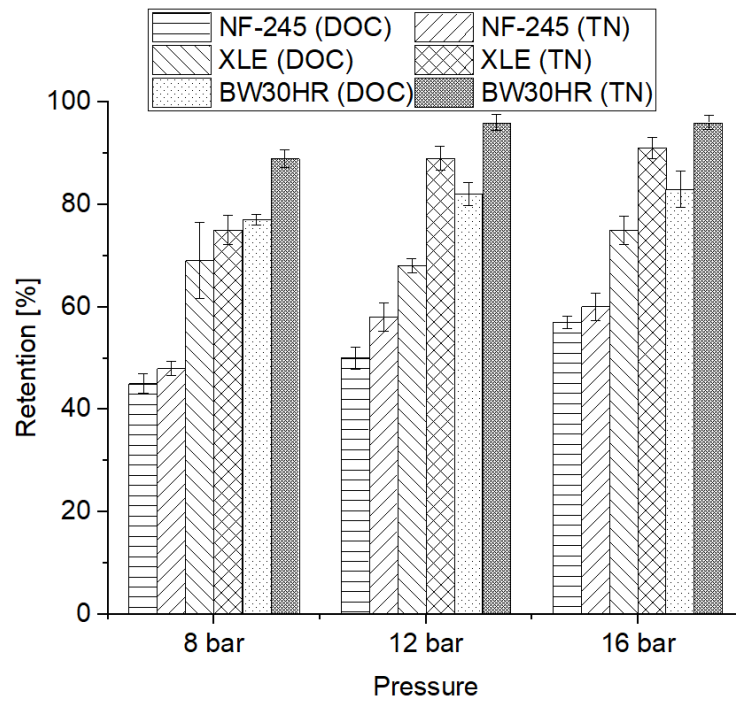


Fig. 2-3: DOC and TN retention of the three selected membranes at pH 5.0 and 8, 12 and 16 bar.

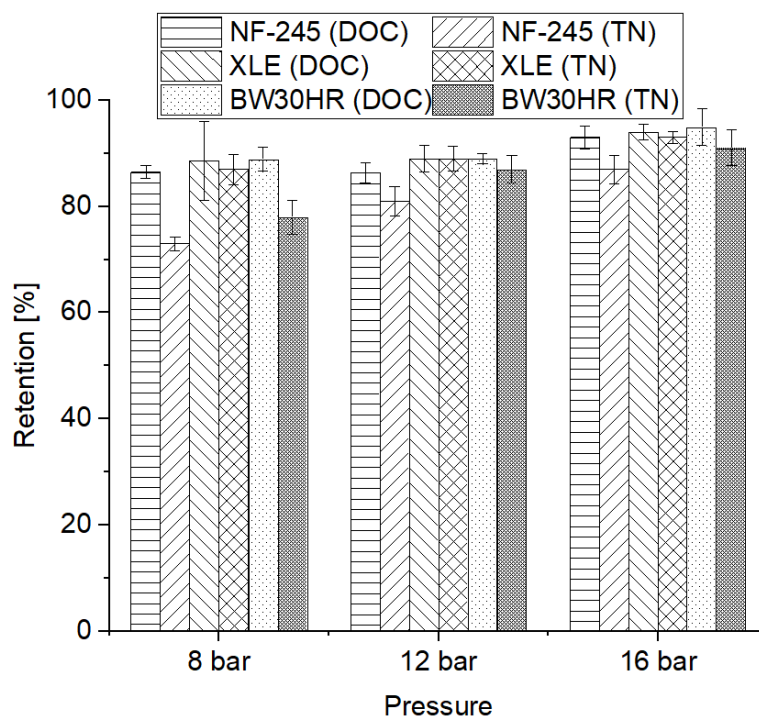


Fig. 2-4: DOC and TN Retention of the three selected membranes at pH 6.0 and 8, 12 and 16 bar.

The BW30HR is characterized by high retention values and low permeability. In contrast, the NF-245 provides high flux, but poor DOC rejection. The XLE represented a tradeoff between high rejection and good permeability and was therefore selected for the further experiments.

2.2 Formulation of a model solution and choice of the operating pressure

Another point to address was the formulation of a model solution that would mimic the hydrolysate produced in the HR. The composition of the hydrolysate can vary significantly due to several factors (changes in the microbial community, temperature, substrate, etc.). To guaranty the reproducibility of the results, it was decided to work with a synthetic solution containing the most abundant VFA in the hydrolysate. These were: formic acid, acetic acid, propionic acid, butyric acid and lactic acid. However, it was reported that acetic acid is retained the least among all VFA – except formic acid – by RO membranes (Bóna et al. 2020). To confirm this finding, it was decided to treat the real solution with the XLE membrane and analyze the retention values for the main VFA via ion chromatography (Metrohm, 790 Personal IC, Herisau, Switzerland). The hydrolysate was pretreated with MF (0.45 μm nominal pore size) to remove the suspended solids. After MF, the pH of the hydrolysate was 5.7. The filtered solution underwent RO treatment for three days before analyzing the feed and the permeate samples. This minimized the impact of the short-term adsorption of the VFA to the RO membrane and could deliver more solid results. The pressure was set to 16 bar and the temperature to 37 °C, a realistic value, considering that, in the frame of the ProBioLNG project, the HR was operated under thermophilic conditions (55 °C). Heat losses due to the microfiltration and the pumping through the pipes are difficult to gauge and depend from the layout of the whole biogas plant as well as from the outside temperature, with possible fluctuation over the year. It was assumed that, if the MF and RO units are placed in the vicinity of the HR, heat losses might be lower than 20 °C. This would be also advantageous for the operability of the MR, which is supposed to run at mesophilic conditions (between 30 °C and 37 °C). Moreover, most microorganisms have their optimum growth rate around 35 °C. Running the experimental RO unit at 37 °C with the real hydrolysate had the advantage of promoting biofouling, thereby allowing a first qualitative visual estimation of the amount of biofilm on the membrane at the end of filtration.

Fig. 2-5 shows the retention values for the different VFA as well as for the DOC and the TN. 75% of acetic acid was retained by the membrane. The retention values of all other VFA were at least 80%. As Bóna et al. stated, VFA selectivity in RO is probably governed by size (Bóna et al. 2020). That is, the compound with the smallest solvated volume is retained the least (in this case acetic acid). Moreover, the dissociation degree plays less of a role, since butyric acid and propionic acid have similar pK_a as acetic acid (near 4.8). In the case of lactic acid, which was retained the most, dissociation might have indeed played a role. The dissociation constant of lactic acid is 3.9, significantly lower than the one of the other VFA. At pH 5.7, almost all lactic acid dissociated into lactate. Therefore, charge repulsion effect strongly favored the retention of lactic acid over the other VFA.

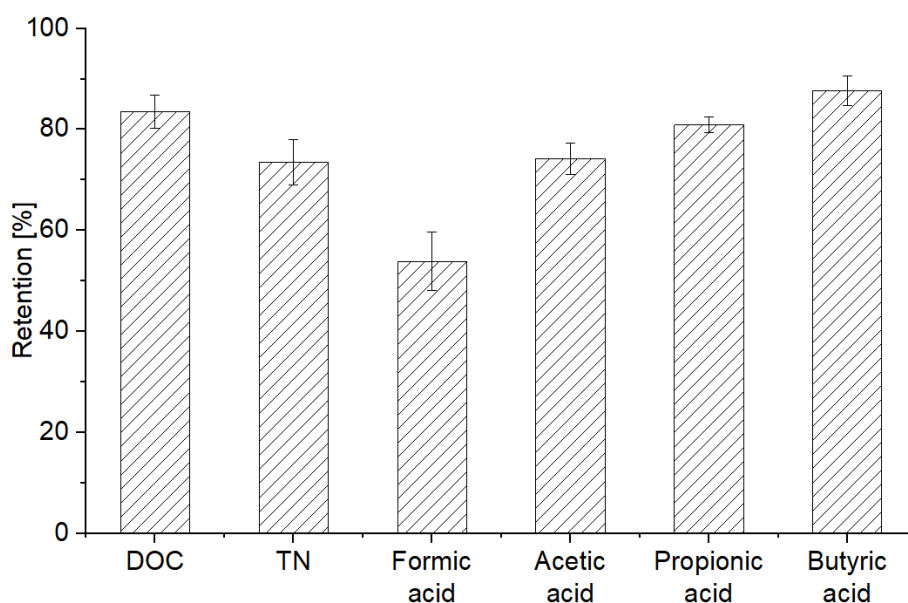


Fig. 2-5: Retention values of the XLE membrane for DOC, TN and the main VFA in the hydrolysate at 12 bar and 37 °C.

Knowing that acetic acid is retained less than propionic, butyric and lactic acid, it was decided to formulate a model solution with acetic acid/acetate as only VFA. Working with such solution guarantees conservative DOC retention values, thereby avoiding the overestimation of VFA retention. The model solution did not contain formic acid either, although its retention was lower than the one of acetic acid (only 54%). This choice was justified by the relatively low concentration of formic acid in the hydrolysate (120 mg L^{-1}). Even if all formic acid could escape the XLE membrane, the related amount of organic carbon ending up in the permeate would be neglectable in comparison to the other VFA being retained.

Calcium acetate was combined with acetic acid as organic carbon source for the solution. This had the further advantage of providing a high amount of Ca^{2+} in the model solution, which was the inorganic ion with the highest concentration in the hydrolysate after K^+ . Tab. 2-1 shows the composition of the model solution used to compare the retention of the XLE with respect to the different VFA. $600 \text{ mg L}^{-1} \text{ NH}_4\text{Cl}$ were used to prepare the model solution to provide similar amounts of Cl^- and NH_4^+ as in the hydrolysate. The composition of the synthetic solution is displayed in Tab. 2-2. The pH of the model solution was 5.4, which is near the target value and represents realistic benchmark for the pH of the HR product treated with MF.

Tab. 2-3: Composition of the model solution used in the present work. Acetic acid and calcium acetate were used to reach the equivalent DOC value of the other main VFA.

| Component | Concentration [g L ⁻¹] |
|----------------------------------|------------------------------------|
| CH ₃ COO ⁻ | 16.9 |
| Na ⁺ | 2.8 |
| K ⁺ | 2.4 |
| Ca ²⁺ | 1.4 |
| Cl ⁻ | 0.4 |
| NH ₄ ⁺ | 0.2 |

Once the composition of the synthetic solution was defined, it was possible to set a minimum operating pressure. The osmotic pressure of a solution can be calculated with the Van't Hoff equation (Eq. 1-1) when its composition is completely known. That is, knowing the concentration of every component allows the calculation of the minimum pressure that needs to be applied to a RO membrane to obtain water flux. Substituting the values of Tab. 2-2 in the Van't Hoff equation returns an osmotic pressure of 12 bar. Considering that during the filtration of real hydrolysate at 16 bar a relatively low flux was recorded (around 4 L m⁻² h⁻¹), it was decided to work at least at 10 bar above the osmotic pressure (22 bar).

3 Impact of the recovery on concentrating acetic acid with low-pressure reverse-osmosis membranes

(Published in MDPI Membranes)

Considering the role of RO in the two-stage production of biogas, the RO unit must be designed and operated with a view to the maximization of the VFA concentration in the methane reactor. At the same time, the amount of VFA that gets lost in the permeate must be minimized. This chapter focuses on the optimization of the separation efficiency of acetate by tuning the recovery of the system. This investigation is necessary to set the boundary conditions of the process. A detailed study of long-term issues (i.e. biofouling) will be object of the following chapters. At this point, the discussion centers on a more direct and short-term related topic: the impact of the recovery on the acetate reclamation. Since the study was conducted using a model solution, all components were known. This allowed for the calculation of the osmotic pressure in the feed channel based on the analysis performed on the samples. This calculation could thus support the results obtained with the mass balances, providing a physical explanation of the phenomenon and quantifying the driving force for water flux through the membrane.

3.1 Introduction

The interest in anaerobic digestion processes for biogas production and for the production of platform chemicals (such as lactic and propionic acid) has increased in the last decades (Li et al. 2008; Valentino et al. 2019; Ali et al. 2020). One process that is being studied in the area of biogas production is the two-stage fermentation process, where biomass is first degraded to simpler organic compounds— mostly volatile fatty acids (VFA)—via hydrolysis and acidogenesis and later converted into methane by methanogens in a second reactor (Kumanowska et al. 2017; Ravi et al. 2018). Electrodialysis, pervaporation, membrane distillation, membrane contactor, forward osmosis, reverse osmosis, and nanofiltration appear to be valid techniques to concentrate these low-molecular weight substances, increase the organic load, and improve their availability for the last step of the biogas production or for platform chemicals production in general (Aktija et al. 2020; Zhu et al. 2020; Blandi et al. 2019). Among them, nanofiltration (NF) and low-pressure reverse osmosis (LPRO) have been gaining importance for VFA recovery in recent years, due to their high retentions with respect to these chemicals. Moreover, they allow the separation of VFA from other molecules, such as sugars (Atasoy et al. 2018). Tab. 3-1 lists different membranes for VFA recovery applied in the literature.

Some effort has already been made to better understand the mechanisms governing the separation of organic acids from aqueous solutions with NF and LPRO membranes. A previous study showed that 80% of acetic acid can be retained using NF-270 membranes, at a concentration in the feed of 500 mg L⁻¹, a pressure of 2.8 bar and pH 7.3 (Choi et al. 2008). At

pH 7.3, acetic acid is totally dissociated in the solution and can easily be rejected by the negatively charged NF-membranes. However, for solutions with lower pH value, a tighter membrane might be applied in order to achieve higher rejection rates. In fact, pH value plays a double role in the separation of organic acids: it influences the membrane surface charge and the dissociation of the acids. In more acidic solutions, the fraction of dissociated VFA becomes smaller, and the negative surface charge of the membrane is neutralized by the hydronium ion in water. Bellona and Drews showed that acetic acid ($pK_a = 4.76$) can be retained up to 60% by the NF-90 membrane at 5.5 bar when the pH is 5.5 (Bellona et al. 2005). The two researchers also measured the Zeta potential of the membrane, relating a negative Zeta potential with the enhancement of the retention of negative species, confirming the effect of pH value on the rejection of VFA. Verliefde et al. showed that the acetic acid retention decreased from 98% to 79% when the pH is shifted from 8 to 5 at 25 bar (Verliefde et al. 2008). In this range, the fraction of dissociated acid varies from 100% at pH 8 to 63% at pH 5. Relevant VFA show similar behavior, as they all have pK_a in the range between 4.75 and 4.9.

The presence of inorganic salts can also affect the retention of organic molecules, as pointed out by previous works (Umpuch et al. 2010; Zacharof et al. 2015; Zhu et al. 2020). Lactic acid was retained by a Desal-5 DK membrane 30% less when the concentration of NaCl in the feed was increased from 0 to 1 M (pH between 6 and 7) (Umpuch et al. 2010). According to the authors, NaCl screens the electrostatic repulsion between membrane and lactate. This effect becomes more evident for solutes with a molecular weight much smaller than the molecular weight cut-off (MWCO) of the membrane, since for these compounds, charge effect plays a dominant role in the rejection mechanisms. In general, higher ionic strength leads to a neutralization of the membrane, with a consequent reduction of the electrostatic repulsion. Similar results were obtained by Choi et al. (Choi et al. 2008). This underlines the importance of considering the matrix when it comes to evaluating the separation performances.

Multicomponent systems can show different retentions than single-component solutions. For instance, acetic acid is retained 11.5% and 7.8% more, when it is mixed with butyric and propionic acid, respectively (Laufenberg et al. 1996). Bóna et al. performed a statistical analysis on several runs of filtration of mixtures containing acetic, propionic, and butyric acid using NF and LPRO membranes (Bóna et al. 2020). As expected, NF showed higher permeability ($4.2 \text{ L m}^{-2} \text{ h}^{-1} \text{ bar}^{-1}$) and lower retentions (on average 50%, 64%, and 74% for acetic, propionic, and butyric acid, respectively) compared to LPRO ($2.5 \text{ L m}^{-2} \text{ h}^{-1} \text{ bar}^{-1}$), 80% retention for acetic, and 84% for propionic and butyric acid) and was more susceptible to changes in the pH.

Another important factor determining the retention of VFA is the size of the compounds that undergo the filtration. NF/LPRO membranes are dense composite membranes, and the diffusion of smaller chemicals through their active layer is easier than for larger ones. Retention of different molecules in NF/LPRO processes can be linked to several parameters,

such as the molecular weight, the equivalent molar diameter, the Stokes diameter, and the calculated molecular diameter (Van der Bruggen et al. 1999).

Hydrophobic compounds solvate less and flow more easily through the membrane. (Braeken et al. 2005). However, in the case of VFA, hydrophobicity is not determinant. In fact, for short chain organic acids, the carboxylic polar group is predominant and confers a hydrophilic structure to the compound.

LPRO and NF can concentrate VFA but are not able to separate them from one another. However, Zhou et al. were able to separate acetic acid from glucose and xylose in a model hydrolysate by using RO98pHt membranes at a pH of about 3 and 20 bar (Zhou et al. 2013a, 2013b). Furthermore, acidic conditions allow acetic acid to flow through the membrane while bigger uncharged molecules such as monosaccharides, for which size exclusion is the dominant effect, are highly retained. They also investigated the effect of temperature on the retention of the three solutes by NF and LPRO membranes, finding that both the monosaccharides and acetic acid are retained less by NF membranes when temperature increases. On the other hand, LPRO membranes showed only a drop in the retention of acetic acid and not of glucose and xylose, resulting in a better separation. A higher temperature implies an increase in the diffusion of the solutes and a change in the thin-layer structure, where pore size becomes larger.

In spiral wound modules, the choice of the recovery has consequences on the overall efficiency of the separation. The use of continuous pilot plants permits one to simulate the behavior of a spiral wound module when operated at a desired recovery. Moreover, the effect of the recovery on the efficiency of the concentration of VFA has not been deeply investigated so far. In previous studies on continuous pilot plants, experiments were only conducted at a fixed recovery (Roman 2006; Warnecke et al. 2021). The aim of this study is to evaluate the effect of the recovery on the LPRO of a model solution defined to simulate a hydrolysate obtained from biomass hydrolysis. An attempt was made to explain the mechanisms involved, in order to better understand the optimal condition to run the process. The scope was to find out whether a high or limited recovery is desirable, preventing in this way the loss of the acetic acid in the permeate.

Tab. 3-1: Membranes used for VFA recovery.

| Membrane | Material | VFA Recovered | NF/LPRO | Manufacturer | Reference |
|-------------|--------------------|----------------------------------|---------|---------------|-------------------------|
| NF-90 | Polyamide | Acetic acid | NF | FilmTec-Dow | (Bellona et al. 2005) |
| NF-270 | Polyamide | Formic, acetic, butyric acids | NF | FilmTec-Dow | (Choi et al. 2008) |
| XLE | Polyamide | Acetic, propionic, butyric acids | LPRO | FilmTec-Dow | (Zhu et al. 2020) |
| SW30 | Polyamide | Acetic, propionic, butyric acids | LPRO | FilmTec-Dow | (Bóna et al. 2020) |
| RO98pHt | Aromatic polyamide | Acetic acid | LPRO | Alfa Laval | (Zhou et al. 2013) |
| Trisep TS80 | Aromatic polyamide | Formic, acetic, lactic acids | NF | Trisep | (Verliefde et al. 2008) |
| ES10 | Aromatic polyamide | Formic, acetic, butyric acids | NF | Nitto Denko | (Choi et al. 2008) |
| Desal-5 DK | Aromatic polyamide | Lactic acid | LPRO | GE | (Umpuch et al. 2010) |
| Desal HL | Aromatic polyamide | Formic, acetic, lactic acids | NF | GE | (Verliefde et al. 2008) |
| dNF40 | Polyethersulfone | Acetic, propionic, butyric acids | NF | NX Filtration | (Bóna et al. 2020) |

3.2 Materials and methods

3.2.1 Experimental setup

The experiments were performed in a continuously operated laboratory setup (PS Prozesstechnik GmbH, Basel, Switzerland). It consisted of two cross-flow flat sheet membrane modules (active surface $0.279 \times 0.1 \text{ m}^2$, channel thickness 1 mm) connected in parallel (Fig. 3-1). A photograph of one module is provided in appendix 3-1 as well as one of the setup. A similar module was used by West et al. (West et al. 2016). Two equal pieces of XLE (FilmTec Dupont, Wilmington, DE, USA), a polyamide thin-film composite membrane, were used in this work. According to the manufacturer, this membrane has a stabilized salt rejection of 99% (500 ppm NaCl in the feed stream) with a flux of $7.4 \text{ L m}^{-2} \text{ h}^{-1} \text{ bar}^{-1}$. The desired concentrate has to be fed to a methane reactor and must contain a high amount of acetate and, at the same time, not extremely high salinity. Therefore, a tighter membrane was not chosen. Permeate flux, temperature, and pressure were measured continuously throughout the experiments. Experiments were run at 22 ± 0.5 and at 25 ± 0.5 bar. These two pressures were chosen on the basis of the expected osmotic pressure of the feed (10 bar) and the optimal pressure needed to achieve an adequate membrane flux. The temperature was controlled by a heat exchanger placed in the recirculation tank (RT in Fig. 3-1) and kept at 37 ± 1 °C, the temperature in hydrolysis reactors operated at mesophilic conditions.

The cross-flow velocity in the feed channel was set at 0.2 L m s^{-1} . The system can be considered as a black box. The feed is the only entering stream, while the concentrate and permeate are the two streams leaving the system. However, there was an internal recirculation, which made it possible to test different recoveries. Anytime the volume inside the recirculation tank (RT) decreased below 4.8 L a level control unit turned on two pumps, FP and CP. FP pumped fresh medium into RT, while CP pumped the mixture from RT at a lower flowrate than FP. The level control unit turned them off when the level was reached again. In this way, the volume in RT remained practically constant, since the quantity of liquid delivered by FP equaled that pumped by CP plus the volume leaving the system as permeate. The ratio between the flowrates of the feed (Q_f) and the solution withdrawn from RT (Q_c) was varied, in order to evaluate the influence of the recovery on the separation efficiency of the whole process. This ratio was referred to as the concentration factor (CF, Eq. 3-1). Eq. 3-2 clarifies the relation between recovery and concentration factor. The higher CF, the higher the recovery.

$$CF = \frac{Q_f}{Q_c} \quad \text{Eq. 3-1}$$

$$\text{Recovery (\%)} = \left(1 - \frac{1}{CF}\right) \cdot 100 \quad \text{Eq. 3-2}$$

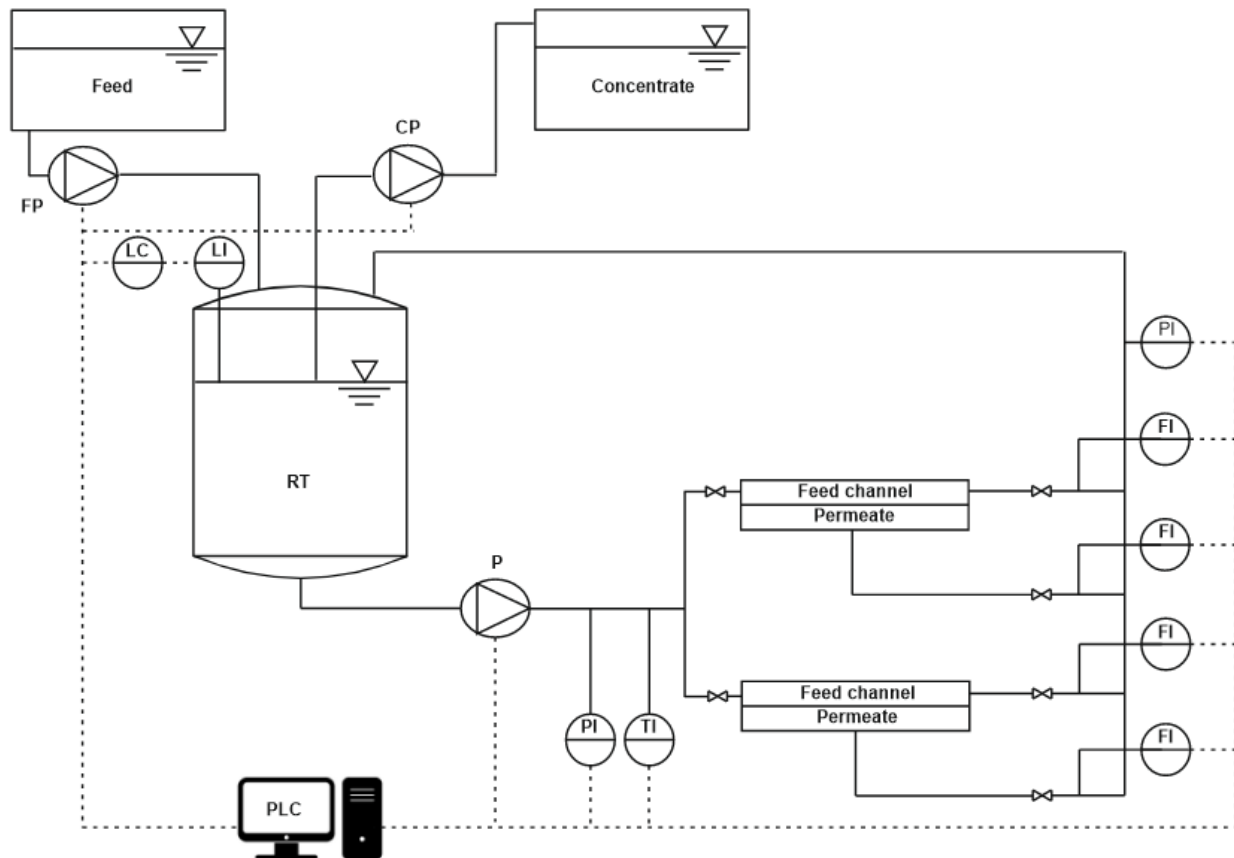


Fig. 3-1: Schematic representation of the system. FP: Feed pump; CP: concentrate pump; RT: recirculation tank; P: pump; PI: pressure indicator; TI: temperature indicator; FI: flow indicator; LI: level indicator; LC: level controller.

3.2.2 Feed solution

The feed solution was prepared with 13 g L^{-1} acetic acid, 5.5 g L^{-1} calcium acetate, 4.8 g L^{-1} NaOH, 3.5 g L^{-1} KOH, and 0.6 g L^{-1} NH_4Cl . These values correspond to a total acetate concentration of 17 g L^{-1} . The pH was 5.4 ± 0.1 , and the electrical conductivity was $17 \pm 0.5 \text{ mS cm}^{-1}$. It was decided to use only acetic acid because previous works showed that its retention is equal or smaller than that of other relevant VFA such as propionate, butyrate, and lactate (Bóna et al. 2020; Jänisch et al. 2019). At this pH, acetate accounts for 80% of total acetic acid, according to the Henderson–Hasselbalch equation. The formulation of the feed was performed based on the hydrolysates, described in the literature by Kumanowska et al. and Ravi et al. (Kumanowska et al. 2017; Ravi et al. 2018).

3.2.3 Sampling and analytics

The compositions of the feed, the concentrate, and the permeate were determined on a daily basis. Dissolved organic carbon (DOC) and total nitrogen (TN) were measured with a carbon analyzer (TOC-L CPH, Shimadzu Corporation, Kyōto, Japan). Since the only nitrogen source in the solution was NH_4Cl , the TN value was proportional to the ammonium concentration.

Inductively coupled plasma optical emission spectroscopy (ICP-OES) (Agilent, Model 5110, Santa Clara, CA, USA) was used to determine the concentrations of cations (Ca^{2+} , Na^+ , K^+). The concentration of Cl^- was measured with ion chromatography (Metrohm, 790 Personal IC, Herisau, Switzerland).

3.2.4 Development of parameters

The focus of the present work is the maximization of acetate in the concentrate of a membrane process (LPRO) for its further use. To compare the quantity of acetate being withdrawn from RT as concentrate with the one in the permeate, the ratio between the concentration of acetate in the two streams (R_c) was defined as follows:

$$R_c = \frac{C_c}{C_p} \quad \text{Eq. 3-3}$$

where C_c (mg L^{-1}) is the concentration in the concentrate and C_p (mg L^{-1}) the one in the permeate. The higher R_c , the higher the efficiency of the separation.

Another important parameter is the ratio between the acetate flowrate in the concentrate and in the permeate:

$$R_w = \frac{W_c}{W_p} \quad \text{Eq. 3-4}$$

where W_c (mg min^{-1}) is the mass flowrate in the concentrate and W_p (mg min^{-1}) is the one in the permeate. R_w simply represents the relation between the overall amounts of acetate flowing in the two streams and indicates how much acetate is being “lost” in the permeate.

The osmotic pressure π was calculated based on the concentrations of ions measured with the different techniques according to:

$$\pi = RT \sum_{k=1}^n i_k C_k \quad \text{Eq. 3-5}$$

where T is the temperature (K), C_k the concentration of the component k (mol L^{-1}), n the number of components, i_k the Van't Hoff coefficient of the component k , and R is the universal gas constant ($\text{L bar mol}^{-1} \text{K}^{-1}$). The osmotic pressure was calculated assuming that the concentrations at the membrane surface mimicked the ones in the bulk, neglecting concentration polarization. The approach used for the calculation of the osmotic pressure is a linear approach, i.e., the Van't Hoff coefficients are independent of the concentration and equal the charges of the considered ions. For acetate, the coefficient equals 0.8, since it is partially dissociated, as discussed in Section 2.2. The assumption of linearity in the range of

concentration of the present work is validated by Nagy et al. (Nagy et al. 2021). In the case of NaCl, as soon as the concentration reaches 4 M, this assumption does not hold anymore.

The acetic acid mass balance over the whole system is represented by Eq. 3-6:

$$Q_A^F = Q_A^P + Q_A^C \quad \text{Eq. 3-6}$$

where Q_A^F is the flowrate of acetic acid entering the system by FP, Q_A^P the flowrate of acetic acid leaving the system in the permeate, and Q_A^C the one being withdrawn by CP. The term concerning the permeate sampling does not appear in the balance, since permeate was continuously disposed and its collection did not interfere with the operation of the plant.

3.3 Results and discussion

3.3.1 Experiment at 22 bar

Data were collected over a period of 15 days during the filtration experiment at 22 bar. After setting CF to the desired value, the sampling was performed at least one day later, to give the system time to stabilize. The average volumetric flowrate of the feed varied significantly, namely from 10 mL min⁻¹ (at a CF of 2.3) to 62 mL min⁻¹ (at a CF of 1.3). This was caused by the strong dependence of the permeate flux on CF. Increasing CF implied a lower flux through the membrane due to the high concentration in the feed channel at constant pressure. In turn, the level in RT decreased more slowly, and the feed and concentrate were pumped in and out less frequently. The total flowrate of the permeate withdrawn from the system varied from 5.8 to 14.5 mL min⁻¹. The average volumetric flowrate of the concentrate varied accordingly from 4.3 to 47 mL min⁻¹. Fig. 3-2 Fig. 3-3 and Fig. 3-4 depict the concentration of acetic acid in the concentrate and in the permeate, as well as the osmotic pressure, the parameters R_c and R_w , and the retention of ammonium and acetic acid as a function of the concentration factor.

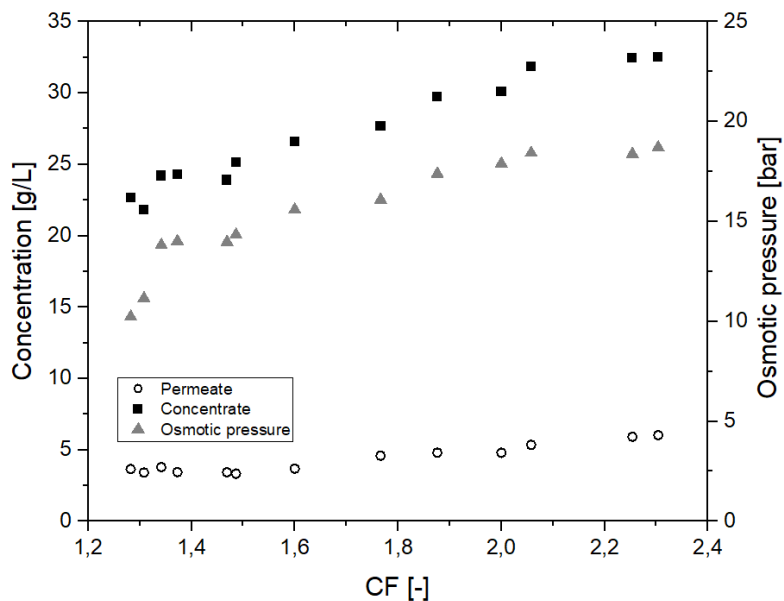


Fig. 3-2: Osmotic pressure and acetate concentrations in the concentrate and in the permeate at different concentration factors CF (22 bar).

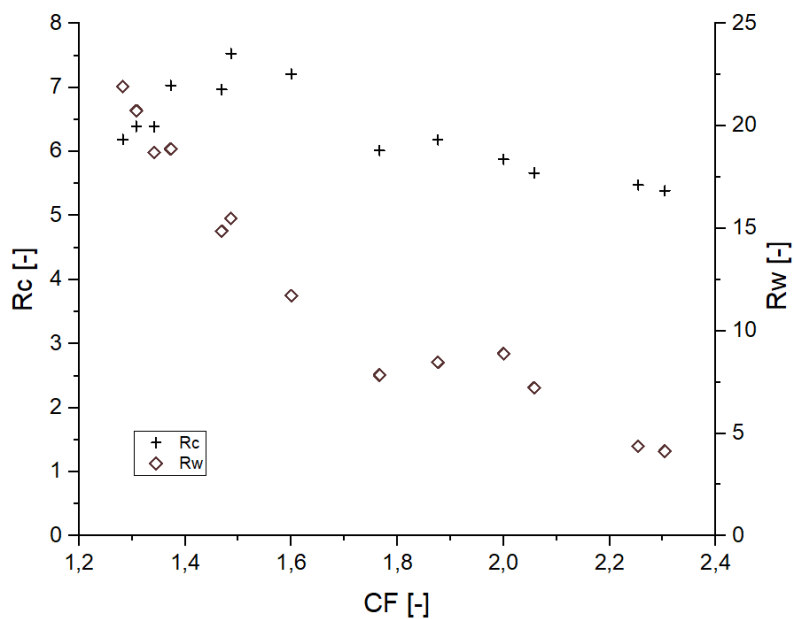


Fig. 3-3: Concentration ratio (R_c) and mass ratio (R_w) at different concentration factors CF (22 bar).

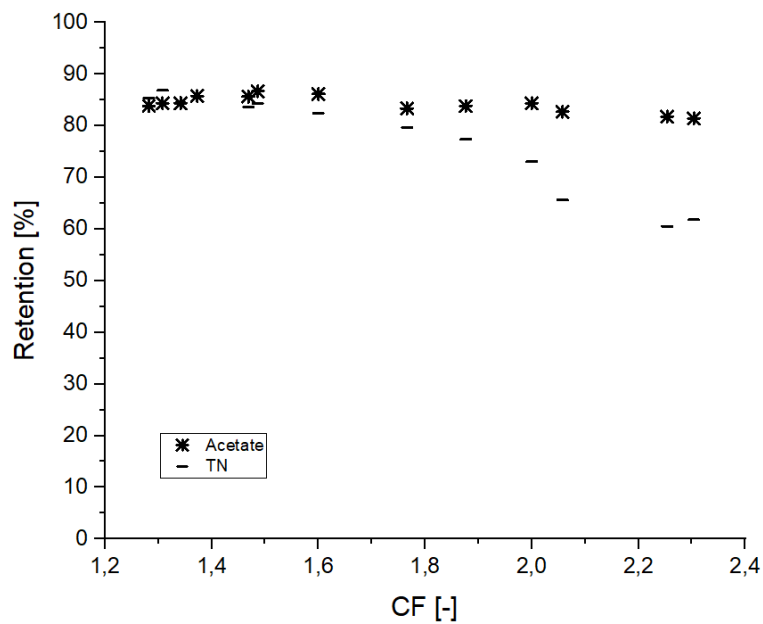


Fig. 3-4: Retention of acetic acid and ammonium (measured as TN) at different CF (22 bar).

The concentration of acetic acid in the permeate increases with CF. This was a consequence of the higher concentration in the feed, which led to a higher osmotic pressure (Fig. 3-2). A higher concentration in the feed resulted in a higher flux of solute through the membrane. A higher osmotic pressure indicated at the same time a decline of the effective pressure, i.e., the driving force for water flux through the membrane. Thus, the concentration of acetic acid in the permeate turned out to be greater, and the permeability decreased with the concentration factor, since the effective applied pressure decreased.

A positive contribution to the parameter R_c (Fig. 3-3) was given by the increase in the acetate concentration in the concentrate when the concentration factor ranged from 1.3 to 1.5 (Fig. 3-2). When the concentration factor was greater than 1.5, R_c showed a decrease. The concentration of acetate in the concentrate at a CF of 2.3 was 30% higher than at a CF of 1.5. In contrast, concentration in the permeate almost doubled in the same range. In other words, the increment in the concentration of acetate (and ions in general) in the concentrate did not compensate anymore for the one in the permeate. This was reflected in the parameter R_c , which had its maximum value at a concentration factor of 1.5, corresponding to a recovery of 33%.

R_w , the ratio between the flowrates of acetate in the concentrate and the permeate, decreased in the whole range of CF tested values. Nevertheless, the decrease slowed down for a concentration factor greater than 2.

The results concerning the retention are consistent with the literature. XLE was already used under similar conditions and at comparable acetate concentrations, retaining 85% of acetate

(Zhu et al. 2020). The retention (Fig. 3-4) is negatively affected by an increase in the concentration factor. This was due to the higher concentration of the solution facing the membrane, with the consequences described above. However, the decline in retention was more pronounced for the total nitrogen (as an indicator of ammonium concentration) than for acetate. This might be due to the positive charge of ammonium, which is more easily pushed through the negatively charged membrane, as the ionic strength in the feed channel increased.

According to previous experiments, fouling/biofouling may occur only after 16 days of operation, under the same conditions of the present study. Consequently, fouling is assumed to play no role for the experiments presented in this work.

Concentration polarization could be expected to play a role in determining the permeate flux and consequently the parameters R_c and R_w . Nevertheless, under the present conditions, no clear influence is expected. The Reynolds number in the channel (570) was much higher than the one associated to a concentration polarization factor (CPF) of 1.1 by Salcedo-Díaz et al. (Salcedo-Díaz et al. 2014). Additionally, Jung et al. showed that at a cross-flow velocity of 0.2 m s^{-1} the CPF can even assume lower values (Jung 2020).

3.3.2 Experiment at 25 bar

A similar experiment to the one presented above was run at 25 bar to evaluate the influence of pressure changes on rejection and membrane performance. The system behaved similar as at 22 bar. This time, the overall duration of the experiment was 10 days, with a sampling interval of one day. The average volumetric flowrate of the feed varied from 9 mL min^{-1} (at a CF of 2.1) to 55 mL min^{-1} (at a CF of 1.3). In the same range, the sum of the two permeate flowrates varied from 4.7 to 11 mL min^{-1} and the flowrate of the concentrate from 4.3 to 44 mL min^{-1} . At higher pressure, the retention of acetate is slightly higher and remains practically constant (88%) throughout the range of CF (Fig. 3-5). A lower retention (75%) was obtained by Bóna et al. with LPRO membrane at the same pH, although at lower pressure of 6 bar (Bóna et al. 2020). Choi et al. also observed lower acetic retentions at pH 5.5; however, looser NF membranes were used in their study (Choi et al. 2018).

Retention of total nitrogen decreases dramatically (from 85% to 60%), similarly as at 22 bar. Likewise, this can be explained by the Donnan effect. The increase in the ionic strength in the feed channel negatively affects the retention of chloride. Consequently, ammonium must flow to the permeate side to maintain charge equilibrium. At the maximum recovery observed, the concentration of acetic acid in the permeate was 4 g L^{-1} at 25 bar and 6 g L^{-1} at 22 bar (Fig. 3-6), resulting in a larger R_c . The concentration of acetate in the concentrate was comparable between both experiments, around 32 g L^{-1} . Due to the better rejection, the maximum of R_c shifts to the right and reached a higher value (Fig. 3-7). For values of CF higher than 1.8 (recovery of 44%), R_c started decreasing again, and the concentration of acetate in the concentrate did not increase proportionally to the one in the permeate (Fig. 3-5). Hence, a

higher applied pressure meant a higher optimal recovery. It must be therefore pointed out that the optimal recovery does not only depend on the characteristics of the solution but also on the operation conditions and the rejection properties of different membranes that change the boundaries of the process.

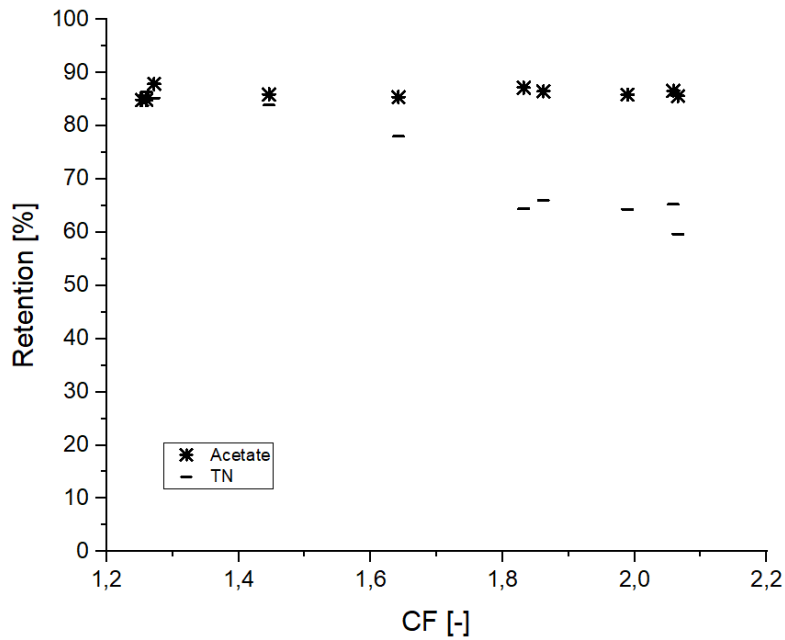


Fig. 3-5: Retention of acetic acid and ammonium (measured as TN) at different concentration factors CF (25 bar).

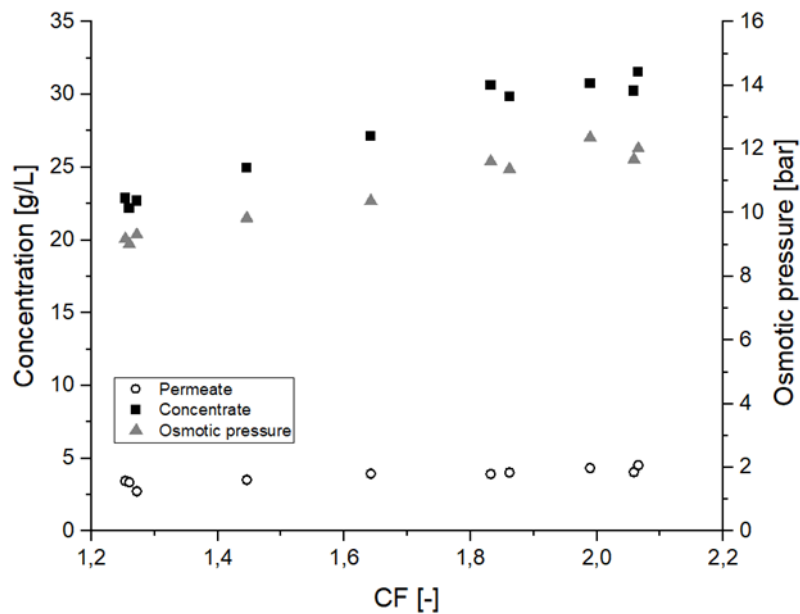


Fig. 3-6: Osmotic pressure and acetate concentrations in the concentrate and in the permeate at different concentration factors CF (25 bar).

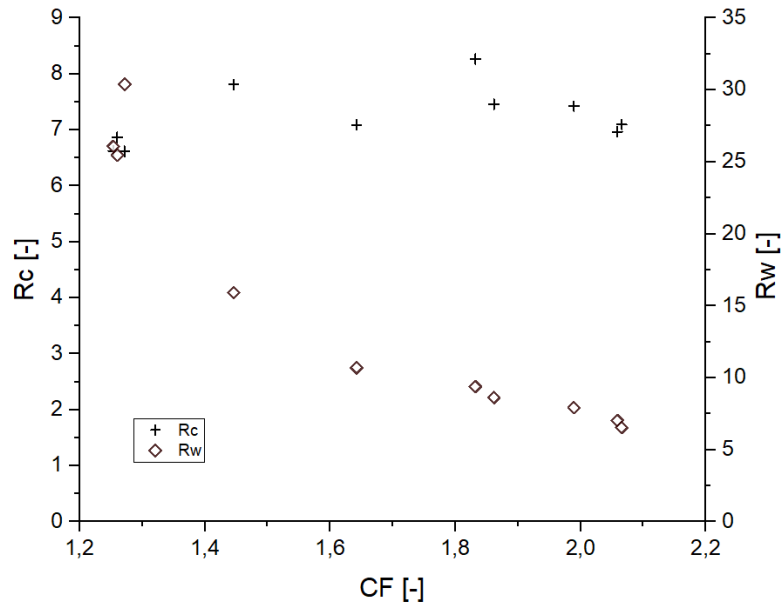


Fig. 3-7: Concentration ratio (R_c) and mass ratio (R_w) at different concentration factors CF (25 bar).

3.3.3 Economic considerations

In order to qualitatively assess whether an increase of 3 bar of the operating pressure may have a beneficial effect on the overall economics of the process, R_c must be considered together with the recovery. At different pressures, the maximum R_c (R_c^{max}) was found at different recoveries. This means that the pressure giving the highest R_c^{max} is not necessarily the best option. For 22 bar, the optimal recovery was 33% ($R_c^{max} = 7.5$), and for 25 bar, it was 44% ($R_c^{max} = 8.3$). That is, the separation efficiency was higher in the second case, but at a higher recovery, more permeate is produced. The parameter R_w can better clarify this aspect. R_w is about 15 and at 22 bar and 10 at 25 bar, meaning that at 25 bar 50% more acetate is lost in the permeate than at 22 bar. In other words, at 25 bar, a better separation efficiency can be achieved, but this fact is compensated by the high amount of produced permeate, causing a considerable loss of solute.

Besides, the difference between the two pressures (3 bar) is more than 10% of the total applied pressure. Thus, it is conceivable to expect that the energy consumption differs by the same order of magnitude. In conclusion, with an operational cost roughly one tenth higher and a loss of solute in the permeate 50% greater, the operation at 25 bar appears to be less advantageous.

3.4 Conclusions

Acetic acid was concentrated using a low-pressure reverse-osmosis membrane. The separation efficiency was assessed at different recoveries by varying the concentration factor

CF. The results showed that above a certain value of recovery (33% at 22 bar and 44% at 25 bar), the efficiency of the separation (represented by R_c) started to decrease. As the recovery increased, the solution in the feed channel was more concentrated. As a consequence of the higher concentration gradient along the membrane, a considerable amount of solute was lost in the permeate, and the total reclamation of acetic acid decreased. Therefore, it can be concluded that recovery should only be increased up to a certain extent, even despite other effects such as fouling and concentration polarization.

Concerning the operating pressure, a preliminary economic consideration showed that the higher costs needed to provide a higher pressure are not justified by a better overall performance. A higher pressure can indeed result in a better separation efficiency. On the other hand, with a higher permeate flux, a greater amount of solute can be lost.

4 Differentiating fouling on the membrane and on the spacer in low-pressure reverse-osmosis under high organic load using optical coherence tomography

(Published in ELSEVIER Separation and purification technology)

The optimization of the recovery addressed the first issue in the application of RO in the two-stage production of biogas: the VFA yield. However, VFA are an easily degradable carbon source for microorganisms. Under such high VFA concentrations as the one reported in the previous chapter (up to 30 g L⁻¹), there is no substrate limitation for microbial growth. This implies a particularly high biofouling potential. In contrast to the recovery, biofouling issues do not significantly affect the yield of VFA. The occurrence of fouling rather threatens the long-term operability of the membrane, by reducing its lifetime and increasing the operational costs related to cleaning. Therefore, the natural follow-up of the work is the focus on biofouling. In this chapter and in the following one, the focus is shifted to the monitoring of biofouling and its characterization. The goal is to better understand biofouling occurrence and provide hints about how this problem should be tackled. In chapter 4, biofilm observation in FMM has been carried out with OCT, an established imaging method used in other previous studies on related topics (e.g. West et al. 2016, Fortunato et al. 2020). Thereby, the results of the present work could be compared with the findings already reported in literature.

4.1 Introduction

In membrane separation processes both biofouling and organic fouling can lead to a severe permeability decline and even more affect the permeate quality. Therefore, the separation of low molecular weight organic compounds from solutions (hydrolysates) with a high fouling potential by the use of reverse-osmosis (RO) is challenging (Jänisch et al. 2019; Bóna et al. 2020). RO membranes are composite membranes, consisting of a thin polyamide active layer deposited on a supporting porous layer. The polyamide layer has a dense structure through which the solvent diffuses. It is generally assumed that dense membranes do not have pores. Herein, the dominant fouling mechanism for RO membranes is the formation of a fouling layer in the feed channel. The characteristics of this deposit (e.g. its porosity and thickness), which are influenced by the membrane properties and the composition of the treated solution, control the flux decline together with the operating conditions (Tariq Khana et al. 2014).

In spiral wound modules the bio/organic fouling load (mass of dried foulant material per unit surface area) is higher for the lead position module (Tariq Khana et al. 2014). This effect is more pronounced when the concentration of organics in the feed is higher. However, in the last module, inorganic fouling/scaling is predominant mainly due to the higher concentration of salts toward the end of the feed channel.

Two key parameters for (bio)fouling control are flux and crossflow velocity (Suwarno et al. 2014). High fluxes induce convective transport of bacteria and nutrient toward the membrane surface, favoring biofouling and thereby negatively affecting the channel pressure drop. However, crossflow velocity acts differently on the transmembrane pressure (TMP) and the channel pressure drop. TMP decreases with increasing crossflow velocity, while channel pressure drop is proportional to the square of the crossflow velocity. A higher cross flow velocity decreases concentration polarization of solutes, thereby slowing down biofouling formation, which has a beneficial effect on TMP. Low crossflow velocities promote attachment and biological growth due to low shear forces. Shear stress also affects the biofilm structure, which can be fluffier or more compact if the fluid velocity in the channel is lower or higher, respectively (Suwarno et al. 2014). Studies have investigated the interconnection between spacer geometries, shear stresses and biomass accumulation using different types of feed spacers (from column type to helical filaments spacers) (Ali et al. 2019; Kerdi et al. 2018, 2020, 2021).

The smaller the clearance height (space between the spacer filament and the membrane surface), the higher the shear stress on the membrane, which in turns results into a faster attachment of biofouling. However, as filtration time progresses the fast growth of bacteria is enhanced in the central region of the rhombus, characterized by lower shear stresses and a stable hydrodynamic (Kerdi et al. 2018). Also, regions where the flow field is more stable also showed less detachment of biomass and more favorable conditions for growth (Kerdi et al. 2018).

Several techniques have been used for the imaging of the fouling layer in feed channels: nuclear magnetic resonance (NMR), oxygen imaging with planar optodes, electrical impedance spectroscopy (EIS), and optical coherence tomography (OCT) (Farhat et al. 2016; Li et al. 2016; West et al. 2016; Bauer et al. 2019, 2021; Fortunato et al. 2017; Hube et al. 2021; Wang et al. 2017). Among them, OCT has proved to be a valuable technique to assess the distribution of biofilm and its structure at the mesoscale (from 100 μm up to 5 mm) (Valladares et al. 2016; Wagner et al. 2010). This is due to the nondestructive nature of OCT and the fast image acquisition, that allow for in-situ real time characterization of the fouling layer. So far, several studies have been carried out to describe fouling of membrane systems and its negative effects on the process efficiency using OCT. Once the OCT dataset is acquired, a major challenge is represented by image processing. Algorithms for image processing can be implemented using either already available plug-ins or custom-made scripts allowing for a more specific interpretation of the data.

In their study about biofouling in RO, West et al. investigated the biofilm development by means of OCT and the subsequent pressure drop along an RO flat sheet module under different organic loads of the feed and with different spacer geometries (West et al. 2016). One of their main findings was that a small-meshed spacer promotes a faster biomass growth in comparison with a wide-meshed spacer. Nevertheless, the final pressure drops and biomass

volumes associated to the different spacer geometries are comparable. A remarkable role on biofouling was played by the feed composition. Their study does not deliver any information about the distribution and the morphology of biomass, nor about surface coverage. To more deeply understand fouling mechanisms, spatially resolved biofilm quantification is needed. There are already some studies dealing with this aspect.

Bauer et al. investigated scaling in membrane distillation using OCT (Bauer et al. 2019). They analyzed the inorganic fouling layer, describing its structure with the help of image processing and demonstrated that it is possible to correlate macroscopic process parameters (i.e. flux and cumulated condensate volume) with local characteristics of the deposit. In a further research they assessed the impact of operating conditions – such as water matrix, temperature and air-gap/direct-contact configurations – on several scale parameters, concluding that the process can be optimized thanks to an accurate observation of the scale layer at a microscopic level (Bauer et al. 2021).

Fortunato et al. performed OCT imaging during a 5 days experiment, in which they operated an ultrafiltration membrane fouling simulator, using tap water as feed (Fortunato et al. 2017). Additionally, a nutrient solution was continuously dosed to trigger biomass formation. They quantified the biomass volume on the membrane, feed spacer and cover glass, finding that during the first 2 days the biomass accumulation in the module was low. Starting from the third day, biofilm attachment on the spacer was observed, accompanied by an increase of the pressure drop. The highest spreading of biofilm on the membrane occurred on the last two days of the experiment. The duration of the experiment was relatively short, due to fast biomass growth. A similar approach has not yet been applied to long term trials. Longer times of observation enable higher temporal resolution, therefore yielding more information about phenomena that might be overlooked when biomass growth occurs too fast.

The present study focuses on the development of a method for (bio) fouling quantification in spacer filled channels, with a view to reproducing fouling behavior in spiral wound modules. In contrast to previous works, the flat sheet membrane module (FSMM) were operated with feed streams at high organic load. A synthetic solution simulating an anaerobic hydrolysate was fed to the units. The quantification of fouling was realized via OCT. The goal was to differentiate between the biofilm growing on the spacer filaments and the one growing directly on the membrane surface using microscopic parameters and to relate biofilm growth to macroscopic process variables. The pressure drop along the modules was measured as well as membrane permeability. An attempt has been made to understand whether the biofilm growing on the spacer or the one growing on the membrane (or both) dominates the flux decline at different stages of operation.

4.2 Materials and methods

4.2.1 Feed solution

Experiments were carried out using a model solution. The composition of the solution was formulated to simulate the hydrolysis product of pig manure and sugar beet at 55 °C and 1 bar. Tab. 4-1 displays the composition of the feed, which was mainly composed by acetate. The pH was 5.4 ± 0.1 , the electrical conductivity was $17 \pm 0.5 \text{ mS cm}^{-1}$ and the turbidity was 2.7 NTU. Hydrolysates with similar composition were produced by Kumanowska et al. and Ravi et al. (Kumanowska et al. 2017; Ravi et al. 2018).

Tab. 4-1: Feed composition.

| Component | g L ⁻¹ |
|----------------------------------|-------------------|
| CH ₃ COO ⁻ | 16.9 |
| Na ⁺ | 2.8 |
| K ⁺ | 2.4 |
| Ca ²⁺ | 1.4 |
| Cl ⁻ | 0.4 |
| NH ₄ ⁺ | 0.2 |

4.2.2 Lab-scale LPRO setup

The experiment was performed on a LPRO system, equipped with two FMM arranged in parallel, in order to run the experiment in duplicate. Each module was provided with three optical windows (sapphire glass, 1" diameter, 5 mm thickness, Thorlabs, Bergkirchen, Germany) facing the feed channel, allowing for the visualization of the fouling layer. To each window corresponded an imaging position (at 70 mm, 140 mm, and 210 mm from the inlet of the channel). XLE membrane sheets (FilmTec Dupont, Wilmington, DE, USA) were placed inside the modules. This membrane is a low energy polyamide thin-film composite membrane used for RO. A commercially available RO 28 mil woven spacer with a mesh of 3.5 mm was set in the feed channel. Due to the typical structure of the woven spacer, clearance height is not constant and for the 28 mil spacer amounts to 230–490 μm. A photograph of one module is displayed in Fig. 4-1a. The active surface of the sheet was $0.279 \times 0.1 \text{ m}^2$ and the channel height was 0.7 mm.

Temperature was recorded by a sensor (2xPt100, Negele Messtechnik GmbH, Egg an der Günz, Germany) placed before the modules and kept constant by means of a thermostat. Pressure indicators (Cerabar PMP11, Endress + Hauser GmbH, Maulburg, Germany) were placed before and after the modules. The volumetric flow rates in the two parallel tracks on the retentate side was monitored by two magnetic inductive flowmeters (Picomag, Endress + Hauser GmbH, Maulburg, Germany). A diaphragm pump (G03, Verder, Haan, Germany) supplied both tracks with the feed. A simplified flow diagram of the setup can be seen in Fig. 4-1b. Permeate and concentrate were recirculated to the 5 L tank. The feed was renewed every day to limit bacterial growth inside the vessel.

4 Differentiating fouling on the membrane and on the spacer in low-pressure reverse-osmosis under high organic load using optical coherence tomography

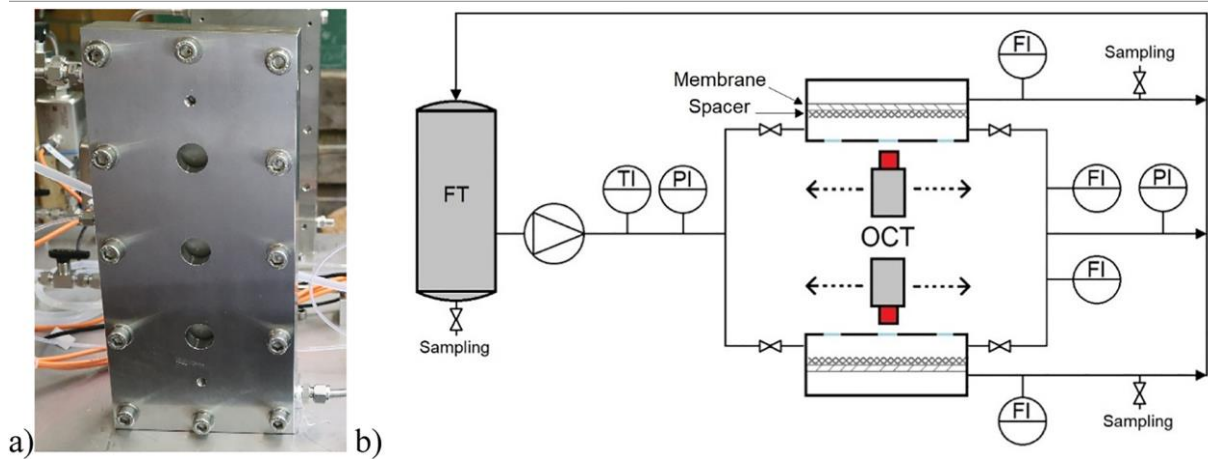


Fig. 4-1: Photograph of an FMM with optical windows (a) and schematic representation of the lab-scale LPRO setup (b). FT: feed tank; TI: temperature sensor; PI: pressure sensor; FI: flowmeter.

4.2.3 Operational conditions

For 26 days the pressure before the modules was kept at $25 \text{ bar} \pm 0.5 \text{ bar}$ while the temperature was $37 \pm 1 \text{ }^\circ\text{C}$. Experimental conditions were based on a previous work dealing with concentration of acetic acid (Pratofiorito et al. 2021). The average crossflow velocity inside the feed channel was 0.2 m s^{-1} (Reynolds number, $Re = 570$), a typical value for spiral wound modules. Before starting the experiment, the system was run with deionized water at 10 bar for 3 h to for membrane pre-conditioning.

4.2.4 OCT and image processing

A GANYMEDE II spectral domain system (Thorlabs GmbH, Dachau, Germany) was used to perform OCT imaging. The OCT device was provided with an LSM04 objective lens (Thorlabs GmbH, Dachau, Germany). The A-scan acquisition rate was 36 kHz. The field of view (FOV) was set at $6 \text{ mm} \times 5 \text{ mm} \times 1.6 \text{ mm}$, in order to picture one rhombus of the spacer and the halves of the surrounding rhombuses. The axial resolution was $3.14 \text{ } \mu\text{m voxel}^{-1}$, whilst the resolution in the x-y plane was $8 \text{ } \mu\text{m voxel}^{-1}$. The refractive index was fixed at $n = 1.33$.

OCT C-scans consisted of a 3D image in which both the spacer and the membrane surface were represented. To separately analyze the information about the spacer and the membrane, an in-house ImageJ macro was written and run on Fiji (ImageJ version 2.1.0). The results of the image analysis on the three positions of the two parallel units were then averaged. Hereunder the processing steps for the membrane as well as for the spacer section of the picture are clarified.

4.2.4.1 Image analysis of the membrane

The macro was tailored to every imaging position, since the spacer was placed differently inside the FOV depending on the acquisition spot. However, the spacer maintained the same location during the experiment, so that by every acquisition on the same spot at different times the topography of uncovered spacer and membrane was the same.

The raw C-scans were converted from 32-bit to 8-bit. To evaluate only the fouling formation on the membrane, a rhombus – corresponding to the region of the membrane that was not covered by the spacer – was cropped out of the raw image dataset (step A). The contour of the rhombus was defined by placing its vertexes 50 μm away from the corners of the spacer. In this way, the possible interference caused by the fouling formation on the spacer was excluded and only the portion of membrane uncovered by the spacer was analyzed.

A filter was applied and the contrast was enhanced (Step B). The image dataset was then flattened as described by Bauer et al. (Step C) (Bauer et al. 2019). This was necessary to align the bottom of the fouling layer on the same height inside the image, since the membrane was not perfectly flat. Thereafter, the contrast was enhanced and the image was binarized according to Yen et al. (Step D) (Pfaff et al. 2021). The membrane area below the feed spacer was not considered in the calculation of ME. The spacer was indeed transparent and biofilm below the filaments could be seen, but the change of the refractive index at the spacer-liquid interface implied a shadowing effect with a subsequent distortion of the image. This can be clearly seen in the images provided in the supporting material. The membrane below the spacer appears to be displaced downwards. Image analysis in this region is likely to overestimate dimensions of objects. 2D images are provided in the appendix 4-1 to show biological growth.

Fig. 4-2 depicts each step. It must be mentioned that the setting for the cropping and the processing of each spot were the same for the whole time series, allowing for a consistent treatment of the collected data.

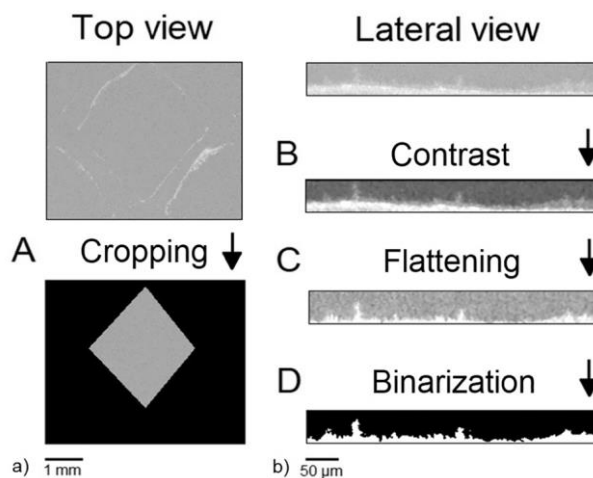


Fig. 4-2: Image processing steps for the membrane. Top view of a spacer rhombus (a) lateral view of the fouling layer on the membrane (b).

4.2.4.2 Image analysis of the spacer region

The spacer filaments do not have a constant section and present an irregular geometry. This makes the evaluation of 3D datasets more difficult than on the membrane, since the irregular geometry does not permit to write a macro that crops the image close enough to the spacer everywhere. For this reason, it was decided to analyze several B-scans (i. e. slices of the 3D stack) separately and to average the results to gain information about biofilm development on the spacer. Similarly, to the image processing of the membrane, the dataset had to be filtered, the contrast enhanced and the image binarized. Fig. 4-3 depicts the process of one B-scan yielding a binarized image of the cross-section of a spacer filament.

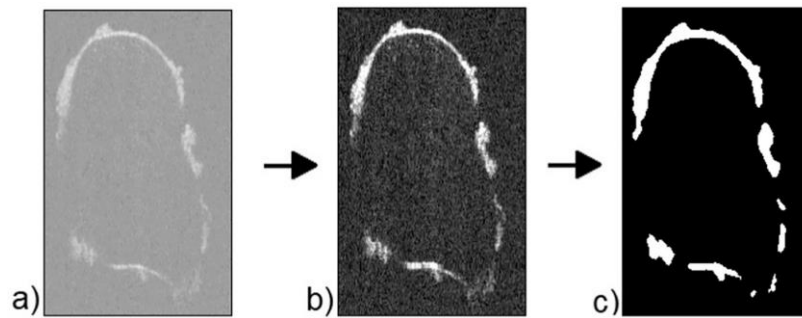


Fig. 4-3: Processing steps of a B-scan. The raw image dataset (a) is first filtered and the contrast is enhanced (b) and then the dataset is binarized (c).

4.2.4.3 Development of parameters

To separately quantify the biofilm growing on the membrane (Fig. 4-1) and the one growing on the spacer (Fig. 4-2) the following parameters have been defined:

$$ME = \frac{V_{ME}}{S_{ME}} \quad \text{Eq. 4-1}$$

$$SP = \frac{A_{SP}}{L_{SP}} \quad \text{Eq. 4-2}$$

ME (μm) represents the average thickness of biofilm growing on the membrane. This applies under the assumption that biofilm growth on the membrane is quite homogeneous. V_{ME} (μm^3) is the biovolume accumulated on the membrane and S_{ME} (μm^2) the membrane area without spacer (area enclosed by the rhombus cropped from the image, (Fig. 4-2)). V_{ME} is calculated by multiplying the white voxels of the processed C-scan times their size.

SP (μm) approximates the average thickness of the biofilm layer covering the spacer. A_{SP} (μm^2) is the area obtained multiplying the number of white pixels in the processed B-scan of the spacer (Fig. 4-3c) times their size and represents the amount of fouling deposit on the

spacer. L_{SP} (μm) is the width of the spacer filament and is used to normalize A_{SP} , yielding a monodimensional parameter. L_{SP} was calculated on the clean spacer with the built-in function “Straight” of Fiji for each B-scan, as the spacer did not have a constant cross-section, due to the irregular geometry. Precisely this irregular geometry did not make it possible, to implement the calculation of the spacer perimeter in the macro. The L_{SP} values along the Y-direction are provided in appendix 4-2.

To exclude the initial pressure drop provoked by the FMM itself and the tubing, the relative pressure drop was calculated (Eq. 4-3):

$$\Delta p = p - p^0 \quad \text{Eq. 4-3}$$

where p is the pressure drop at a given time and p^0 is the initial pressure drop of 0.1 bar. Such a high initial value can be explained by the fact that the tube between the first pressure transducer and the FMM made a curve (Fig. 4-1b). This was the case also for the section between the FMM and the second transducer. Besides, the downstream sensor was placed after the valve for the setting of the flow velocity, resulting in an additional pressure drop.

4.3 Results and discussion

The FMM were run for a period of 26 days and three different positions were pictured daily by means of OCT on the modules. The focus of the work was to distinguish between (bio)fouling formation both on spacer and membrane surface. However, the separation performance of the membranes did not seem to be affected by biofouling. The retention of acetic acid fluctuated between 87% and 92% (Pratofiorito et al. 2021).

4.3.1 Biofilm development

The evolution of the two parameters is shown in Fig. 4-4. During the first 15 days the fouling formation on the membrane was very low and ME stayed below the OCT detection limit. Fouling started being more appreciable from the sixteenth day, showing an exponential increase. On the other hand, the build-up on the spacer was already evident from the beginning. Its rise was more linear than the one on the membrane and the average SP reached a maximum of 31 μm between day 16 and day 17. This value was maintained until the experiment was shut down. However, detachment and new attachment did also occur on the spacer during the final days. Some images are provided in the appendix 4-1 material to show the biofilm growth over time.

4 Differentiating fouling on the membrane and on the spacer in low-pressure reverse-osmosis under high organic load using optical coherence tomography

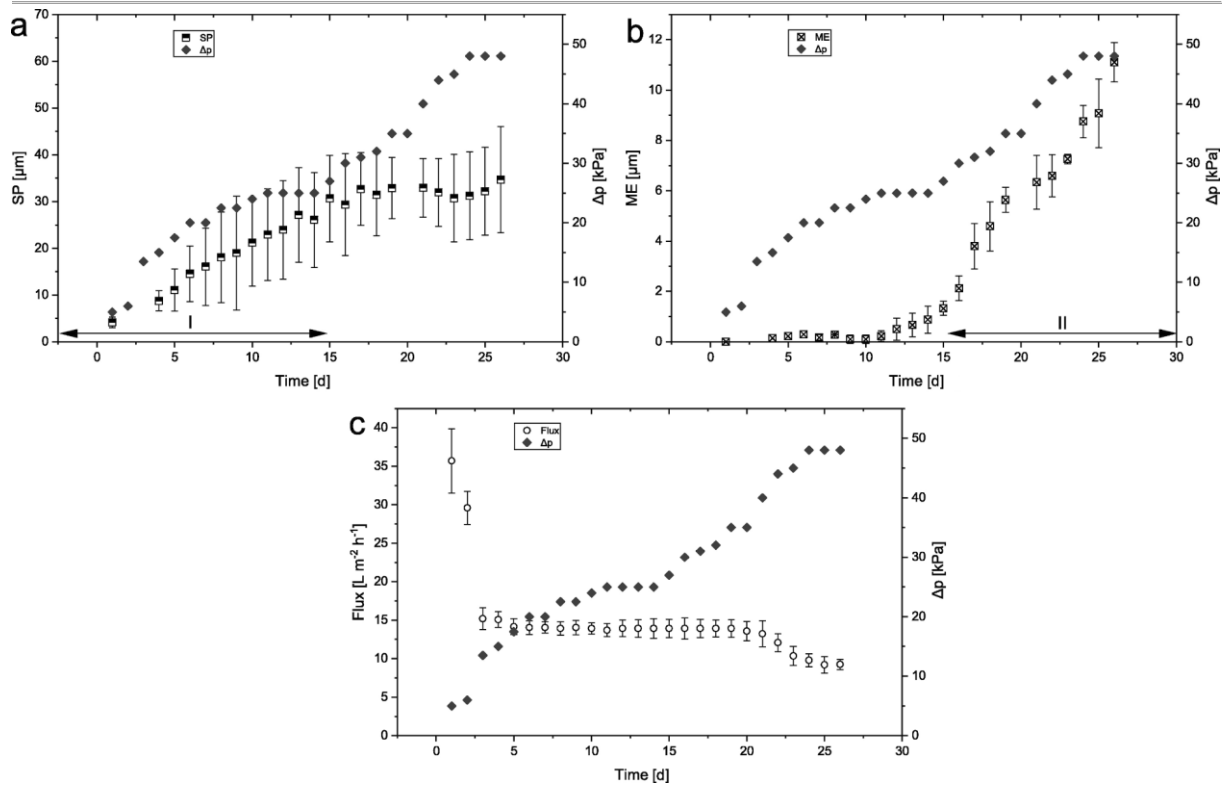


Fig. 4-4: Development of relative pressure drop together with spacer fouling (SP) (a), membrane fouling (ME) (b), and flux (c). The arrows show the phases in which pressure drop is governed by fouling on the spacer (I) and on the membrane (II).

Fouling layer thickness strongly depends from nutrient concentration/ water composition, shear stresses, and pressure. Despite the very high availability of carbon source and a cross flow velocity typical for spiral wound modules, the fouling layer was very thin due to high pressure. The final average height of the fouling layer on the membrane was about 11 μm . Fortunato et al. obtained an averaged thickness of fouling on an UF set-up of about 55 μm (Fortunato et al. 2020). This value is five times higher than the one obtained in this study. Differences on the thickness of the fouling layer might be due to a) the presence of suspended solids in their feed (however smaller than 5 μm), leading to the formation of a cake and b) the pressure used in their study (1 bar), 25 times lower than the one used here, justifying the formation of a thicker layer. The higher pressure used in our study lead to the formation of a more compact layer. This layer can account for up to 80% of the filtration resistance (Bauer et al. 2019) The specific biomass resistance was calculated as described elsewhere (Fortunato et al. 2018) and amounted 3.3 $\mu\text{m}\cdot\text{m}^{-1}$. Another factor that might have increased the compactness of the fouling layer is the high concentration of Ca^{2+} ions in the feed (35 mM). Pfaff et al. investigated the influence of calcium concentration in the supernatant (ranging from 1 mM to 15 mM) on the compactness of their biofilm (Pfaff et al. 2021). They could correlate an increase of the concentration to a compacter structure of the layer, with a plateau at 8 mM. This fact has been explained with the higher crosslinking between negatively charged

portions of extracellular polymeric substances (EPS). Both algal and bacterial biofilms showed this behavior. The resulting compactness explains the high hydraulic resistance experienced in our study. Another study showed that already a concentration of 0.5 mM of Ca^{2+} can promote the adsorption efficiency of EPS on a RO membrane, which lead to a lower flux (Herzberg et al. 2009).

Suwarno et al. performed a RO membrane autopsy followed by image acquisition via confocal laser scanning microscopy (CLSM). The biovolume of the material occluding the module was calculated using a commercially available software (IMARIS, Bitplane, Switzerland) and resulted to be higher than the one obtained herein (26.3 μm) (Suwarno et al. 2014). This can be on one hand because they operated their RO system at a pressure between 10 and 11 bar. On the other hand, the invasive nature of CLSM might have affected the accuracy of measurement. In fact, imaging was performed ex-situ and after staining. Removing the membrane from its place always implies the risk of modifying the structure of the biofilm and the release of pressure from 10 bar to ambient pressure might also have expanded it. This stresses the advantage of OCT as a noninvasive technique.

Although *SP* is scaled by the width of the spacer rather than its perimeter, it is reasonable to compare it with *ME*. Of course, it must not be a one-to-one comparison, since *SP* will be higher than *ME*, even when the amount of biomass per surface area is the same on the spacer and on

the membrane. However, in this study *SP* appears to be two to three times higher than *ME*. Picioreanu et al. developed a three-dimensional computational approach to describe biomass attachment in feed channels (Picioreanu et al. 2009). One of their findings was that shear stress is higher on the membrane than on the spacer filaments because of the acceleration imparted to the fluid in the narrow section between the filament and the membrane surface. This might explain the difference between *ME* and *SP*. The values of *SP* are close to the “specific biovolume” obtained by Fortunato et al. with OCT (Fortunato et al. 2020). Differences between the results of this and their study can be due to the different algorithm used for image analysis (filter, thresholding, etc.), different resolution of the image acquisition as well as to the specific operating conditions. On the other hand, the degree of biofouling on the spacer filaments obtained by Suwarno et al. is significantly lower (around 7 μm), probably due to the lower nutrient concentration of their feed solution (6.5 mg L^{-1} total organic carbon, TOC) and the shorter duration of the experiment (10 days) (Tariq Khana et al. 2014).

As for the distribution of biomass on the membrane over the module length, in this work, no difference between the inlet and the distal positions could be detected. Apparently, the limited length of the module did not allow for diversification of the fouling layer. However, against expectations, the spacer of the terminal position had approximately 50% more biofilm compared to the lead and the central positions. It can be suggested that fragments of detached biomass were dragged by the current and accumulated on the spacer in the end

section of the membrane module. This discrepancy is the cause of the big standard deviation reported in the graph (Fig. 4-4a).

4.3.2 Flux decline and feed channel pressure drop increase

The flux was continuously monitored over the duration of the experiment and the inlet pressure was kept constant. By measuring the outlet pressure, it was possible to determine the pressure drop along the module. Fig. 4-4c depicts the trends of the flux (average of the two parallel units) and the pressure drop. During the first two days of operation, flux decreased sharply, due to membrane compaction and the conditioning of the membrane by the feed. Preliminary experiments showed similar times for membrane compaction. Afterwards, it set to a stable value of $14 \text{ L m}^{-2} \text{ h}^{-1}$, which stayed stable until day 21. The experiment was concluded when flux decreased below 70% of the stable value.

The relative pressure drop in the feed channel increased almost constantly, indicating that the fouling on the spacer represents the main resistance to the flow in the channel. This is in accordance with previous simulations (Pfaff et al. 2021). However, after day 15, Δp built up more rapidly, suggesting that also the fouling accumulating on the membrane played a role in the pressure drop. Looking at Fig. 4-4a and 4-4b, one notices that the pressure drop is governed by fouling on the spacer at first (phase I). However, from day 15 (phase II) the material accumulating on the membrane also contributes to the pressure drop. Given the low average height reached by the fouling layer on the membrane compared to the feed channel height (approx. 1%), it is unlikely that this fraction of fouling caused a substantial reduction of the cross section. It is more reasonable to think that, if it contributed at all to the pressure drop increase, this was rather due to the clogging of the narrow spaces between the filaments and the membrane. We conclude therefore that the impediment of flow would then be localized in these regions and the distributed effect of fouling on “free membrane” (far from the spacer) would be neglectable. This conclusion is supported by the findings of Picioreanu et al. (Picioreanu et al. 2009).

The total Δp divided by the time span (Δt) in which it is built up gives the rate of pressure drop increase ($\Delta p \Delta t^{-1}$). The rate observed in this study (1.8 kPa day^{-1}) was higher than the one reported by Suwarno et al. (Suwarno et al. 2014). Spacer fouling is the main responsible for channel pressure drop. As discussed in section 3.1, in this study the fouling of the spacer was higher than the one found by Suwarno et al., suggesting that the different feed composition triggered a more severe pressure drop.

The maximum pressure drop normalized by the module length can also be used to compare results from different studies. The one obtained in this work (845 mbar m^{-1}) is close to what have already been reported elsewhere (Fortunato et al. 2020). This might be explained by the similarity of the two used systems.

Interestingly, the pressure drop within the feed channel did not seem to affect flux. The inlet pressure was so high (2500 kPa) that the flux did not substantially suffer from the pressure drop increase, even considering the highest value of 50 kPa, accounting for only 2% of the inlet pressure. Reasonably, a longer module would have shown a higher deterioration of permeability owed to pressure drop. A typical spiral wound module is 1 m long, which would correspond to a pressure drop of 90 kPa. This holds under the assumption that the energy losses experienced herein can be directly upscaled solely according to the length and will not be exacerbated by the wider channel of a spiral wound module (typically 2.6 m of channel width) and by the cylindrical geometry.

4.3.3 Surface coverage distribution

The topographic height maps of a representative membrane area are shown in Fig. 4-5. From day 10 fouling starts developing significantly, although only after day 16 a more uniform surface coverage is reached. This is confirmed by Fig. 4-6, revealing a rise in surface coverage around the same date. However, this descriptor is limited to the OCT resolution. This means that the interpretation of the results must take into account the possibility of a thinner foulant layer that could not be detected by the device. The fact that fouling starts accumulating again on the membrane once the attachment on the spacer has stopped is remarkable and suggests that from this point the deposition on the membrane surface is dominant. However, a direct correlation between surface coverage and flux decline could not be found, supposedly because a very thin layer is not sufficient to drastically hinder permeation. Together with the surface coverage, the average fouling thickness must be sufficiently high before the final abrupt permeability drop occurs. This happens short after *SP* has reached its maximum. This appears to be the most convenient moment to start the cleaning, since the permeability drops within the very next days.

By comparing Fig. 4-4b with Fig. 4-6, it can be seen that surface coverage increases even before *ME*. This means that fouling distributes irregularly over the membrane at first, joining together in a thin film later on. Then the film builds up and vertical growth occurs only after a more or less uniform layer has already established. This underlines the importance of comparing different parameters describing biofilm structure (in this case *ME* and surface coverage). We speculate therefore that *ME* can be more easily related to the reduction of permeability than surface coverage, being a more useful key parameter for the prediction of membrane performance.

The possibility that a thin biofilm layer can still allow a high flux has already been proved (Fortunato et al. 2017a). Even with a thickness of 15 μm the permeability can remain essentially unaltered, being almost insensitive to the fouling layer. But again, given the high pressure used in this study, the compactness of the biofilm also plays a role. Accordingly, the height, at which permeability is affected, sinks to 7 μm . On the other hand, for scaling (where the inorganic material shows a higher hydraulic resistance than that of biofoulants) surface

coverage can already be correlated with the deterioration of the membrane performance (Fortunato et al. 2017b).

4.4 Conclusions

A method for biofouling differentiation in feed channels was presented, demonstrating that OCT is a powerful tool to predict both pressure drop in the feed channel and flux decline. The parameters *SP* and *ME* were particularly helpful to represent values for differentiating the biofouling. *ME* is a more relevant indicator for flux decline than surface coverage, confirming that the solution can permeate through the thin biofilm layer (in the order of few μm) without much hindrance. Flux appeared to decline after a certain *ME* value was reached. This happened after three weeks of operation, proving that long term operability under high organic load is possible.

In accordance with previous studies, fouling/biofouling grew on the feed spacer during the first stage of operation. Subsequently, a competition between membrane and spacer fouling appeared, followed by the stabilization of the amount of foulant on the spacer and an increase in the membrane surface coverage. Pressure drop increased during a first phase due to fouling on the spacer, whereas membrane fouling contributed only afterward. Therefore, cleaning cycles should be programmed before attachment on the spacer reaches its maximum (and stabilizes to a plateau), avoiding further deposition directly on the membrane surface. In this study, the maximum *SP* was reached at day 16, four days before drastic flux decline was detected.

5 Application of online biofilm sensors for the prediction of membrane performance in a reverse osmosis with high organic load feed streams

(Submitted – ELSEVIER Separation and Purification Technology)

In chapter 4, a method for the differentiation of spacer and membrane biofouling was presented. An attempt was made to increase the knowledge about biofilm development inside spacer-filled channels and its impact on the membrane performance. An important finding is that stable flux can still be possible even when a considerable amount of biofilm is present in the feed channel of the membrane module. Moreover, the quantification of the biofilm growing on the membrane surface could somewhat predict the permeability decline. This suggests the possibility to gauge biofilm accumulation on the membrane in full scale RO plants, to anticipate the final drop of permeability. Biofilm sensors are a less expensive and less complex alternative to OCT and might accomplish this task. Chapter 5 discusses the cultivation of biofilm on a sensor under similar conditions as in the membrane module. The goal was to investigate whether the sensor can generate a signal before the occurrence of severe fouling. In the context of the two-stage fermentation, the prediction of permeability decline would definitely result in an enhancement of the process efficiency. In fact, a well-timed management of membrane cleaning reduces the overall energy demand for membrane filtration. Some membrane manufacturers recommend to take curative measures against biofouling after the pressure drop along the RO module increases of 10 to 15% from the initial value (Vrouwenvelder et al. 2011). However, pressure drop might increase independently from permeability decline, as already seen in chapter 4. Therefore, it is recommendable to provide the RO installation with an online monitoring tool, delivering additional information to support the decision of when to clean the membrane. A crucial point in chapter 5 is the modification of the sensor surface to facilitate biofilm attachment. This probably represents the most original contribution by the present work to the progress in this field, since no such a modification has been reported in literature for this very specific application so far.

5.1 Introduction

One major concern in pressure driven membrane processes is the loss of permeability due to fouling. Several mechanisms are responsible for fouling, depending on the type of membrane used, the feed water composition, the pre-treatment and the operating conditions (Ibrar et al. 2019). In the case of a solution with high concentration of easily degradable organic compounds, biofouling is the main threat to flux stability. Biofouling is the accumulation of microorganisms in the feed channel with the consequent formation of a biofilm. The biofilm matrix is mostly composed by extracellular polymeric substances (EPS), that are produced by the microbes to better attach to surfaces and to create a favorable microenvironment (Bucs et al. 2018). The occurrence of biofouling is not only reported for sea water desalination or

waste water treatment, but also for the application of reverse osmosis (RO) for the concentration of volatile fatty acids (VFA) coming from a hydrolysis reactor (Pratofioito et al. 2022).

Biofouling control and mitigation is crucial for the reduction of the energy demand. Pretreatment (e.g. biofilters, deep bed filtration, activated carbon and disinfection) is often applied and shows a good reduction of fouling potential – measured as silt density index (SDI), modified fouling index (MFI) or turbidity (Zhao and Yu 2015). However, biofouling cannot be avoided, it can only be delayed (Bucs et al. 2018). Even at a 99.9% removal of microorganisms, the remaining cells are able to feed on the biodegradable organic compounds and to proliferate. Conventionally, chemicals such as acids, bases, enzymes and biocides are flushed into the system to dissolve the biofilm matrix and restore flux. This curative cleaning is applied when the permeability declines below a certain threshold and it might imply the deterioration of the membrane (Huang et al. 2020). Moreover, waiting until a severe decline of permeability often leads to irreversible fouling. Therefore, anticipating permeability decline is essential for an optimal operability of the plant.

Recently, much effort has been dedicated to the prediction of permeability decline using mechanistic models on one hand and data-driven models on the other hand (Ludwig et al. 2012; Lim et al. 2017; Han et al. 2018; Wu et al. 2021). The advantage of both approaches is that they rely on parameters that are easily measurable, such as organic load, flux, air scouring or feed water temperature. One drawback of these predictive models is that they partly display a high degree of specificity. In particular, the complex and dynamic nature of fouling represents another obstacle to the application of mechanistic models. An alternative for these methods is the development of online fouling monitoring tools. Many studies were conducted to deepen the understanding of different types of fouling for several membrane processes (Pratofiorito et al. 2022; Bauer et al. 2019, 2021; Fortunato et al. 2020; Hube et al. 2021; Valladares Linares et al. 2016). Some of the techniques used to quantify fouling so far are: impedance spectroscopy, nuclear magnetic resonance and optical coherence tomography (OCT). They could deliver useful information for fouling characterization, but they are either invasive or difficult to apply at industrial scale and are therefore limited to experiments in laboratories. The use of biofilm sensors is an appealing alternative for a rough estimation of the accumulation of biomass inside a system, without the need of a complex apparatus for the measurement. Several solutions, based on different measuring principles, are available on the market. For instance, the ALVIM sensors measure the cathodic current related with the oxygen consumption of a biofilm growing on a metallic surface (Pavanello et al. 2010). The response of these sensors to biological growth have already been tested in a RO desalination plant to optimize chemical cleaning. However, no visual information about bioaccumulation on the sensor was gathered and no comparison between sensor signal and permeability trends was made. Moreover, these sensors are not applicable to anaerobic systems or systems with low oxygen content, since no cathodic current is generated in absence of oxygen. Another possibility is to measure light adsorption at different wave lengths along the diameter of a tube to gather information about bioaccumulation on its wall (www.environmental-

[expert.com/products/aqua-color-biofilm-sensor-569180](https://www.expert.com/products/aqua-color-biofilm-sensor-569180), accessed on 07.04.2022). In this case, the inconvenient is the presence of substances in the treated solution that might absorb light at the given wave lengths. Furthermore, particles might also scatter light and lead to a false interpretation of the signal. Additionally, the geometry of a tube differs significantly from the one of a spacer-filled channel. Thereby, bioaccumulation inside a pipe would presumably correlate to permeability decline worse than bioaccumulation on a flat surface.

A robust option is offered by heat transfer sensors, which quantify the increase of thermal resistance caused by biofilm deposition on a surface (Reyes-Romero et al. 2014; Netsch et al. 2022). A previous study demonstrated that these sensors are able to detect biofilm growth inside pipes (Netsch et al. 2022). Two different materials for the pipes were tested, stainless-steel (SS) and composite graphite-polypropylene (C-PP). The latter was supposed to be used as electrode material for microbial fuel cells. The SS pipe displayed a higher sensitivity compared to the C-PP pipe, due to the higher thermal conductivity of the C-PP material, which has a negative impact on the accuracy of the measurement. This underlines the importance of the choice of the material.

The present work focuses on biofouling in RO while treating feed streams with high concentrations of volatile fatty acids. It combines direct quantification of biofouling on the RO membrane using OCT and the simultaneous application of a biofilm sensor mounted in parallel to two geometrically identical flat sheet membrane modules (FMM). The sensor was tested without any modification of the measuring surface and then, in a second experiment, the surface was sandblasted and several runs were performed. Additionally, the effect of membrane and sensor cleaning in terms of restoration of permeability, retention and sensor response were evaluated.

5.2 Materials and methods

5.2.1 Flat sheet membrane modules

The FMM were designed to reproduce the flow conditions inside the feed channel of a spiral wound module. The spacer-filled channel of both FMM was 100 mm broad and 279 mm long. XLE membrane coupons (manufactured by FilmTec Dupont, Wilmington, DE, USA) were laid at the bottom of the channel, on top of the permeate spacer. A 28 mil thick feed spacer was inserted into the channel. The linear flow velocity inside the modules was 0.2 m s^{-1} . The two FMM were disposed in parallel, to provide results in duplicate. An optical window allowed for the OCT imaging of the membrane surface at 210 mm from the inlet.

5.2.2 Biofilm sensor

The DEPOSENS[®] biofilm sensors (LAGOTEC GmbH, Magdeburg, Germany) can gauge biofilm deposition by measuring heat transfer across heat-conductive surfaces. As biomass accumulates on the surface, thermal resistance increases, resulting in an increase of the data signal. As biomass accumulates on the plate, thermal resistance augments, resulting in an increase of the signal delivered by the sensor. The working principle of this sensor has already

been described in literature (Netsch et al. 2022). A flow cell made of SS was built to host the sensor, which measured biofilm deposition on the bottom of the flow channel. The sensor was embedded in a housing on the backside of the flow cell and thermally isolated to the outside. On the other side of the flow cell, two optical windows allowed for the visualization of the measuring surface by OCT. The windows were placed at 140 and 210 mm from the inlet of the flow cell. The flow cell channel was as wide and as long as the one of the FMM. The superficial velocity inside the flow cell was set to 0.12 m s^{-1} . This velocity was used by Netsch et al. to detect the biofilm development with a similar sensor. The authors could successfully monitor the growth and development of a biofilm in two tubes of different material (Netsch et al. 2022). A sketch of the flow cell can be seen in Fig. 5-1.

To increase the roughness of the channel surface, normal corundum F020 was used as abrasive agent. The surface roughness was measured before and after sandblasting: $R_a = 0.4 \mu\text{m}$ and $R_z = 2.6 \mu\text{m}$ (before); $R_a = 8.6 \mu\text{m}$ and $R_z = 49.6 \mu\text{m}$ (after) (MarSurf PS 10, Mahr GmbH, Göttingen, Germany).

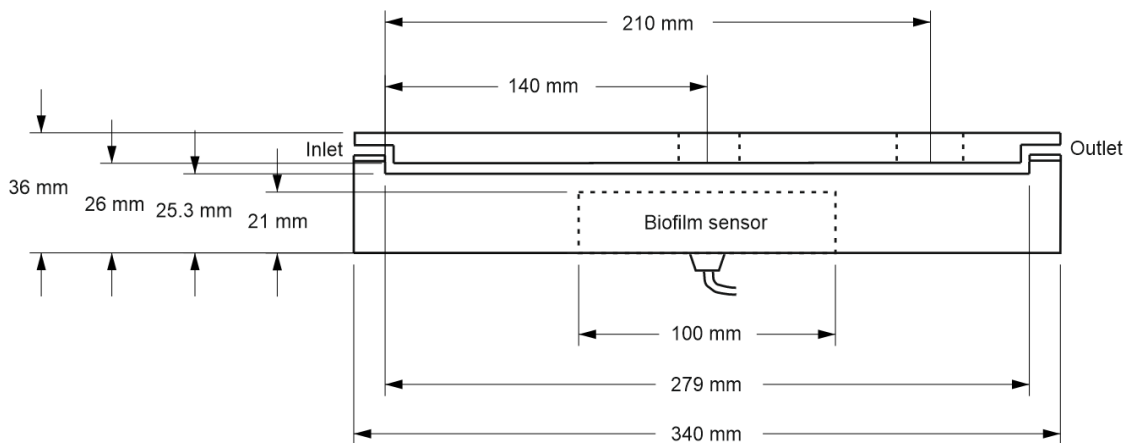


Fig. 5-1 Sketch and dimensions of the flow cell in which the biofilm sensor was embedded, the optical windows for OCT measurement are located at 140 mm and 210 mm from the inlet above the biofilm sensor.

5.2.3 Experimental procedure

The flow cell with the biofilm sensor was installed in an experimental setup equipped with two FMM (Fig. 5-2). The data signal was collected by the Controller unit of the sensor and stored internally on a data logger. The hypothesis was that biofilm growth on the sensor surface and on the membrane are comparable. To validate this assumption and draw solid conclusions, the FMM and the flow cell were provided with optical windows that enabled OCT imaging.

Prior to each experiment, the membranes were cleaned with demineralized water to wash out the preservative glycerin. A diaphragm pump supplied the sensor flow cell and the two modules with the feed solution. The concentrated streams, the permeates and the solution

leaving the sensor flow cell were recirculated to the 5 L feed tank for 24 h. Therefore, fresh medium was poured daily into the tank to replace the old one. About 100 mL of pretreated real hydrolysate (microfiltration with 0.45 μm nominal pore size) were dosed once a day in the system to promote biofouling. The feed consisted of a model solution simulating the product of pig manure and sugar beet hydrolysis with an average chemical oxidation demand (COD) of 30 g L^{-1} . The only carbon source of the synthetic solution was acetate, with a corresponding dissolved organic carbon (DOC) of 6.6 g L^{-1} . The COD was $18.9 \pm 0.5 \text{ g L}^{-1}$ and the total nitrogen (TN) was 200 mg L^{-1} , all in the form of ammonium. The Ca^{2+} , K^+ , Na^+ and Cl^- concentrations were 1.4 g L^{-1} , 2.4 g L^{-1} , 2.8 g L^{-1} and 400 mg L^{-1} , respectively. The turbidity amounted to 2.7 NTU and the pH was 5.4.

The setup was operated under anaerobic conditions (O_2 concentration below the detection limit of 0.1 mg L^{-1}) at 25 bar and 37 $^\circ\text{C}$.

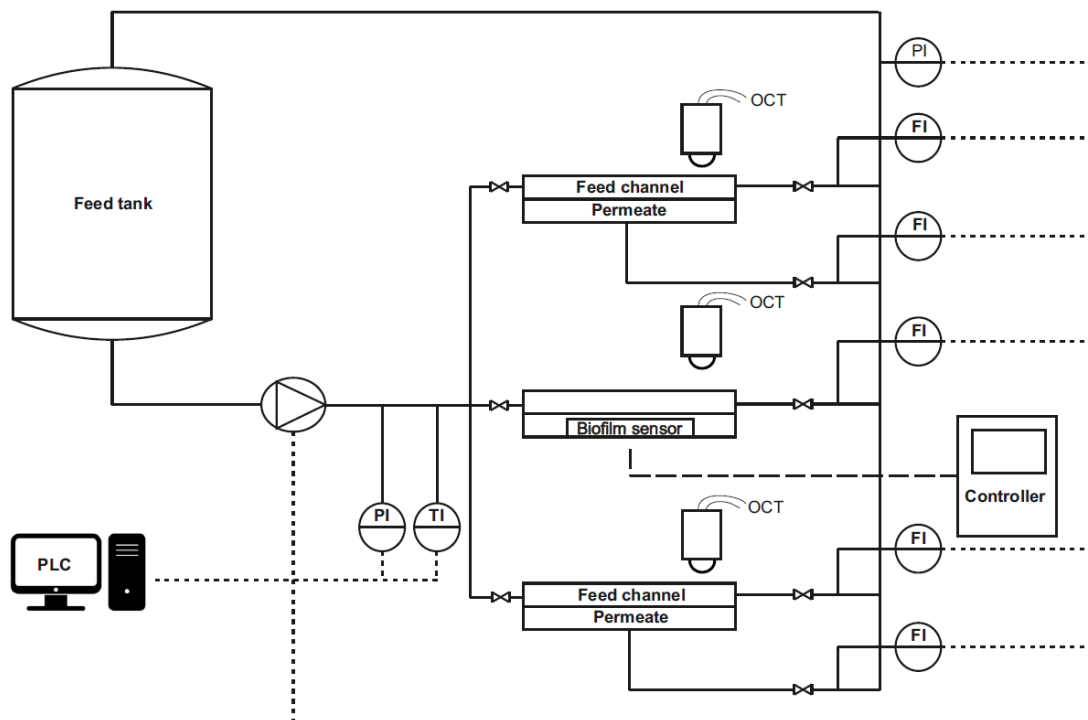


Fig. 5-2 Experimental setup. PI: pressure indicator; TI: temperature indicator; FI: flow indicator. The flow cell with the biofilm sensor was set parallel to the membrane modules.

To evaluate the impact of fouling on the separation efficiency of the membrane, DOC and total nitrogen were measured in the feed and in the permeate streams using a carbon analyzer (TOC-L CPH, Shimadzu Corporation, Kyōto, Japan).

The performed experiments are summarized in Tab. 5-1. For the first two trials (Exp. 1a and 1b), the flow channel of the biofilm sensor was not modified and a feed spacer was applied to promote biofilm formation on the sensor surface (Exp. 1b). For the further experiments (Exp. 2a, 2b, 2c and 3) the bottom surface of the channel, where the sensor took its measurement, was roughened to facilitate biofilm attachment. At last, the membrane and the sensor were cleaned to evaluate flux restoration and to test the response of the sensor (Exp. 3).

Tab. 5-1: Summary of the experiments. The cross-flow velocity inside the FMM, the temperature and the pressure were 0.2 m s^{-1} , $37 \text{ }^\circ\text{C}$ and 25 bar , respectively.

| Experiment | Sandblasted flow cell | Feed spacer above sensor | Biofilm on the sensor | Cleaning with NaOH | Cross-flow velocity on the sensor [m s^{-1}] | Duration [d] | Sensitivity [μm] |
|------------|-----------------------|--------------------------|-----------------------|--------------------|---|--------------|-------------------------------|
| Exp. 1a | No | No | No | No | 0.12 | 11 | - |
| Exp. 1b | No | Yes | No | No | 0.12 | 12 | - |
| Exp. 2a | Yes | No | Yes | No | 0.12 | 14 | 1.2 |
| Exp. 2b | Yes | No | Yes | No | 0.12 | 11 | 1.3 |
| Exp. 2c | Yes | No | Yes | No | 0.02 | 12 | 2.3 |
| Exp. 3 | Yes | No | Yes | Yes | 0.12 | 13 | 1.4 |

5.2.4 OCT imaging

Imaging of the spacer-filled channel and of the measuring surface of the sensor was performed using 5 mm thick sapphire glass windows, with a diameter of 1" (Thorlabs GmbH, Bergkirchen, Germany). The GANYMEDE II spectral domain system was equipped with the objective lens LSM04 (Thorlabs GmbH, Dachau, Germany). The field of view for each picture was $5 \text{ mm} \times 6 \text{ mm}$. The refractive index was set to 1.33. The x-y plane resolution was $8 \mu\text{m voxel}^{-1}$ and the axial resolution was $3.14 \mu\text{m voxel}^{-1}$. Image processing was done with the version 2.1.0 of Fiji (ImageJ). The method used to process the dataset is already presented elsewhere (Pratofiorito et al. 2022). The dataset was first filtered to exclude artefacts. Then, the image was binarized using the intensity value of the biofilm as threshold. The white voxels were counted and multiplied by their volume. The total biofilm volume in the feed channel was then divided by the scanned surface to obtain the biofilm thickness, as described by Eq. 5-1, where V_B is the biofilm volume and S is the scanned surface.

$$\text{Biofilm thickness} = \frac{V_B}{S} \quad \text{Eq. 5-1}$$

5.3 Results and discussion

5.3.1 Biofilm detection with the unmodified flow cell surface

During the experiments, the permeability was monitored and the biofilm growth on the sensor and on the membranes was detected with OCT. Fig. 5-3 shows the permeability decline and the sensor signal for Exp. 1a. In Exp. 1b, where we applied a feed spacer, the sensor signal showed a similar profile as showed in Fig. 5-3 for Exp. 1a (see appendix 5-1). The permeability drastically declined over the first couple of days, stabilizing to a value that was maintained until day 11. After ten days there was a second decline of permeability, which was a sign of severe fouling. The wish is to avoid this impairment of the membrane performance by an early

warning tool. Obviously, the sensor operated with a smooth metal surface is not able to deliver such early warning. The fact that no biofilm developed on the sensor surface is corroborated by OCT imaging. OCT could not detect any accumulation on the measuring surface of the sensor (Fig. 5-3b). On the other hand, biofilm formation was clearly observed on the membrane. One could argue that the feed spacer laid on top of the membrane can facilitate biological growth by inducing dead zones in the flow field, thereby promoting biofilm development in the FMM. However, Exp. 1b demonstrated that the spacer in the sensor flow cell does not significantly improve cells attachment directly on the measuring surface (appendix 5-1). Reasonably, the membrane material (cross-linked polyamides) has a higher propensity to fouling than stainless steel. Additionally, concentration polarization (CP) increases the availability of nutrients in the membrane vicinity. However, Radu et al. observed that the effect of CP can be limited by the substrate consumption rate (Radu et al. 2012). If the concentration of acetate in the bulk is already high and the rate at which microorganisms consume the substrate is comparatively low, the increase of the acetate concentration due to CP does not imply a faster biological growth. Although the work of Radu et al. has been very much cited by RO-related articles (Costa et al. 2021; Kerdi et al. 2020; Bouma et al. 2018; Goh et al. 2018; Imbrogno et al. 2017; Ying et al. 2013)], the aspect of metabolism limitations in spacer-filled channels has not been recalled in literature. This is probably due to the scarcity of studies about RO applied to streams with high concentrations of fast degradable organic compounds. Another factor favoring membrane biofouling with respect to sensor biofouling might be flux through the membrane itself, that fosters the convective transport of microbes towards the membrane surface. All these factors induce preferential fouling of the membrane with respect to the sensor surface. To tackle this problem, the sensor surface was modified in a way that made it appealing for microorganisms to attach to it.

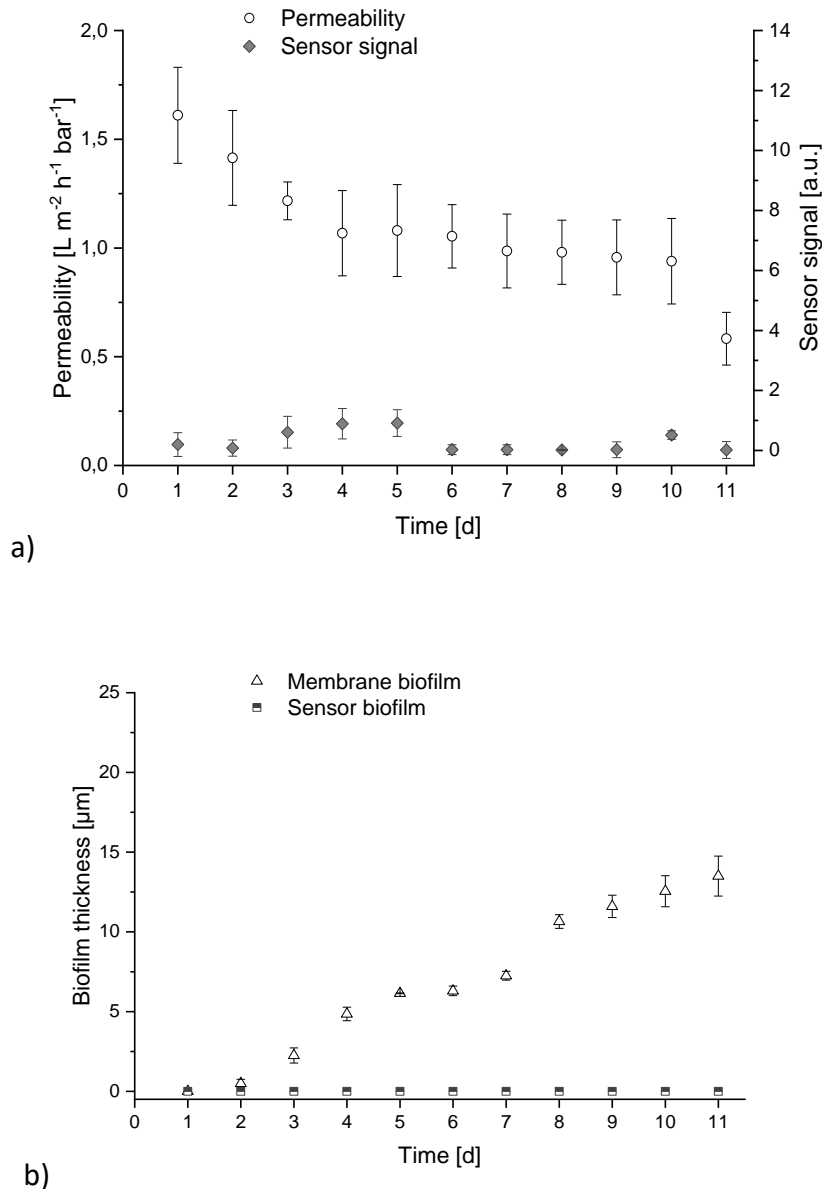


Fig. 5-3 a) Permeability and biofilm sensor signal; b) biofilm thickness on the membrane and on the sensor for the experiment with the unmodified flow cell measured with OCT. The error bars represent the deviation between the average values of the two FMM.

5.3.2 Biofilm detection with a sandblasted flow cell surface

The second fouling experiment (Exp. 2) was run under the same conditions as Exp. 1, only with the modified flow cell surface. Two runs (Exp. 2a and 2b) were performed to provide a duplicate. No spacer was placed inside the roughened flow cell. The idea was to not interfere with the functioning of the sensor, since the heat transfer area occupies around 2 cm^2 . Moreover, Exp. 1b operated with spacer did not show any impact on bacterial attachment directly on the sensor surface.

The results nicely show that the surface modification allowed for a detection of biofilm growth similar to the one on the membrane (Fig. 5-4). A reproducible pattern for permeability decline was observed and the biofilm on the membrane also reached a comparable thickness as in the previous experiment. The sensor signal continuously increased during Exp. 2a (Fig. 5-4). In the second run (Exp. 2b) it remained stable from day six up to day ten. The same profile was observed for biofilm growth on the sensor. In general, the biofilm thickness (measured with OCT) on the membrane was higher than the one on the sensor, which is probably due to one or more of the above-mentioned factors that preferentially promote biofilm attachment on the membrane. As already mentioned, the colonization of the sensor flow cell is independent from the presence of a spacer on top of the measuring surface. This means that the sensor can uncouple feed-spacer fouling from membrane surface fouling. In other words, an increase of the sensor signal is a sign that the membrane is getting fouled, but does not tell anything about the condition of the spacer in the membrane module.

The reason why biofilm growth resulted in an increase of the sensor signal can be found in the Fourier's law of thermal conduction (Eq. 5-2):

$$P = k \frac{\Delta T}{L} = \frac{\Delta T}{R} \quad \text{Eq. 5-2}$$

Where P is the power provided by the sensor heater (W), ΔT is the temperature difference between the surface and the fluid (K), k is the material's conductivity (W m K^{-1}), L is the thickness of the conductive layer (m) and R is the conductive resistance across the diffusive layer (K W^{-1}). As biofilm accumulates on the sensor surface, the thermal resistance of the biofilm is added to the one of the stainless-steel plate placed on top of the sensor and the power provided by the sensor heater to maintain a fixed temperature difference decreases, as described in Eq. 5-3. The decrease of the supplied power is elaborated by a transducer and results in a higher signal of the biofilm sensor.

$$P_0 = \frac{\Delta T}{R_{ss}} > \frac{\Delta T}{R_{ss}+R_{bf}} = P_t \quad \text{Eq. 5-3}$$

Where P_0 and P_t are the powers supplied by the heater at time zero and at time t , respectively. R_{ss} and R_{bf} represent the conductive resistances across the stainless-steel plate and across the biofilm layer, respectively. It is generally assumed that heat transfer across biofilms occurs via conduction, since the velocity field of water inside biofilms can be neglected (Characklis et al. 1981).

R_{bf} can be expressed as the ratio between the biofilm thickness L_{bf} and the biofilm conductivity k_{bf} (Eq. 5-4). A thicker biofilm layer implies a higher conductive resistance. This is true if one assumes that the biofilm conductivity remains constant over time, neglecting the effect that biofilm compaction might have on k_{bf} .

$$R_{bf} = \frac{L_{bf}}{k_{bf}}$$

Eq. 5-4

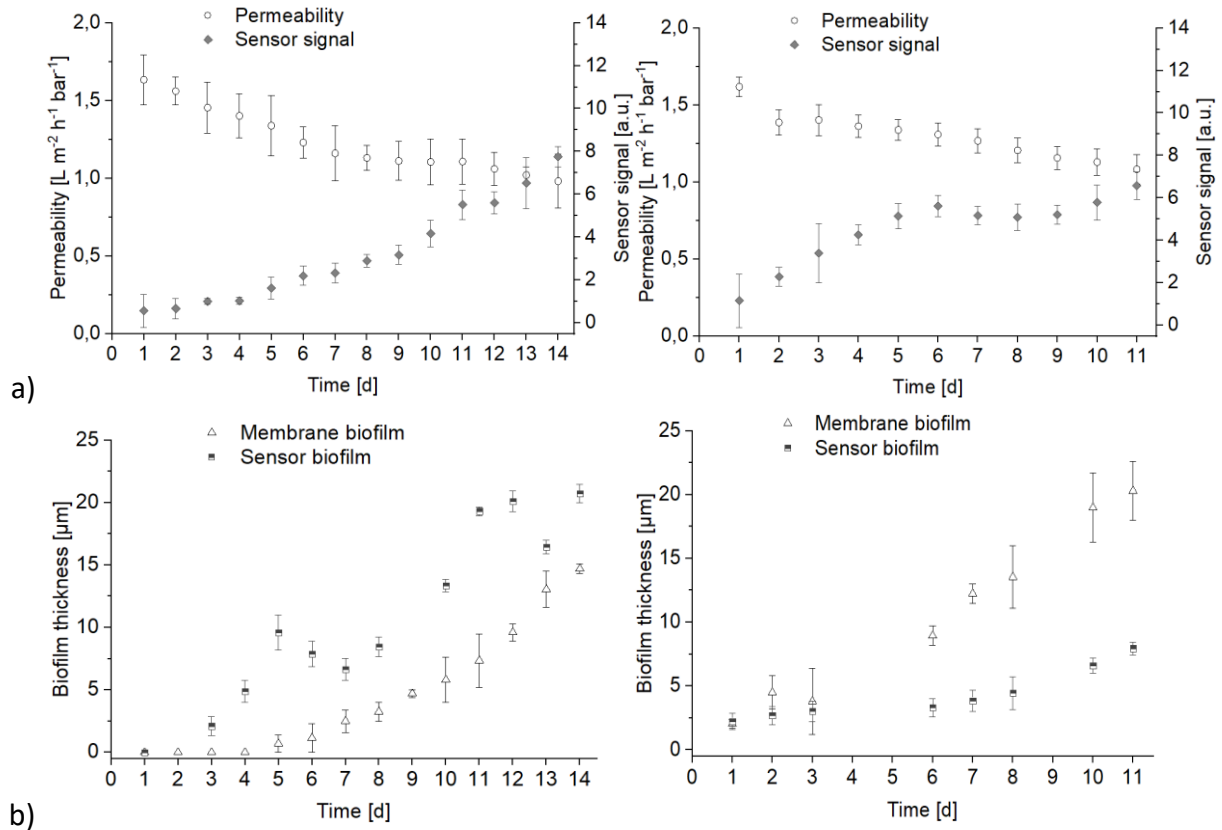


Fig. 5-4 a) Permeability and biofilm sensor signal; b) biofilm thickness on the membrane and on the sensor for the experiment with the sandblasted flow cell measured with OCT. Exp. 2a (left) and Exp. 2b (right).

As for the statistical significance of the trend, a regression analysis was performed to quantify the relation between sensor signal increase and permeability decline. The analysis was performed on the series of data collected in Exp. 2a and 2b. For Exp. 2a, the coefficient of multiple correlation (R) was 0.88, while for Exp. 2b R was equal to 0.89. This means that, although the relation between sensor signal increase and permeability decline is weakly linear, it is statistically relevant.

In the present work no estimation of the variability of biofilm thickness along the membrane module is provided, since OCT imaging of the membrane surface was performed using only one window. However, a previous work performed under the same conditions and using the same FMM showed that spacer fouling increased by 50% through the modules, while the biofilm thickness on the membrane was uniform (Pratofiorito et al. 2022).

Considering the DOC values of feed, concentrate and permeate, it is possible to quantify the increment of substrate concentration on the membrane surface compared to the concentration near the sensor. Hereunder, it is assumed that acetate is the only DOC source

in the system, since the main products of an anaerobic biofilm fed with acetate are methane and carbon dioxide. The concentration of the concentrate can be calculated with Eq. 5-5.

$$C_c = \frac{(Q_c + Q_p) \cdot C_f - Q_p C_p}{Q_c} \quad \text{Eq. 5-5}$$

Where Q_c is the volumetric flowrate of concentrate, Q_p is the volumetric flowrate of permeate, and C_f , C_p and C_c are the concentrations of substrate in the feed, in the permeate and in the concentrate, respectively. Given the average DOC concentrations $C_f = 6.6 \text{ g L}^{-1}$, $C_p = 1.1 \text{ g L}^{-1}$, and the flowrates $Q_c = 51 \text{ L h}^{-1}$ and $Q_p = 0.65 \text{ L h}^{-1}$, Eq. 5-5 returns a C_c of 6.7 g L^{-1} . That is an increment of only 2% with respect to the concentration of the feed. However, due to CP, the concentration on the membrane can be significantly higher than in the bulk. A first approximation of the substrate concentration on the membrane surface (C_m) can be derived by Eq. 5-6 (Jung et al. 2020).

$$C_m = C_c \exp\left(\frac{u_w \delta}{D}\right) \quad \text{Eq. 5-6}$$

With u_w being the permeation velocity through the membrane, δ the thickness of the concentration boundary layer and D the diffusion coefficient of acetate in water. u_w can be calculated dividing the Q_p times the membrane surface and is equal to $6.5 \times 10^{-6} \text{ m s}^{-1}$. D is approximately $1.2 \times 10^{-9} \text{ m}^2 \text{ s}^{-1}$ ([https://classes.engineering.wustl.edu/eece503/Lecture Notes](https://classes.engineering.wustl.edu/eece503/Lecture%20Notes), accessed on 23.08.2022). δ can be approximated with $100 \text{ }\mu\text{m}$ (Jung et al. 2020). Substituting in Eq. 5-6 yields $C_m = 11 \text{ g L}^{-1}$.

The effect of CP increases the availability of substrate at the membrane surface. However, in this study, the substrate concentration in the feed was well above the half-saturation coefficient. Under such condition, the growth rate follows a zero-order kinetic and an increase of the substrate concentration does not have any impact on biomass growth (Radu et al. 2012). In oligotrophic environments, biofilm growth would be more affected by CP. Probably, the low DOC concentration of a pretreated feed for seawater desalination would enhance even more the preferential fouling of the membrane, making the application of such sensor unfeasible. Fig. 5-5 depicts the difference in the concentration profiles near the membrane and near the sensor surface.

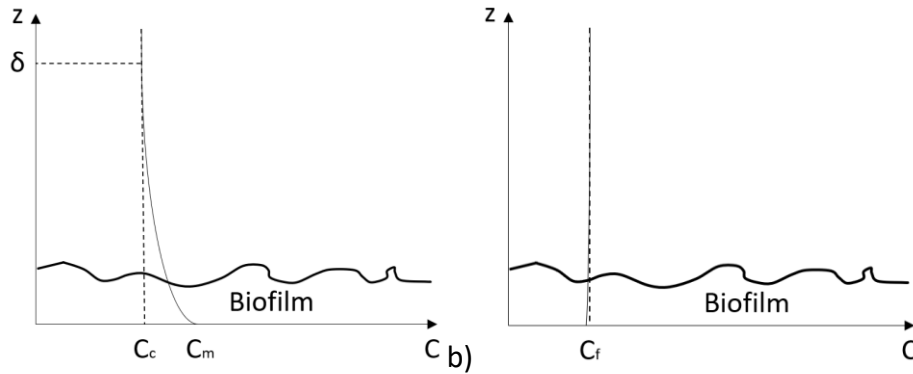


Fig. 5-5 Estimated substrate concentration profiles near the membrane surface C_m (a) and near the sensor surface $\sim C_f$ (b). Due to the very thin biofilm thickness and the low amount of biomass the consumption is nearly neglectable.

It has been argued that, besides CP, the convective flow through the biofilm matrix would also foster biofilm growth, but again this effect is more pronounced if the substrate concentration in the bulk is low (Radu et al. 2012). Considering our experimental conditions, the convective transport of the substrate did not play a significant role in biofilm development. What did play a role was the transport of planktonic cells towards the membrane and the consequent enhancement of biomass attachment rate. This caused the preferential fouling of the permeable support (the membrane) compared to the non-permeable support (the sensor surface) in Exp. 1a and 1b. The role of planktonic cells as foulant was already observed elsewhere (Hansen et al. 2021). The roughening of the sensor flow cell overcame the bottleneck, providing a higher surface for bacterial deposition. Moreover, the increased roughness offered regions of reduced shear stress where the first colonies could start to build up. A previous study investigated the relation between substratum topography, flow velocity and bacterial adhesion rate (Scheuerman et al. 1998). Results showed that the initial attachment rate increased when the experiments were performed on a rough substrate and at higher velocity (which increased the biomass load and thus the frequency of microorganism collisions with the surface). More recently, Ammar et al. developed a model to describe bacterial adhesion on a rough surface for different ionic strengths (Ammar et al. 2015). The comparison of Computational Fluid Dynamics (CFD) simulations and the deposition measured in a flow cell validated the model. The authors concluded that an increase of the asperity size weakens the electrostatic repulsion between the bacterial cell and the substrate, thereby favoring the deposition.

The biofilm on the sensor was much thicker in Exp. 2a. Nevertheless, the values of sensor signal were comparable in both experiments (see Fig. 5-4). This would intuitively contrast with the assumption that the sensor signal is proportional to the biofilm height. To explain this discrepancy, it is useful to examine the biofilm morphology revealed by OCT images. During the first run (Exp. 2a), the formation of flocs on the sensor surface was observed (images are provided in the appendix 5-2). These flocs hovered in the channel of the flow cell and were attached only with a filament to the base of the structure, giving nearly no contribution to

thermal resistance. In turn, they were taken into the calculation for biofilm height. However, the thickness of the layer growing directly on the sensor surface was similar for the two runs. This layer was always thinner than 20 μm . A second analysis of the OCT datasets, where all biofilm above 20 μm was cropped out, resulted in maximum biofilm thickness of 13 μm , which is closer to the one of the second run (Exp. 2b). Also, the sensor sensitivity (μm of biofilm per unit sensor signal) was comparable between the two runs for the second data evaluation (1.2 μm for Exp. 2a and 1.3 μm for Exp. 2b). The results of the second data analysis are available in the appendix 5-3. One must therefore consider that the thermal resistance provided by a fluffy biofilm is substantially different than the one provided by a compact one and that the sensor is mostly sensitive to the biofilm growing directly on the surface and to a much lesser extent to the flocs that float in the liquid phase. This stresses the importance of the biofilm morphology and thereby the chosen flow velocity above the sensor surface. No information about the structure of the deposit can be derived by the sensor signal as such. Still, the signal is an estimation of the quantity of biofilm present on the surface, which helps to infer the state of the system.

An experiment with a superficial velocity of 0.02 m s^{-1} inside the sensor flow cell was performed (Exp. 2c) and the results can be found in the appendix 5-4. At a lower superficial velocity, the sensitivity of the sensor was lower (2.3 μm). No significant difference between the biofilm structure in Exp. 2c and in Exp. 2b was observed. Hence, we conclude that the worsening of the heat transfer in the liquid phase caused by the reduced superficial velocity made the thermal resistance of the biofilm negligible. This explains why a thicker biofilm is needed to generate a signal.

5.3.3 Cleaning of the membrane and the sensor

To simulate the full operation of a membrane, a further experiment (Exp. 3) was carried out, where the membrane and the sensor were fouled and subsequently cleaned. The aim was to test the sensor response to cleaning.

The profiles of permeability, biofilm growth and sensor signal were similar as for Exp. 2 (Fig. 5-6). Given the considerations of the previous section, the biofilm thickness was calculated by cropping all biofilm growing above 20 μm from the sensor surface, to exclude the contribution of the flocs. The sensor sensitivity was 1.4 μm .

As the permeability dropped to 50% of the post conditioning value (from 1.5 to 0.75 $\text{L m}^{-2} \text{h}^{-1} \text{bar}^{-1}$), the setup was flushed with NaOH at pH 11.5 for 6 h. The temperature was constantly kept at 37 $^{\circ}\text{C}$ and OCT imaging was performed on the sensor during cleaning. Pictures showing the effect of cleaning on the sensor surface are provided in the appendix 5-5. The cleaning partially restored permeability to approximately 0.95 $\text{L m}^{-2} \text{h}^{-1} \text{bar}^{-1}$. This value corresponds to the permeability value of day 5. A large amount of biofilm on the sensor was dissolved and the thickness dropped below 5 μm . The sensor signal dropped to approximately 8 a.u. after cleaning. These were the values of day 5, which is consistent with the partial restoration of permeability. That indicates that the sensor reacts to cleaning with a drop of the signal

proportional to the loss of biofilm on the measuring surface and to the restoration of permeability.

While the biofilm on the sensor was largely removed after flushing the system with NaOH, the one on the membrane was still present in a considerable amount (60% of the biofilm before cleaning, similar to day 6).

The retention of the membrane with respect to DOC and TN was measured at the beginning of the experiment, before cleaning and after cleaning. In general, DOC and TN retentions slightly increased as the membrane fouled (see appendix 5-6). This increase can possibly be ascribed to the compactness of the biofilm, able to retain more dissolved substances as the matrix became thicker. The high pressure used in this study has certainly favored the formation of a rather compact biofilm. The phenomenon of biofilm-enhanced rejection of small solutes is already reported in literature for compact biofilms (Shen et al. 2014). The main mechanism by which a compact biofilm reduces permeation is the hindering of diffusion across the biofilm layer (Radu et al. 2010). To a lesser extent, microbial metabolism on the membrane surface might have consumed acetate and nitrogen. Cleaning did not significantly alter the retention, indicating that the membrane was not damaged by the caustic environment (Huang et al. 2020).

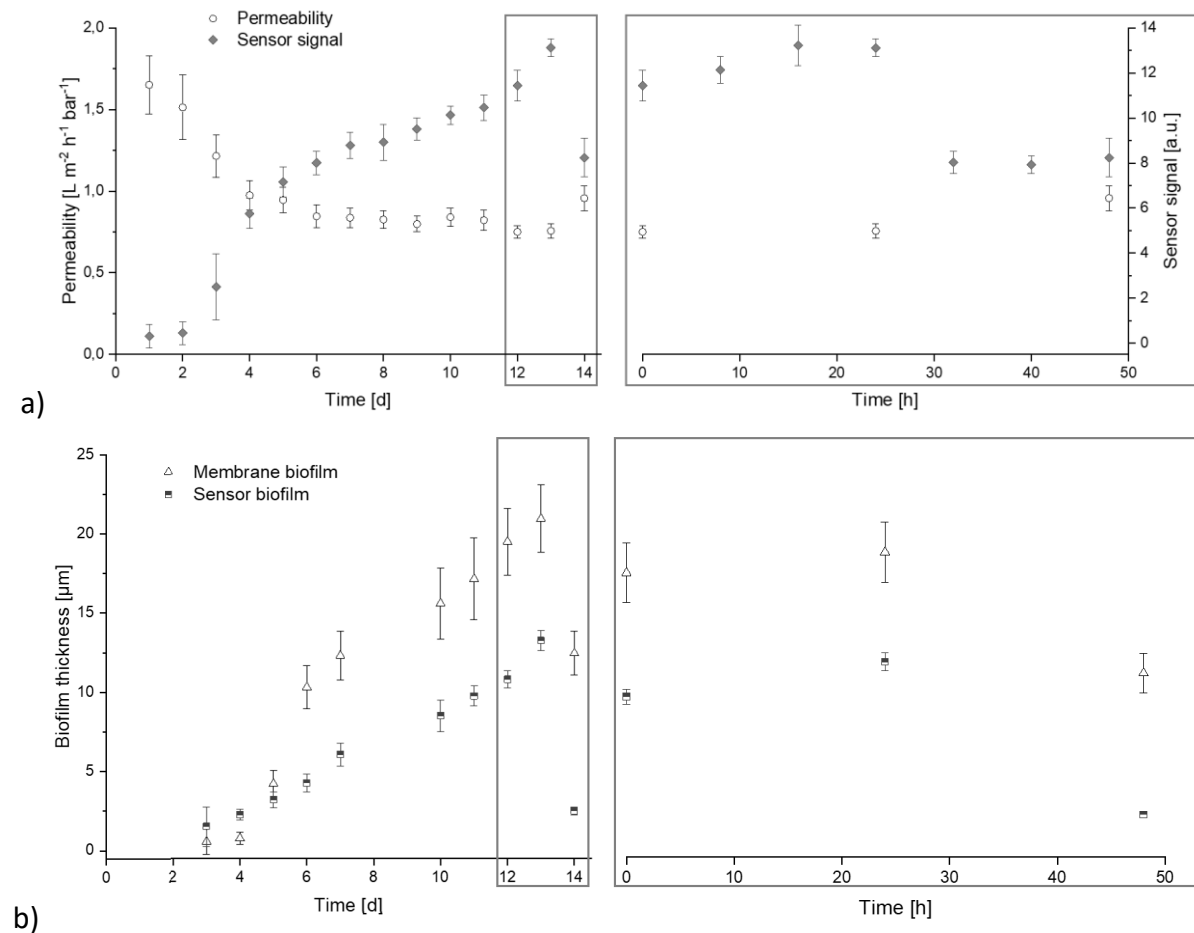


Fig. 5-6 a) Permeability and biofilm sensor signal; b) biofilm thickness on the membrane and on the sensor before and after cleaning measured by OCT (Exp. 3). Time span of cleaning: h 24 to h 30.

5.4 Conclusions

The possibility to use a biofilm sensor as an early warning tool for permeability decline in RO setups was assessed. A sensor with a smooth surface was operated in a flow cell, which was set parallel to two flat sheet membrane modules (FMM). No biofilm attachment on the sensor surface could be detected, whereas the biofilm formation in the feed channel of the FMM under comparable condition could clearly be visualized by OCT.

By offering a rougher sensor surface, cell deposition, biofilm growth and finally the sensor signal were improved. The biofilm development on the membrane was comparable to the one on the sensor surface, which could be proved by imaging and quantification with OCT. The recorded biofilm sensor signal indicates the upcoming final drop of permeability in the FMM. Membrane cleaning with NaOH partially restored permeability and simultaneously removed biofilm from the sensor surface. As a consequence, the sensor signal decreased. The presented results clearly demonstrate the potential of biofilm sensors to be used for knowledge-based cleaning cycles optimization. These sensors may realistically be applied in pilot scale plants for RO. The interpretation of the signal depends on the specific conditions of the process. There is the need to collect data for the specific application by performing several runs. If the correlation between sensor signal and permeability is reproducible, a value of sensor signal could be defined as threshold above which cleaning is necessary to avoid severe fouling.

6 Summary

The present dissertation discusses the optimization of a RO unit for the concentration of VFA in a two-stage fermentation process for the production of biogas. The work covered three main aspects: (I) the maximization of the VFA yield via mass balances; (II) the differentiation of biofouling on the spacer and on the membrane and the study of the impact of these two types of fouling on the membrane performance; and (III) the use of a biofilm sensor to predict membrane performance.

Chapter 3 faced the problem of the loss of VFA in the permeate due to an excessive increase of the recovery. The RO setup was equipped with a recirculation system that permitted to regulate the ratio between the volume flowrates of the concentrate and permeate. Two optimal recoveries were defined for two different operating pressures. These values assure that the concentration of VFA in the concentrate is maximized and that a limited quantity of solute gets lost in the permeate. The tradeoff corresponds to the point at which the excessive concentration of VFA on the feed side of the membrane starts being detrimental for the reclamation yield. The calculation of the osmotic pressure inside the feed channel at different recoveries could support the results of the mass balances. However, the results shall not be generalized. Different boundary conditions (feed composition, type of membrane, etc.) would have led to different optimal recoveries. Nevertheless, the presented results are a reliable benchmark for similar applications.

The concentrations of acetate reported in chapter 3 were as high as 30 g L^{-1} . Such a high availability of nutrients implies an issue for the long-term operability of the RO unit: biofouling. In Chapter 4 a method for the differentiation of biofilm growth on the feed spacer (described by the parameter SP) and on the membrane (described by the parameter ME) was presented. The method was applied to examine the interaction between these two kinds of fouling and two operating parameters: permeability and pressure drop along the module. Spacer fouling occurred mostly during the first half of the experiment, contributing to the increase of the pressure drop. An additional contribution to the pressure drop came from membrane fouling, during a later stage. Interestingly, pressure drop increased independently from flux decline, probably due to the short modules. Moreover, permeability decreased independently from surface coverage. These last two facts prove the following: (I) pressure drop might be a poor indicator for biofouling severity and (II) biofilm growth on the membrane occurs before the permeability decline. This motivated the investigation of biofilm sensors for predicting the membrane performance (chapter 5).

A biofilm sensor was embedded in a flow cell and installed in parallel to two FMM. Both the sensor and the membrane surface were pictured with OCT and the membrane performance was constantly monitored. During the first trials, biofilm only grew on the membrane but not on the sensor surface. Therefore, the sensor could not deliver any signal. The bottom of the sensor flow cell was then modified to promote biofilm attachment. The modification was successful and biofilm could grow on the sensor surface as well as on the membrane, when the experiments were repeated. The sensor signal increased as the permeability dropped and

the biofilm thickness on the sensor was proportional to the sensor signal. This finding encourages the use of the sensor for a rough estimation of the amount of biofilm in RO systems. Based on the sensor signal, cleaning agents can be flushed in the spiral-wound module. The response of the sensor to cleaning was tested too. Although cleaning was not fully effective, the decrease of the signal correlated well with the restoration of the permeability.

As an outlook, the potential of the DEPOSENS[®] sensor for biofouling monitoring in RO systems must be further investigated. More data need to be collected in order to define knowledge-based control strategies. However, the operating conditions imposed by the specific application might change the fouling rate. Thus, the sensor signal interpretation is highly dependent on the boundary conditions of the process. In general, the sensor might be used to trigger membrane cleaning after the signal reaches a certain threshold. The threshold value observed in this study is around 7 a.u., but this might be different if the operating conditions change.

7 Appendix

Appendix 1-1

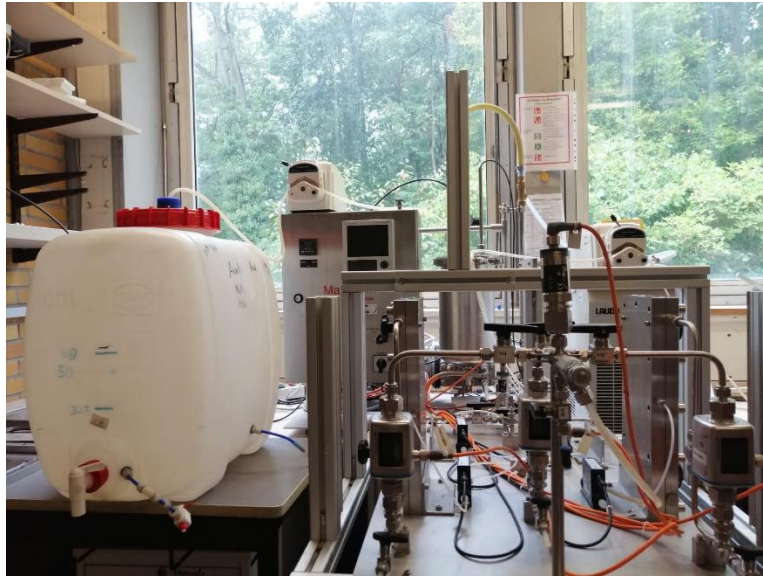
Characterization of the real hydrolysate.

| Component | mg L ⁻¹ |
|------------------------------------|---------------------------|
| Formic acid | 120 |
| Acetic acid | 12600 |
| Propionic acid | 980 |
| n-Butyric acid | 2480 |
| Lactic acid | 680 |
| NH ₄ ⁺ | 6.6 |
| Na ⁺ | 96 |
| K ⁺ | 2268 |
| Ca ²⁺ | 1369 |
| Zn ²⁺ | 56 |
| Fe ²⁺ /Fe ³⁺ | 0.94 |
| Br ⁻ | 29 |
| Cl ⁻ | 383 |
| F ⁻ | < 1 |
| NO ₂ ⁻ | < 1 |
| NO ₃ ⁻ | < 1 |
| SO ₄ ²⁻ | 39 |
| PO ₄ ³⁻ | 27 |
| TOC | 13420 |
| DOC | 9920 |
| TN | 2836 |
| COD | 30000 |
| TSS | 19000 |
| Electrical conductivity | 21 [mS cm ⁻¹] |
| pH | 5.6 [-] |

Appendix 3-1

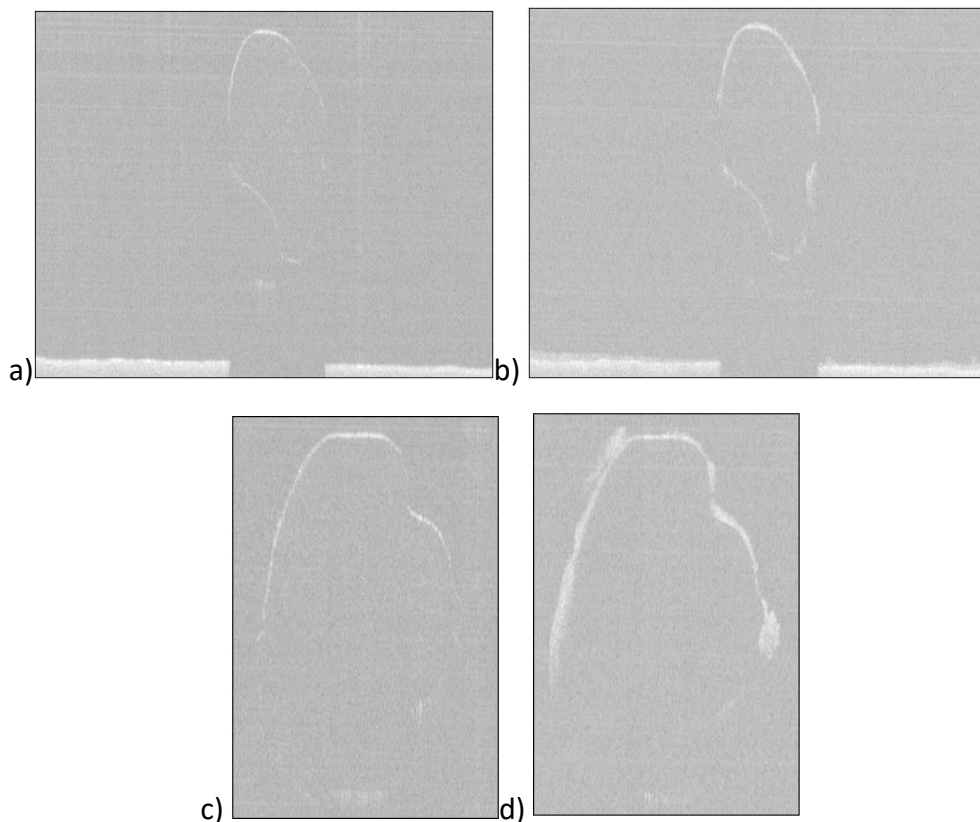


Flat sheet module. Feed side on the right and permeate side on the left.



LPRO setup. The two modules are placed vertically (on the right).

Appendix 4-1



2D pictures of the cross section of the spacer-filled channel. Membrane fouling from day 0 to day 26 can be seen in a) and b); spacer fouling is more evident in c) and d). The missing part of membrane in a) and b) is due to the shadowing effect of the spacer.

Appendix 4-2

L_{sp} values along the Y-direction. Module 1, lower position.

| Y-direction [pixels] | L_{sp} [pixels] |
|-----------------------------|-------------------------------------|
| 1 | 308 |
| 130 | 255 |
| 235 | 165 |
| 236 | 185 |
| 320 | 318 |
| 440 | 305 |
| 552 | 225 |
| 615 | 329 |

L_{sp} values along the Y-direction. Module 1, middle position.

| Y-direction [pixels] | L_{sp} [pixels] |
|-----------------------------|-------------------------------------|
| 100 | 200 |
| 101 | 200 |
| 160 | 326 |
| 284 | 320 |
| 351 | 186 |
| 352 | 184 |
| 399 | 186 |
| 400 | 186 |

L_{sp} values along the Y-direction. Module 1, upper position.

| Y-direction [pixels] | L_{sp} [pixels] |
|-----------------------------|-------------------------------------|
| 50 | 203 |
| 51 | 215 |
| 215 | 300 |
| 302 | 210 |
| 303 | 201 |
| 385 | 332 |
| 595 | 235 |
| 596 | 194 |

L_{sp} values along the Y-direction. Module 2, lower position.

| Y-direction [pixels] | L_{sp} [pixels] |
|-----------------------------|-------------------------------------|
| 1 | 150 |
| 2 | 306 |
| 192 | 222 |
| 193 | 195 |
| 376 | 287 |
| 486 | 222 |
| 487 | 212 |
| 605 | 140 |

L_{sp} values along the Y-direction. Module 2, middle position.

| Y-direction [pixels] | L_{sp} [pixels] |
|----------------------|-------------------|
| 1 | 108 |
| 2 | 206 |
| 186 | 307 |
| 345 | 212 |
| 346 | 212 |
| 503 | 305 |
| 624 | 182 |
| 625 | 204 |

L_{sp} values along the Y-direction. Module 2, upper position.

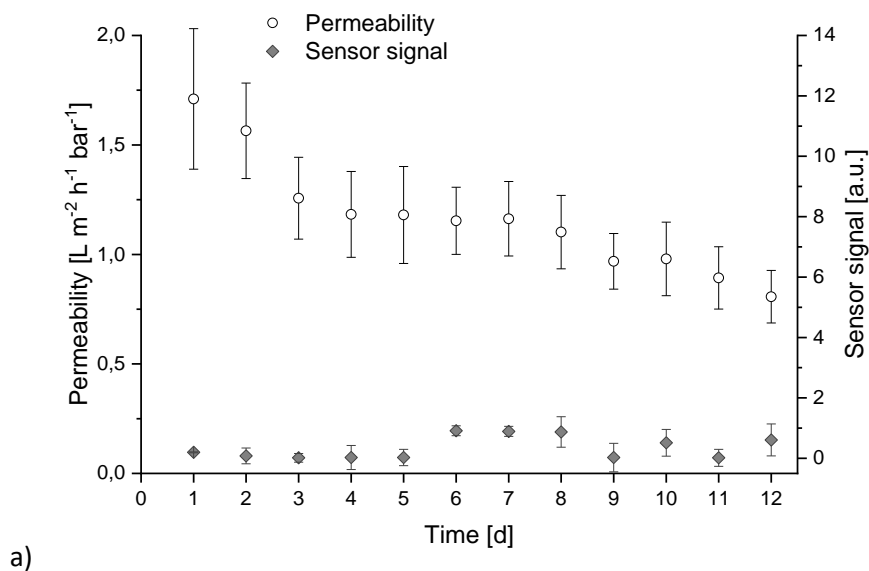
| Y-direction [pixels] | L_{sp} [pixels] |
|----------------------|-------------------|
| 1 | 350 |
| 95 | 160 |
| 96 | 205 |
| 250 | 145 |
| 251 | 230 |
| 405 | 185 |
| 406 | 185 |
| 555 | 265 |

L_{sp} was calculated drawing a line in the X-direction using the built-in function "Straight".
 Pixels dimensions (x;y;z): 8 μm ; 8 μm ; 3.14 μm .

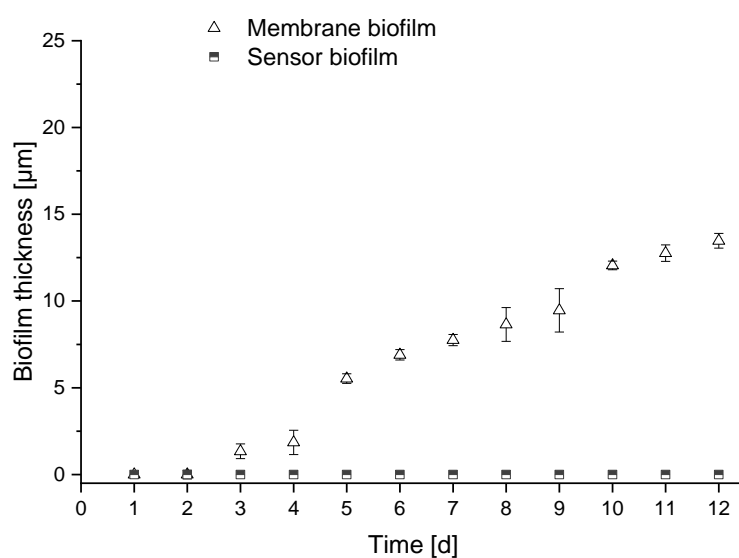
Average values of SP for the 6 positions at day 26.

| Position | SP [μm] |
|---------------|------------------------|
| Module 1 up | 42 |
| Module 1 mid | 36 |
| Module 1 down | 27 |
| Module 2 up | 47 |
| Module 2 mid | 33 |
| Module 2 down | 31 |

Appendix 5-1



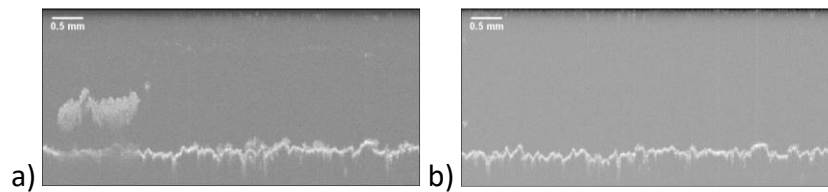
a)



b)

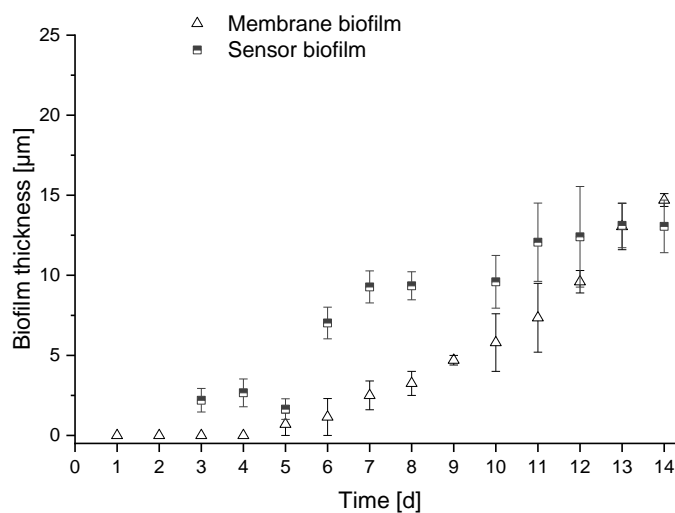
a) Permeability and biofilm sensor signal; b) biofilm thickness on the membrane and on the sensor for the experiment with the unmodified flow cell and with spacer measured with OCT (Exp. 1b). In the flow cell, biofilm grew only on the spacer, but not on the bottom of the channel. Therefore, it did not deposit on the measuring surface.

Appendix 5-2



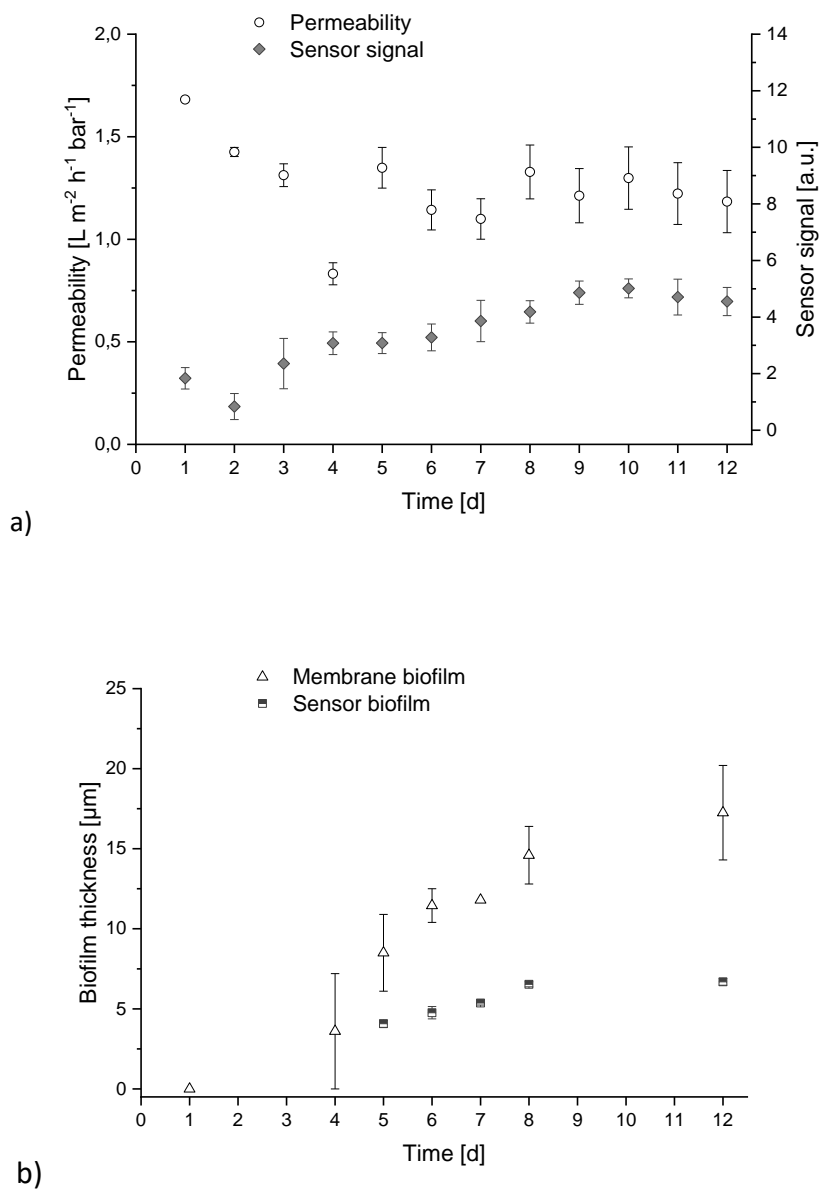
Sensor surface before the cleaning (a); sensor surface after the cleaning (b). Flow direction to the right.

Appendix 5-3



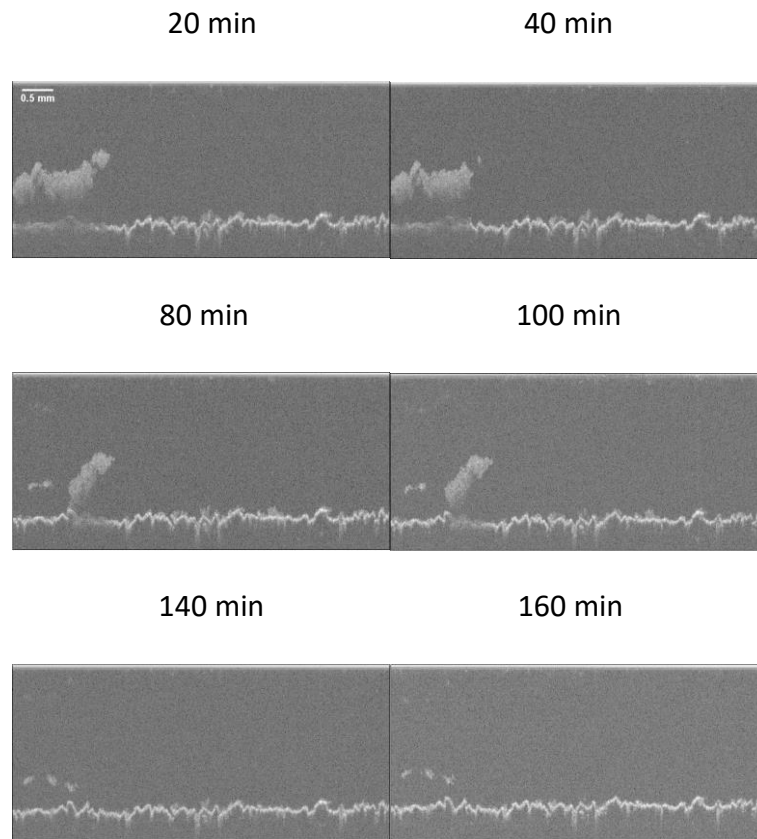
Biofilm thickness on the membrane and on the modified sensor surface measured with OCT (Exp. 2a). For the image analysis, all biofilm higher than 20 μm was cropped out.

Appendix 5-4



a) Permeability and biofilm sensor signal; b) biofilm thickness on the membrane and on the modified sensor surface measured with OCT (Exp. 2c). Superficial velocity in the sensor flow cell: 0.02 m s^{-1} . At day two the room temperature dropped after a cold night, making the sensor display a negative value. For the sake of data representation, the signal values were all increased by 2.

Appendix 5-5



Sensor surface during the cleaning.

Appendix 5-6

DOC and TN retention values for Exp. 3. The errors represent the deviation between the retentions of the two FMM.

| Retention | DOC | TN |
|-----------------|----------|-----------|
| Beginning | 78% ± 3% | 83% ± 5% |
| Before cleaning | 86% ± 4% | 89% ± 10% |
| After cleaning | 85% ± 4% | 91% ± 8% |

8 Reference

- Abbt-Braun G., Lankes U., Frimmel F.H. "Structural characterization of aquatic humic substances – The need for a multiple method approach." *Aquatic Sciences*, 2004: 66 151–170
<https://doi.org/10.1007/s00027-004-0711-z>.
- Abushaban A., Salinas-Rodriguez S.G., Pastorelli D., Schippers J.C., Mondal S., Goueli S., Kennedy M.D. "Assessing Pretreatment Effectiveness for Particulate, Organic and Biological Fouling in a Full-Scale SWRO Desalination Plant." *Membranes*, 2021 , 11(3).
- Aktija, S.A., A. Zirehpour, A. Mollahosseini, M.J. Taherzadeh, A. Tiraferri, and A. Rahimpour. "Feasibility of membrane processes for the recovery and purification of bio-based volatile fatty acids: A comprehensive review." *J. Ind. Eng. Chem.*, 2020: 81, 24–40.
- Ali R., Saravia F., Hille-Reichel A., Härrer D., Gescher J., Horn H. "Enhanced production of propionic acid through acidic hydrolysis by choice of inoculum." *J. Chem. Technol. Biotechnol.*, 2020: 96, 207–216, doi:10.1002/jctb.6529.
- Ali S.M., Qamar A., Kerdi S., Phuntsho S., Vrouwenvelder J.S., Ghaffour N., Shon H.K. "Energy efficient 3D printed column type feed spacer for membrane filtration." *Water Research* 164, 2019: 114961. <https://doi.org/10.1016/j.watres.2019.114961>.
- Al-Juboori R.A., Yusaf T. "Biofouling in RO system: mechanisms, monitoring and controlling." *Desalination*, 2012: 302 1-23, <http://dx.doi.org/10.1016/j.desal.2012.06.016>.
- Atasoy M., Owusu-Agyeman I., Plaza E., Cetecioglu Z. "Bio-based volatile fatty acid production and recovery from waste streams: current status and future challenges." *Bioresource Technology*, 2018 268.
- Bär K., Merkle W., Tuczinski M., Saravia F., Horn H., Orloff F., Graf F., Lemmer A., Kolb T. "Development of an innovative two-stage fermentation process for high calorific biogas at elevated pressure." *Biomass and Bioenergy* 115, 2018: 186–194.
<https://doi.org/10.1016/j.biombioe.2018.04.009>.
- Bauer A., Wagner M., Horn H., Saravia F. "Operation conditions affecting scale formation in membrane distillation – An in situ scale study based on optical coherence tomography." *Journal of Membrane Science* 623, 2021: 118989.
<https://doi.org/10.1016/j.memsci.2020.118989>.
- Bauer A., Wagner M., Saravia F., Bartl S., Hilgenfeldt V., Horn H. "In-situ monitoring and quantification of fouling development in membrane distillation by means of optical coherence tomography." *Journal of Membrane Science* 577 (2019), n.d.: 145-152
<https://doi.org/10.1016/j.memsci.2019.02.006>.
- Bellona C., Drews J.E. "The role of membrane surface charge and solute physico-chemical properties in the rejection of organic acids by NF membranes." *J. Membr. Sci.*, 2005: 249, 227–234, doi:10.1016/j.memsci.2004.09.041.
- Benecke J., Rozova J., Ernst M. "Anti-scale effects of select organic macromolecules on gypsum bulk and surface crystallization during reverse osmosis desalination." *Separation and Purification Technology*, 2018: 68-78 198 <https://doi.org/10.1016/j.seppur>.

- Blandin G., Rosselló B., Monsalvo V.M, Batlle-Vilanova P., Viñas J.M., Rogalla F., Comas J. "Volatile fatty acids concentration in real wastewater by forward osmosis." *J. Membr. Sci.*, 2019: 575, 60–70, doi:10.1016/j.memsci.2019.01.006.
- Bolaji I.O., Dionisi D. "Acidogenic fermentation of vegetable and salad waste for chemicals production: effect of pH buffer and retention time." *J. Environ. Chem. Eng. 5*, 2017: 5933–5943.
- Bouma A.T., Lienhard J.H. "Split-feed counterflow reverse osmosis for brine concentration." *Desalination 445*, 2018: 280 – 291. <https://doi.org/10.1016/j.desal.2018.07.011>.
- Bucs S., Farhat N., Kruithof J.C., Picioreanu C., van Loosdrecht M.C.M., Vrouwenvelder J.S. "Review on strategies for biofouling mitigation in spiral wound membrane systems." *Desalination*, 2018: 434, 189-197. <https://doi.org/10.1016/j.desal.2018.01>.
- Choi, J.H., K. Fukushi, and K. Yamamoto. "A study on the removal of organic acids from wastewaters using nanofiltration membranes. ." *Sep. Purif. Technol.*, 2008: 59, 17–25, doi:10.1016/j.seppur.2007.05.021.
- Costa F.C.R., Ricci B.C., Teodoro B., Koch K., Drewes J.E., Amaral M.C.S. "Biofouling in membrane distillation applications - a review." *Desalination 516*, 2021: 115241. <https://doi.org/10.1016/j.desal.2021.115241>.
- Creber S.A., Vrouwenvelder J.S., van Loosdrecht M.C.M., Johns M.L. "Chemical cleaning of biofouling in reverse osmosis membranes evaluated using." *Journal of Membrane Science*, 2010: 362 202–210 <http://dx.doi.org/10.1016/j.memsci.2010.06.052>.
- Curto, D., V. Franzitta, and A. A Guercio. " Review of the Water Desalination Technologies." *Applied Science*, 2021: 11, 670. <https://doi.org/10.3390/app11020670>.
- Desmond P., Huisman K.T., Sanawar H., Farhat N.M., Traber J., Fridjonsson E.O., Johns M.L., Flemming H.C., Picioreanu C., Vrouwenvelder J.S. "Controlling the hydraulic resistance of membrane biofilms by engineering biofilm physical structure." *Water Research*, 2022.
- Farhat N.M., Staal M., Bucs S., Van Loosdrecht M.C.M., Vrouwenvelder J.S. "Spatial heterogeneity of biofouling under different cross-flow velocities in reverse osmosis membrane systems." *Journal of Membrane Science 520*, 2016: 964–971. <https://doi.org/10.1016/j.memsci.2016.08.065>.
- Flemming, H.-C. "Biofouling in water systems—cases, causes and countermeasures." *Appl. Microbiol. Biotechnol.*, 2002: 629–640, <http://dx.doi.org/10.1007/s00253-002-1066-9>.
- Fortunato L., Bucs S., Valladares Linares R., Cali C., Vrouwenvelder J.S., Leiknes T. "Spatially-resolved in-situ quantification of biofouling using optical coherence tomography (OCT) and 3D image analysis in a spacer filled channel." *Journal of Membrane Science 524*, 2017: 673–681. <https://doi.org/10.1016/j.memsci.2016.11.052>.
- Fortunato L., Jeong S., Leiknes T. "Time-resolved monitoring of biofouling development on a flat sheet membrane using optical coherence tomography." *Scientific Reports 7 (1)*, 2017: <https://doi.org/10.1038/s41598-017-00051-9>.

-
- Fortunato L., Pathak N., UrRehman Z., Shon H., Leiknes T. "Real-time monitoring of membrane fouling development during early stages of activated sludge membrane bioreactor operation." *Process Safety and Environmental Protection* 120, 2018: 313–320.
- Fortunato L., Ranieri L., Naddeo V., Leiknes T. "Fouling control in a gravity-driven membrane (GDM) bioreactor treating primary wastewater by using relaxation and/ or air scouring,." *J. Membr. Sci.* 610, 2020: 118261, <https://doi.org/10.1016/j.memsci.2020>.
- Fridjonsson E.O., Creber S.A., Vrouwenvelder J.S., Johns M.L. "Magnetic resonance signal moment determination using the Earth's magnetic field." *Journal of Magnetic Resonance* 252, 2015: 145–150 <https://doi.org/10.1016/j.jmr.2015.01.013>.
- Goh P.S., Lau W.J., Othman M.H.D., Ismail A.F. "Membrane fouling in desalination and its mitigation strategies." *Desalination* 425, 2018: 130-155. <https://doi.org/10.1016/j.desal.2017.10.018>.
- Guo W., Ngo H., Li J. "A mini-review on membrane fouling." *Bioresource Technology*, 2012: 122 27–34 <https://doi.org/10.1016/j.biortech.2012.04.089>.
- Hackbarth M., Jung T., Reiner J.E., Gescher J., Horn H., Hille-Reichel A., Wagner M. "Monitoring and quantification of bioelectrochemical *Kyrpidia spormannii* biofilm development in a novel flow cell setup." *Chemical Engineering Journal* 390, 2020: 124604.
- Han H., Zhang S., Qiao J., Wang X. "An intelligent detecting system for permeability prediction of MBR." *Water Science and Technology* 77 (2)., 2018: <https://doi.org/10.2166/wst.2017.562>.
- Hao J., Wang H. "Volatile fatty acids productions by mesophilic and thermophilic sludge fermentation: biological responses to fermentation temperature." *Bioresour. Technol.* 175, 2015: 367–373.
- Herzberg M., Kang S., Elimelech M. "Role of extracellular polymeric substances (EPS) in biofouling of reverse osmosis membranes." *Environmental Science and Technology* 43, 2009: 4393-4398. <https://doi.org/10.1021/es900087j>.
- "https://classes.engineering.wustl.edu/eece503/Lecture_Notes/ChE_505_Chapter_7N_Appendix.pdf (accessed on 23.08.2022)." 8 23, 2022.
- "<https://www.environmental-expert.com/products/aqua-color-biofilm-sensor-569180> (accessed on 07.04.2022)." 4 7, 2022.
- Huang J., Luo J., Chen X., Feng S., Wan Y. "How do chemical cleaning agents act on polyamide nanofiltration membrane and fouling layer?" *Industrial and Engineering Chemistry Research* 59 (40), 2020: 17653-17670. <https://doi.org/10.1021/acs.iecr.0c03365>.
- Hube S., Wang J., Sim L.N., Chong T.H., Wu B. "Direct membrane filtration of municipal wastewater: Linking periodical physical cleaning with fouling mechanisms." *Separation and Purification Technology* 259, 2021: 118125. <https://doi.org/10.1016/j.seppur.2020.118125>.
- Ibrar I., Naji O., Sharif A., Malekizadeh A., Alhawari A., Alanezi A.A., Altaee A. "A review of fouling mechanisms, control strategies and real-time fouling monitoring techniques in forward osmosis." *Water* 11(4), 2019: 695. <https://doi.org/10.3390/w110406>.
- Imbrogno J., Keating IV J.J., Kilduff J., Belfort G. "Critical aspects of RO desalination: A combination strategy." *Desalination* 401, 2017: 68-87. <http://dx.doi.org/10.1016/j.desal.2016.06.033>.
-

- Jänisch T., Reinhardt S., Pohsner U., Böringer S., Bolduan R., Steinbrenner J., Oechsner H. "Separation of volatile fatty acids from biogas plant hydrolysates." *Sep. Purif. Technol.*, 2019: 223, 264–273, doi:10.1016/j.biortech.2012.12.145.
- Jiang S., Li Y., Ladewig B.P., "A review of reverse osmosis membrane fouling and control strategies." *Science of the Total Environment*, 2017: 595, 567-583
<https://doi.org/10.1016/j.scitotenv.2017.03.235>.
- Jung, O. "Raman Microspectroscopy for In-Situ Measurement of Concentration Polarization in Nanofiltration. Phd Thesis, Karlsruhe Institute of Technology, Karlsruhe, Germany." 2020.
- Kerdi S, Qamar A., Vrouwenvelder J.S., Ghaffour N. "Effect of localized hydrodynamics on biofilm attachment and growth in a cross-flow filtration channel." *Water Research* 188, 2021: 116502. <https://doi.org/10.1016/j.watres.2020.116502>.
- Kerdi S., Qamar A., Alpatova A., Vrouwenvelder J.S., Ghaffour N. "Membrane filtration performance enhancement and biofouling mitigation using symmetric spacers with helical filaments." *Desalination* 484, 2020: 114454. <https://doi.org/10.1016/j.desal.2020.114454>.
- Kerdi S., Qamar A., Vrouwenvelder J.S., Ghaffour N. "Fouling resilient perforated feed spacers for membrane filtration." *Water Research* 140, 2018: 211–219.
<https://doi.org/10.1016/j.watres.2018.04.049>.
- Kumanowska E., Saldaña M.U., Zielonka S., Oechsner H. "Two-stage anaerobic digestion of sugar beet silage: The effect of the pH-value on process parameters and process efficiency." *Bioresource Technology* 245, 2017: 876–883. <https://doi.org/10.1016/j.biortech.2017.09.011>.
- Lemmer, A., Chen, Y., Lindner, J., Wonneberger, A.-M., Zielonka, S., Oechsner, H., Jungbluth, T. "Influence of different substrates on the performance of a two-stage high pressure anaerobic digestion system." *Bioresour. Technol.* 178, 2015: 313–318.
- Li C., Wagner M., Lackner S., Horn H. "Assessing the influence of biofilm surface roughness on mass transfer by combining optical coherence tomography and two-dimensional modeling." *Biotechnol. Bioeng.* 113, 2016: 989–1000. <https://doi.org/10.1002/bit.25868>.
- Li W., Liu X., Wang Y.N., Chong T.H., Tang C.Y., Fane A.G. "Analyzing the evolution of membrane fouling via a novel method based on 3D optical coherence tomography imaging." *Environmental Science and Technology* 50/13, 2016: 6930–6939.
<https://doi.org/10.1021/acs.est.6b00418>.
- Li, Y., A. Shahbazi, K. Williams, and C. Wan. "Separate and concentrate lactic acid using combination of nanofiltration and reverse osmosis membranes. ." *Appl. Biochem. Biotechnol.* , 2008: 147, 1–9, doi:10.1007/s12010-007-8047-5.
- Lim K.B., Wang P.C., An H., Yu S.C.M. "Computational Studies for the Design Parameters of Hollow Fibre Membrane Modules." *Journal of Membrane Science* 529, 2017: 263-273.
<https://doi.org/10.1016/j.memsci.2017.01.053>.
- Lindeboom A., Feroso F.G., Weijma J., Zagt K., Van Lier J.B. "Autogenerative high pressure digestion: anaerobic digestion and biogas upgrading in a single step reactor system." *Water Sci. Technol.*, 64, 2011: 647-653.

-
- Lindner J., Zielonka S., Oechsner H., Lemmer A. "Effect of different pH-values on process parameters in two-phase anaerobic digestion of high-solid substrates." *Environ. Technol.* 36, 2015: 198–207.
- Ludwig T., Gaida D., Keysers C., Pinnekamp J., Bongards M., Kern P., Wolf C., Sousa Brito A.L. "An advanced Simulation model for membrane bioreactors: development, calibration and validation." *Water Science and Technology* 66 (7), 2012: <https://doi.org/10.2166/wst2012.249>.
- Matin A., Rahman F., Shafi H.Z., Zubair S.M. "Scaling of reverse osmosis membranes used in water desalination: Phenomena, impact, and control; future directions." *Desalination*, 2019: 455, 135-157. <https://doi.org/10.1016/j.desal.2018.12.009>.
- Merkle W., Baer K., Haag N., Zielonka S., Ortloff F., Graf F. "High-pressure anaerobic digestion up to 100 bar: influence of initial pressure on production kinetics and specific methane yields." *Environ. Technol.* 38, 2017: (3) (232) 72–78.
- Merkle W., Baer K., Lindner J., Zielonka S., Ortloff F., Graf F., Kolb T., Jungbluth T., Lemmer A. "Influence of pressures up to 50 bar on two-stage anaerobic digestion." *Bioresour. Technol.* 232, 2017: 72–78.
- Min E., Shin J.G., Lee J., Yasuno Y., Lee B.H. "Single-step method for fiber-optic probe-based full-range spectral domain optical coherence tomography." *Applied optics* 52, 2013: 5143-5151.
- Mittenzwey K., Szewzyk U., Dworak V., Schulze D. "Online Sensor zur Erfassung von Biofilmen." *Schriftenreihe Kompetenzzentrum Wasser Berlin Band 4*, 2006: 12004.
- Muha I., Zielonka S., Lemmer A., Schönberg M., Linke B., Grillo A., Wittum G. "Do two-phase biogas plants separate anaerobic digestion phases? – A mathematical model for the distribution of anaerobic digestion phases among reactor stages." *Bioresour. Technol.* 132, 2013: 414–418.
- Nagy, E., I. Hegedüs, D. Rehman, Q.J. Wei, Y.D. Ahdab, and J.H. Lienhard. "The need for accurate osmotic pressure and mass transfer resistances in modeling osmotically driven membrane processes. ." *Membranes* , 2021: 11, 128, doi:10.3390/membranes11020128.
- Netsch A., Horn H., Wagner M. "On-line monitoring of biofilm accumulation on graphite-polypropylene electrode material using a heat transfer sensor." *Biosensors* 12 (18), 2022: <https://doi.org/10.3390/bios12010018>.
- Neu T.R., Lawrence J.R. "Investigation of Microbial Biofilm Structure by Laser Scanning Microscopy." *Productive Biofilms 1 – 51. Part of the Advances in Biochemical Engineering/Biotechnology book series (ABE, volume 146)*, 2014.
- Niesner J., Jecha D., Stehlík P. "Biogas upgrading technologies: state of art review in European region." *Chem. Eng. Trans.* 35, 2013: 517–522.
- Pavanello G., Faimali M., Pittore M., Mollica A., Mollica A., Mollica A. "Exploiting a new electrochemical sensor for biofilm monitoring and water treatment optimization." *Water Research* 45, 2011: 1651-1658. doi:10.1016/j.watres.2010.12.003.
- Pfaff N.M., Mieke Kleijn J., van Loosdrecht M.C.M., Kemperman A.J.B. "Formation and ripening of alginate-like exopolymer gel layers during and after membrane filtration." *Water Research* 195, 2021: 116959. <https://doi.org/10.1016/j.watres.2021.11>.
-

- Picioreanu C., Vrouwenvelder J.S., van Loosdrecht M.C.M. "Three-dimensional modeling of biofouling and fluid dynamics in feed spacer channels of membrane devices." *Journal of Membrane Science* 345, 2009: 340-354. <https://doi.org/10.1016/j.memsci.2009.09.024>.
- Pratofiorito G., Hackbarth M., Mandel C., Madlanga S., West S., Horn H., Hille-Reichel A. "A membrane biofilm reactor for hydrogenotrophic methanation." *Bioresource Technology* 321, 2020: 124444 <https://doi.org/10.1016/j.biortech.2020.124444>.
- Pratofiorito G., Horn H., Saravia F. "Impact of the recovery on concentrating acetic acid with low-pressure reverse-osmosis membranes." *Membranes* 11(10), 2021: 742. <https://doi.org/10.3390/membranes11100742>.
- . "Differentiating fouling on the membrane and on the spacer in low-pressure reverse-osmosis under high organic load using optical coherence tomography." *Separation and Purification Technology* 291, 2022: 120885.
- Radu A.I., Vrouwenvelder J.S., van Loosdrecht M.C.M., Picioreanu C. "Effect of flow velocity, substrate concentration and hydraulic cleaning on biofouling of reverse osmosis feed channels." *Chemical Engineering Journal* 188, 2012: 30-39. <https://doi.org/10.1016/j.desal.2018.07.011>.
- Ravi P.P., Merkle W., Tuczinski M., Saravia F., Horn H., Lemmer A. "Integration of membrane filtration in two-stage anaerobic digestion system: Specific methane yield potentials of hydrolysate and permeate." *Bioresource Technology* 275, 2018: 138-144.
- Reyes-Romero D.F., Behrmann O., Dame G., Urban G.A. "Dynamic thermal sensor for biofilm monitoring." *Sensors and Actuators A: Physical* 213, 2014: 43-51. <http://dx.doi.org/10.1016/j.sna.2014.03.032>.
- Saha N.K., Balakrishn M.an. "Short chemical cleaning of polymeric ultrafiltration membranes fouled by sugarcane juice polysaccharides." *Desalination and Water Treatment* 2, 2009: 266–277 <http://dx.doi.org/10.5004/dwt.2009.292>.
- Salcedo-Díaz, R., P. García-Algado, M. García-Rodríguez, J. Fernández-Sempere, and F. Ruiz-Beviá. "Visualization and modeling of the polarization layer in crossflow reverse osmosis in a slit-type channel." *J. Membr. Sci.*, 2014: 456, 21–30, doi:10.1016/j.memsc.
- Schuhmann S., Simkins J.W., Schork N., Codd S.L., Seymour J.D., Heijnen M., Saravia F., Horn H., Nirschl H., Guthausen G. "Characterization and quantification of structure and flow in multichannel polymer membranes by MRI." *Journal of Membrane Science*, 2019: (570-571) 472-480.
- Siddiqui A., Pinel I., Prest E.I., Bucs S., van Loosdrecht M.C.M., Kruithof J.C., Vrouwenvelder J.S. "Application of DBNPA dosage for biofouling control in spiral wound membrane systems,." *Desalination and Water Treatment*, 2017: 68 <http://dx.doi.org/10.50>.
- Suwarno S.R., Chen X., Chong T.H., McDougald D., Cohen Y., Rice S.A., Fane A.G. "Biofouling in reverse osmosis processes: The roles of flux, crossflow velocity and concentration polarization in biofilm development." *Journal of Membrane Science* 467, 2014: 116-125.
- Tariq Khana M., Busch M., Garcia Molina V., Emwas A.H., Aubry C., Croue J.P. "How different is the composition of the fouling layer of wastewater reuse and seawater desalination RO

- membranes?" *Water Research* 59, 2014: 271–282.
<https://doi.org/10.1016/j.wat.res.2014.04.020>.
- Ucisk A.S., Henze M. "Biological hydrolysis and acidification of sludge under anaerobic conditions: the effect of sludge type and origin on the production and composition of volatile fatty acids." *Water Res.* 42, 2008: 3729–3738.
- Umpuch, C., S. Galier, S. Kanchanatawee, and H. Roux-de Balman. "Nanofiltration as a purification step in production process of organic acids: Selectivity improvement by addition of an inorganic salt.. 2010, ." *Process. Biochem*, 2010: 45, 1763–1768, doi:10.1016/j.pro.
- United Nations Educational, Scientific and Cultural Organization (UNESCO). "The United Nations World Water Development Report 2021: Valuing Water.
<https://unesdoc.unesco.org/ark:/48223/pf0000375724>." 2021.
- Valentino, F., G. Moretto, M. Gottardo, P. Pavan, D. Bolzonella, and M. Majone. "Novel routes for urban bio-waste management: A combined acidic fermentation and anaerobic digestion process for platform chemicals and biogas production." *Journal of clean production*, 2019.
- Valladares Linares R., Fortunato L., Farhat L.M., Bucs S., Staal M., Fridjonsson E.O., Johns M.L., Vrouwenvelder J.S., Leiknes T. "Mini-review: novel non-destructive in situ biofilm characterization techniques in membrane systems." *Desalination and Water Treatment*, 2016.
- Verliefde A.R.D., Cornelissen E.R., Heijman S.G.J., Verberka J.Q.J.C., Amy G.L., Van der Bruggend B., van Dijka J.C. "The role of electrostatic interactions on the rejection of organic solutes in aqueous solutions with nanofiltration." *Journal of membrane science*, 2010: 1763-1768.
- Wagner M., Horn H. "Final report (BioSclrr): On-line Erfassung, Behandlung und Reduktion der Biofilm-Bildung sowie anorganischer Ablagerungen in mit biologisch gereinigtem Abwasser betriebenen Bewässerungssystemen. BMBF-Project, Timespan: 2013-2016." 2017.
- Wagner M., Taherzadeh D., Haisch C., Horn H. "Investigation of the mesoscale structure and volumetric features of biofilms using optical coherence tomography." *Biotechnology and Bioengineering* 107, 2010: 844–853. <https://doi.org/10.1002/bit.22864>.
- Wanga Y., Fortunato L., Jeong S., Leiknes T. "Gravity-driven membrane system for secondary wastewater effluent treatment: Filtration performance and fouling characterization." *Separation and Purification Technology* 184, 2017: 26–33.
<http://dx.doi.org/10.1016/j.seppur.2017.04.027>.
- West S., Wagner M., Engelke C., Horn H. "Optical coherence tomography for the in situ three-dimensional visualization and quantification of feed spacer channel fouling in reverse osmosis membrane modules." *Journal of Membrane Science* 498, 2016: 345–352
<https://doi.org/10.1016/j.memsci.2015.09.047>.
- Wijmans J.G., Baker R.W. "The solution-diffusion model: a review." *Journal of Membrane Science*, 1995: 107 1-21 [https://doi.org/10.1016/0376-7388\(95\)00102-l](https://doi.org/10.1016/0376-7388(95)00102-l).
- Wu L., Wei W., Xu J., Chen X., Liu Y., Peng L., Wang D, Ni B. J. "Denitrifying biofilm processes for wastewater treatment: developments and perspectives." *Environmental Science: Water Research & Technology*, 2021: 7, 40-67 <https://doi.org/10.1039/D0EW00576B>.

- Wu X., Han H., Qiao J. "Data-driven intelligent warning method for membrane fouling." *IEEE Transactions on Neural Networks and Learning Systems* 32 (8), 2021: 3318-3329. <https://doi.org/10.1109/TNNLS.2020.3041293>.
- Yen J.C., Chang F.J., Chang S. "A new criterion for automatic multilevel thresholding." *IEEE Transactions on Image Processing* 4, 1995: 370-378. <https://doi.org/10.1109/83.366472>.
- Yiantsios S.G., Sioutopoulos D., Karabelas A.J. "Colloidal fouling of RO membranes: an overview of key issues and efforts to develop improved prediction techniques." *Desalination*, 2015: 183 257–272 doi:10.1016/j.desal.2005.02.052.
- Ying W., Gitis V., Lee J., Herzberg M. "Effects of shear rate on biofouling of reverse osmosis membrane during tertiary wastewater desalination." *Journal of Membrane Science* 427, 2013: 390-398. <http://dx.doi.org/10.1016/j.memsci.2012.09.054>.
- Zacharof, M.P., S.J. Mandale, P.M. Williams, and R.W. Lovitt. "Nanofiltration of treated digested agricultural wastewater for recovery of carboxylic acids." *J. Clean. Prod.* , 2015: 112, 4749–4761, doi:10.1016/j.jclepro.2015.07.004.
- Zhang P., Chen Y., Zhou Q. "Waste activated sludge hydrolysis and short-chain fatty acids accumulation under mesophilic and thermophilic conditions: Effect of pH." *Water Res.* 43, 2009: 3735–3742.
- Zhao D., Yu S. "A review of recent advance in fouling mitigation of NF/RO membranes in water treatment: pretreatment, membrane modification, and chemical cleaning." *Desalination and Water Treatment* 55, 2015: 870-891. <http://dx.doi.org/10.1080/19443994.2014.928804>.
- Zhao J., Wang D., Liu Y., Ngo H.H., Guo W., Yang Q., Li X. "Novel stepwise pH control strategy to improve short chain fatty acid production from sludge anaerobic fermentation." *Bioresour. Technol.* 249, 2018: 431–438.
- Zhou, F., C. Wang, and J. Wei. " Simultaneous acetic acid separation and monosaccharide concentration by reverse osmosis. *Bioresour. Technol.*" 2013: 131, 349–356, .
- Zhu X., Leininger A., Jassby D., Tsesmetzis N., Ren Z.J. "Will membranes break barriers on volatile fatty acid recovery from anaerobic digestion? *ACS EST Eng.*" 2020: 1, 141–153, doi:10.1021/acsestengg.0c00081.
- Zhu Y., Galier S., Roux-de Balman H. "Nanofiltration of solutions containing organic and inorganic salts: Relationship between feed and permeate proportions. 2020,," *J. Membr. Sci.*, 2020: 613, 118380, doi:10.1016/j.memsci.2020.118380.